AD-E800273

LEVEL III (12)

AD A099590

Supplement to
NASA Conference Publication 2128
FAA-RD-80-30

Lightning Technology

Proceedings of a technical symposium
held at NASA Langley Research Center,
Hampton, Virginia, April 22-24, 1980

DTIC
ELECTE
JUN 1 1981
S D
A

This document has been approved for public release and sale; its distribution is unlimited.

DTIC FILE COPY

387543

81 5 28 022

Supplement to

NASA Conference Publication 2128

FAA-RD-80-30

Lightning Technology

Proceedings of a technical symposium sponsored by the National Aeronautics and Space Administration, the Florida Institute of Technology, and the Department of Transportation and held at NASA Langley Research Center, Hampton, Virginia, April 22-24, 1980

NASA

National Aeronautics
and Space Administration

**Scientific and Technical
Information Branch**

1981

PREFACE

The proceedings of the 1980 Symposium on Lightning Technology held at Langley Research Center April 22-24, 1980, are reported in NASA CP-2128. The Symposium was sponsored by the National Aeronautics and Space Administration, the Florida Institute of Technology, and the Department of Transportation.

This supplement contains papers that were presented at the Symposium, but were unavailable for printing at the time of publication of NASA CP-2128.

This publication was prepared from camera-ready copies of the conference presentations supplied by the authors. The material presented in this report was taken from a variety of sources; therefore, various units of measure are used. Use of trade names or names of manufacturers in this report does not constitute an official endorsement of such products or manufacturers, either expressed or implied, by NASA.

Felix L. Pitts

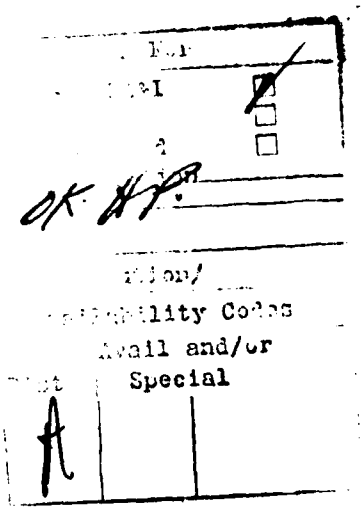

CONTENTS

AIRBORNE LIGHTNING CHARACTERIZATION*

Capt. Robert K. Baum

Air Force Wright Aeronautical Laboratories

SUMMARY

A WC-130 aircraft was instrumented with wideband electromagnetic field sensors and flown near active thunderstorms to obtain data on the characteristics of nearby and direct strike lightning. An electric field ground station and time-of-arrival network provided time correlated data to identify the three dimensional locations of the discharge and the different events in the lightning flash. A description of the sensors, calibration procedures, and recording equipment is presented. Data are presented on return stroke characteristics in the 5 to 50 km range. At the time of this writing, data on the three dimensional source locations are not available for publication.

INTRODUCTION

The present interest in high frequency lightning characterization stems in part from a concern over an increasing susceptibility of modern aircraft to the electromagnetically coupled effects produced by lightning. Aircraft susceptibility is expected to increase with the use of composite materials and more susceptible microelectronics. To compound the susceptibility problem, the high frequency nature of the lightning event is not as yet well defined. For example, transients arising from the pre-attachment stepped leader process or nearby interstroke and intracloud processes may well be as important from a coupling standpoint as the return stroke phase itself. It is of increasing importance, therefore, to obtain a more refined empirical model of the overall lightning event taken from an appropriate base of wideband measurements.

In 1979, the Air Force Wright Aeronautical Laboratories began a joint flight research program with the National Oceanic and Atmospheric Administration to obtain data on the high frequency characteristics of lightning. Objectives of the 1979 phase of the program were: 1) develop a sensor/instrumentation package with linear response and recording capabilities in the 0.1-20 MHz range, 2) develop a ground station recording system capable of providing three dimensional locations of very high frequency (VHF) lightning activity with an accuracy of ± 250 m on a 20 km radius, 3) obtain wideband airborne data on electric and magnetic field characteristics associated with lightning within a 20 km range, 4) obtain and compare corresponding wideband aircraft skin current transients, and 5) correlate ground measurements (VHF source location and electric field) with the airborne data to permit field scaling, channel reconstruction, and isolation of important coupling events.

At this writing, the source location data were being analyzed and correlated with the airborne data. A short description of the ground station apparatus and the approach to be used to analyze the data is presented.

---

*Revision of paper 8 in NASA CP-2128.

Construction and calibration of the airborne sensors is described since they have not been used in any previous program of this type.

GROUND STATION DESCRIPTION

The ground station was situated at Devil's Garden, Florida. It consisted of two separate systems, one to identify the discharge phase, the other to determine the three dimensional VHF lightning source locations.

Phase Identification

The discharge phase was identified using a low frequency electric field measuring system similar to that described by Fisher and Uman (ref. 1). Two plate antennas and three separate recording channels were used to allow linear sensing over the 80 db dynamic range in electric field levels expected within a 20 km radius of the site.

VHF Source Location

The VHF source location system was similar in concept to the Lightning Detection and Ranging (LDAR) system (ref. 2) with modifications as described by Rustan(ref. 3). The system used provides continuous source location data based on differences in times of arrival (DTOA) of the lightning pulses at widely separated stations. The system consisted of three recording stations and a central site positioned in a Y configuration on a 20 km radius. Two backup recording stations were placed on the same radius to provide redundant data. Antennas at each site consisted of four folded dipoles oriented to provide circularly polarized omnidirectional response. The antenna outputs were passed through a 6 MHz bandpass filter centered at 63 MHz. An envelope detector and a logarithmic amplifier were used to effectively compress frequency and dynamic range of the signal to within limits of the recorder. A complete description of the time domain relationship between the antenna output and the recorded signal has been published by Rustan (ref. 3).

The processed VHF signals received at each site were recorded on separate modified video recorders (in contrast to the LDAR system which re-transmits the signals to a central site). The recorders were tuned to a commercial broadcast station (Channel 11) and a normal video recording was made except that the luminance portion of the composite video signal was replaced with the VHF signal and the audio portion of the signal was replaced with a demodulated IRIG B time code transmitted from the test aircraft (see fig. 1). The recording system was designed to operate automatically when the transmitted IRIG B carrier was detected for a period of 10 seconds.

The Timing System

To provide the required source location accuracy of ± 250 m, the data from each video recorder must be time correlated with a relative error no greater than ± 0.1 μs. This was achieved using the transmitted IRIG B as a coarse absolute time reference (common to all airborne and ground-based data) in com-

bination with the vertical and horizontal sync pulses detected and recorded from the composite video signal. The vertical sync pulse (VSP) occurs every 16.66 ms and was used to identify the beginning of one 'frame' of data from one of the two rotating video record heads. The fine time resolution within a given frame was derived from the chroma reference signal (CRS). The CRS is a 3.58 MHz signal recorded from the composite video signal by separating and heterodyning to 629 kHz. The phase of the CRS is advanced 90 degrees by the occurrence of the broadcast horizontal sync pulse every 65.1 μs. By passing the CRS through a band-reject filter centered at 629 kHz, the periodic phase shift is seen on playback as a sharp spike occurring nominally every 65.1 μs. This signal was also used to correct the VHF signal for minor fluctuations in headwheel and capstan speed inherent in the recorders. Figure 2 illustrates the various timing pulses reproduced or derived from the data. Data from the VHF stations were digitized and time correlated using the signals described. VHF source locations were then calculated for selected short intervals corresponding to the airborne recordings using the waveform correlation techniques developed by Rustan (ref. 3).

AIRCRAFT DESCRIPTION

Sensors

The test aircraft was fitted with two single axis sensors to detect free field radiation and a sensor on each wing to detect induced skin currents. The sensors were placed as shown in figure 3. The free field sensors were placed on the symmetry axis of the aircraft (forward upper fuselage) to reduce coupling from symmetric resonances on the aircraft skin. All sensors were designed to have a usable bandwidth of at least 20 MHz.

The vertical component of the incident electric field E(t) was sensed by a parallel plate dipole (PPD) patterned after a design by C. Baum (ref. 4). The sensor consisted of a pair of 0.2 m diameter concentric plates mounted on opposite sides of a common ground plane. Each plate was loaded with an 80 ohm resistive rod in series with a 50 ohm cable matching resistance which served as the signal pickoff point. This configuration resulted in a balanced 100 ohm differential output. The sensor assembly was elevated 0.25 m from the fuselage surface and enclosed in a protective fiberglass fairing. Equivalent height of the sensor (h_{eq}) was calculated to be 0.101 m. Sensor capacitance (C) as derived from reference 4 was 7.1 pF. The equivalent circuit of the sensor is shown in figure 4.

The C_s parameter in figure 4 represents the total stray and distributed capacitance which was found from measurement to be $\simeq$ 1.5 pF. From figure 4, the output voltage of the sensor can be written as:

$$v_o(s) = -R_L C h_{eq} s E(s) \qquad (1)$$

where s is the Laplace transform variable, R_L is the load resistance, C is the sensor capacitance, and h_{eq} is the equivalent height of the sensor. Equation

1 is valid provided that:

$$R \ll \frac{1}{2\pi C_s f_{max}} \qquad \text{and} \qquad f_{max} < \frac{1}{2\pi C(R+R_L)} \tag{2}$$

where f_{max} is the upper frequency of interest. With the values given, these conditions are satisfied for $f \leq 20$ MHz. Within this frequency range, the sensor responds to the time rate of change of the electric field with a sensitivity constant K_E given by:

$$K_E = RCh_{eq} \simeq 7.17 \times 10^{-11} \ \frac{v\text{-}s\text{-}m}{v} \tag{3}$$

Since the effects of the sensor mounts and enclosure were not easily calculated, the entire apparatus was tested in a 50 ohm parallel plate transmission line to derive K_E. A continuous wave (CW) test was performed using a sinusoidal signal ranging in frequency from 0.1 to 15 MHz as input to the transmission line. K_E was then calculated from the following time domain equivalent of equation 1:

$$v_o(t) = -R_L Ch_{eq} \frac{dE}{dt} = -K_E \frac{dE}{dt} \tag{4}$$

For sinusoidal excitation in the derivative band of the sensor, equation 4 can be written as:

$$v_o(t) = -K_E \omega A \sin(\omega t) \tag{5}$$

where A is the peak amplitude of the input sinusoid and ω is the radian frequency. When peak readings are taken, equation 5 can be rewritten as:

$$|K_E| = \frac{v_o(t)}{\omega A} \tag{6}$$

K_E was found to be 4.32×10^{-11} V-s-m/V from the CW test, and this was the value used in the data analysis.

The incident magnetic field sensor consisted of a one conductor multi-turn loop patterned after a design by C. Baum (ref. 5). The sensor was a split copper cylinder, 0.635 m in diameter, wrapped with triaxial cable to yield an effective 4 turn loop with an equivalent area A_{eq} of 0.051 m^2. Sensor inductance of 0.71 μH was found from tables developed by C. Baum (ref. 5). From the equivalent circuit shown in figure 5, the sensor output voltage in the complex frequency domain is given by:

$$V_o(s) = A_{eq} \ s \ B(s) \tag{7}$$

provided that:

$$R_L >> R_s \qquad \text{and} \qquad f_{max} < \frac{R_L}{2\pi L} \tag{8}$$

For the values given, the self-integrating frequency of the sensor ($R_L/2\pi L$) is marginally greater than the 20 MHz limit of interest. The sensitivity constant for the sensor is simply:

$$K_B = A_{eq} \simeq 0.051 \text{ V-s/T} \tag{9}$$

This constant was verified to within ± 5% in the parallel plate transmission line, using the CW test technique described earlier.

The two skin current sensors each consisted of a shielded, two turn rectangular half loop (0.027 m high, 0.305 m long) mounted directly on a removable aircraft skin panel. Sensor output was taken from the underside of the panel into a short 100 ohm twinaxial cable. From the loop dimensions, the sensor's equivalent area was calculated to be 0.0165 m^2. The approxiamte loop inductance was calculated to be 2.7 μH from (ref. 7):

$$L = n^2 \mu_o (b+d) \left[\log_e \left[\frac{bd}{a(b+d)} \right] + 0.25 \right] \tag{10}$$

where n is the number of loop turns, b and d are the rectangle dimensions, a is the shield radius and μ_o is the free space permeability.

From Ampere's law and Faraday's law of induction, the induced loop voltage at the sensor output $v_i(t)$ is related to the time derivative of the surface current density $\dot{J}_s$ on the panel by:

$$v_i(t) = -\mu_o A_{eq} \dot{J}_s \tag{11}$$

where the assumption is made that negligible flux penetrates the underside of the panel.

The sensor equivalent circuit is identical to the magnetic field circuit in figure 5 with the voltage $v_i(t)$ given by equation 11. The Laplace transfer function for the sensor (assuming $r_s << R_L$) is given by:

$$v_o(s) = -K_J J(s) \left[\frac{s}{s + R/L} \right] \tag{12}$$

where:

$$K_J = \mu_o A_{eq} \frac{R_L}{L} \approx 0.723 \text{ A/m-V} \tag{13}$$

The condition ($f_{max} << R_L/2\pi L$) from equation 8 is not met as was the case with the magnetic field sensor, hence the 's + R_L/L' term must be retained in equation 12. The resulting time domain relation between the sensor output and the surface current density is therefore:

$$J_s = -\frac{1}{K_J}\left[v_o(t) + \frac{R_L}{L} \int_o^t v_o(t)dt \right] \tag{14}$$

Using this relation, the K_J parameter was verified within ± 5% from a CW test similar to the one already described for the electric field sensor.

The transient response characteristics of the sensors were verified in the 50 ohm parallel plate transmission line using a 13.5 V, 12 ns rise step as the input. Figure 6 shows the step input and the corresponding response of each of the sensors. The frequency response plots shown in figure 6 were derived by computing the log magnitude of the Fourier transform of the derivative of each sensor output (a valid technique as long as the excitation function is a good step approximation; i.e. $t_r \leq 15$ ns for 20 MHz).

Recording Equipment

Each sensor output was routed via a short twinaxial cable to a shielded, battery-operated fiber optic link which in turn was connected to parallel digital and analog recording systems. The digital recording system consisted of four Biomation 8100 digital transient recorders which provided threshold triggered records (2048 samples, 10 ns sample interval) of each sensor output. The digital records, together with the acquisition time and aircraft position, were stored on flexible disk. The analog recording system was a multi-channel analog recorder with a bandwidth of 400 Hz to 150 kHz. The continuous analog record was required to identify the particular event in the discharge process which triggered the digital system.

The instrumentation was protected from internal transients and power supply surges through the use of metal enclosures, solid-state transient suppressors and power supply isolation filters. A block diagram of the instrumentation is shown in figure 7.

Timing

The time reference for the entire recording system was taken from the IRIG B time code generated on-board the aircraft. The time code was also transmitted to the various ground sites to permit time correlation between the air and ground data. Resolution of the IRIG B time code, typically limited to ± 0.5 ms

will be improved to ± 10 μs using correlation techniques on the code waveform after correction for propagation delays.

PROCEDURE

Prior to each flight, functional tests were performed with small loop and dipole antennas driven by a signal generator to insure integrity of the sensor, optic system, and recorders. Sensor outputs were stored and compared daily for any significant variation in signal amplitude or response characteristics. Every two weeks, sensor cabling was disconnected and a signal injected directly into the fiber optic transmitter to insure that the cable insertion losses remained approximately constant. Analog tapes were stripped and degaussed before each flight.

Flights were typically two hours in duration and were taken in the early afternoon when storm activity was verified over the ground site. The aircraft was flown in a 40 km clockwise rectangular pattern around the central site at a nominal altitude of 4 km. The aircraft was restricted from penetrations into developed storm cells although many flights were taken into heavy precipitation areas surrounding the cell area.

Data from the digital system were stored only when a return stroke was visually verified by one of the aircraft observers or when a direct strike appeared to have occurred. When a nearby strike was observed, the approximate range and azimuth were noted for later verification of position data.

RESULTS

Data were obtained from 7 flights in the immediate vicinity of the ground station during the period from 17 August to 28 September 1979. Data from 43 visually verified cloud-ground return strokes were recorded on the airborne analog/digital system and on the VHF source location system. Data from the low frequency electric field antenna site were not usable this year due to operation difficulties. It is anticipated that phase identification can still be accomplished from the low frequency airborne data. Data were also recorded on two separate events believed to have occurred immediately prior to direct aircraft strikes. The direct strike assumption was verified by pilot report and attachment evidence on the aircraft radome. At this time however, the actual phase of the discharge which was recorded is not known. To date, the only data analyzed in detail are the high frequency airborne recordings. The following results are therefore presented without benefit of phase identification or accurate source location.

The high frequency recordings were grouped into three general categories: first return stroke, subsequent return strokes, and unidentified. The last category arises from the substantial number of waveform which were of the same approximate peak amplitude as the return stroke data but were isolated and impulse-like with total duration times on the order of 100-200 ns and were devoid of any of the classic return stroke waveshape characteristics.

First And Subsequent Stroke Characteristics

The return stroke waveforms were classified as first or subsequent based on the characteristics discussed by Weidman and Krider (ref. 8). Figure 8 shows typical first and subsequent return stroke electric field waveforms taken from the data. The first stroke is characterized by a slowly rising (1 to 3 μs) concave front (F in fig. 8a) sometimes followed by an abrupt fast transition to peak portion (R in fig. 8a) lasting on the order of 100-700 ns. Subsequent strokes are further characterized by the absence of a slow front portion and the relatively smooth and structureless subsidiary peaks (a,b,c in fig. 8b) compared to those of the first strokes.

Front And Fast Transition Times

The 10-90% rise time was calculated for the fast transition portion (R) of the first stroke waveforms. Average R for 22 waveforms was 390 ns. For comparison, the average front plus fast transition time (F+R) was found to be 2.2 μs. Relative distributions of the two rise times are shown in figure 9. Based on the criteria described earlier, four electric field waveforms were classified as subsequent strokes. Average 10-90% fast transition time for these strokes was 550 ns. The peak electric and magnetic field levels recorded ranged from 13 to 146 V/m and 0.017 to 0.145 A/m respectively, indicating an approximate distance from the aircraft of 5 to 50 km (ref 9).

The average fast transition time quoted for both first and subsequent return strokes are approximately two times slower than those reported by Weidman and Krider (ref. 8). The discrepancy is probably due to several factors. First, the 50 ns resolution claimed for direct interpretation of oscilloscope photographs may be in error since this translates to a horizontal axis distance of only 0.25 mm assuming a 10 cm scope face and 20 μs sweep. The rise times in this report were computer calculated from the digitized record and have a maximum resolution of two times the sample interval, or approximately 20 ns on a 20 μs record. Second, the rise times in this report were not corrected for the HF propagation losses over land which was not a factor in Weidman and Krider's data since the propagation was over salt water. Third, and probably most importantly, no standard method exists for defining the beginning of the F and R waveform transition points.

Rise Time Calculation Procedure

In this paper, a consistent method was adopted in which the F and R points were defined by the intersection point of two straight lines whose slopes were given by the best fit straight line through two waveform segments chosen well away from the waveform transition areas. Figure 10 illustrates the method using a first stroke waveform where the F and R points are marked by triangles and the corresponding best fit lines are shown dashed. In the data presented, the best fit lines were computer calculated using the method of least squares but a graphic approximation would be adequate in most cases.

Rise Times and Aperture Coupling

From a standpoint of developing a good model of the aircraft/lightning interaction, at least during the direct attachment return stroke phase, the importance of accurate radiation field rise times cannot be overemphasized. As evidence of this, consider the above ground field equations developed by Uman et al. (ref 10), which describes the time derivative of the magnetic field dB(t)/dt at an altitude z, slant range R, and horizontal range r from the idealized return stroke:

$$\frac{dB(t)}{dt} = \frac{\mu_o v(t)}{4\pi R}\left[\frac{r}{R^2}\, i(Z,t-R/c) + \frac{r}{cR}\,\frac{\partial i(Z,t-R/c)}{\partial t} + \text{Image Terms}\right] \quad (15)$$

where v(t) is the vertical stroke velocity (assumed constant), c is the speed of light and Z is the dipole height above the ground plane. The image term is given by substituting the image slant range R_I and image height $-Z_I$ for R and Z respectively into the first term in equation 16. If $r \geq 3(Z_I + z)$, the image term contribution is approximately equal to the source term, and the Laplace transform of equation 15 (omitting the phase delay term due to the retarded time) is:

$$I(s) \simeq \frac{2\pi rc}{\mu_o v} B(s)\left[\frac{r}{s + c/r}\right] \quad (16)$$

From equation 16, it is apparent that the return stroke current is approximately proportional to the radiation component of the magnetic field provided:

$$R \geq 3(Z_I + z) \qquad \text{and} \qquad f_{min} >> c/2\pi r \quad (17)$$

where f_{min} is the minimum frequency of interest.

Now consider further the aircraft involved in the return stroke phase of a lightning. After entry and exit points have been established, the channel discontinuities caused by the aircraft are small and the return stroke current passes through the aircraft essentially unperterbed. The return stroke current i(t) results in an average magnetic field tangential to a small aperture and an electric field normal to the aperture given by:

$$h_T(t) = i(t)/2\pi r_{ave} \qquad \text{and} \qquad e_n(t) = \rho(t)/\varepsilon_o \quad (18)$$

where r_{ave} is the average equivalent radius of the principal conducting element (i.e. wing, fuselage), $\rho(t)$ is the time varying charge density, and ε_o is the permittivity of air. As discussed by Cabayan (ref. 11), the fields interior to the aperture are proportional to the exterior fields as follows:

$$\begin{aligned} e_N(t) &\propto \left[\frac{1}{R^3}\, e_N(t) \;,\; \frac{1}{R^2}\, \dot{e}_N(t)\right] \\ e_T(t) &\propto \left[\frac{1}{R^2}\, \dot{h}_T(t) \;;\; \frac{1}{R}\, \ddot{h}_T(t)\right] \\ h_T(t) &\propto \left[\frac{1}{R^3}\, h_T(t) \;,\; \frac{1}{R^2}\, \dot{h}_T(t) \;,\; \frac{1}{R}\, \ddot{h}_T(t)\right] \end{aligned} \quad (19)$$

where the primed quantities refer to the interior fields and R is the distance away from the aperture as shown in figure 11. Thus, the aperture coupled fields on the aircraft are dependent not only on the stroke current but also on its first and second derivatives, and the importance of accurate return stroke rise time definition becomes evident. Of course, the rise time can only be used to calculate an average derivative. To the extent that the return stroke average derivative varies from its true instantaneous derivative, the expected aperture coupled fields will be in error. Thus from a coupling standpoint, the best rise time calculation is that which provides derivatives agreeing most closely with the instantaneous derivative.

Peak and Average Derivatives

A comparison was made between the peak instantaneous derivative (D_p) taken from the unintegrated record and the average derivatives calculated from the F+R intervals (D_{F+R}) and the R interval only (D_R) taken from the integrated initial stroke record. From a 15 waveform sample, the following average results were obtained:

$$D_p = 7.9\ D_{F+R} \qquad \text{and} \qquad D_p = 2.3\ D_R \tag{20}$$

These averages agree well with the work of Weidman and Krider (ref. 8) who estimated peak derivative values 3 to 10 times faster than those inferred by straight line approximation. The distribution of D_p taken from 23 unintegrated electric field records is shown in figure 12 where the values have been normalized to 100 km. (ref. 12). Again, the average D_p of 20.3 V/m-μs at 100 km are in very close agreement with the estimates by Weidman and Krider (ref. 8). The fast transition derivative D_R is evidently a reasonable approximation to the peak derivative while the D_{F+R} derivative is definitely not suitable for accurate estimation of the peak return stroke derivative.

Peak Return Stroke Derivatives

Given the average observation distance of 20 km and the short record length of 20 μs, the conditions given in equation 17 were satisfied for the data obtained, and the D_p values were used to infer peak return stroke current derivatives from the time domain equivalent of equation 16:

$$\frac{di(t)}{dt} = \frac{2\pi rc}{vZ_o}\left[\frac{dE(t)}{dt}\right] \tag{21}$$

where Z_o is the free space impedance (377 ohms), and the quantity ($1/\mu_o$ x B(s)) has been replaced in equation 16 with the radiation field equivalent term ($1/Z_o$ x E(s)). If the return stroke velocity v(t) is assumed constant at 1×10^8 m/s (Uman, ref. 10), the peak return stroke derivative inferred from equation 21 ranged from 30 to 150 kA/μs with an average value of 100 kA/μs.

Unidentified Waveforms

As mentioned earlier, a substantial number of waveforms were recorded which could not be identified as return stroke fields. The acquisition time of these data correspond (approximately) in time to visual reports from the

aircraft observers of cloud-ground or intracloud discharges. Range estimates to the discharge, based on these reports, vary from 6 to 15 km. At these ranges, a preliminary breakdown process may have had sufficient field strength to overcome the threshold trigger level on the digital recording system. The unidentified data were pulse-like in nature with peak amplitudes in the same range as the return stroke data (10-100 V/m), with pulse rise times varying from 300 ns to 40 ns (or less). Figure 13 illustrates a time-correlated set of pulse waveforms taken form the free field and skin current sensors. A more complete analysis of the skin currents and pulse data will be made when phase and source location data are available.

CONCLUSIONS

This report presents the first results obtained from a planned three year research effort to study the high frequency characteristics of lightning. The conclusions reached thus far are summarized below.

Accurate measurement of the peak return stroke current derivatives are important in simulating aperture coupled fields on the aircraft. The peak return stroke derivatives inferred from the electric field derivative record ranged from 30 to 150 kA/μs with an average value of 100 kA/μs. The average front plus fast transition rise time (10-90%) for 22 initial strokes was 2.2 μs. The peak current derivatives inferred from this rise time were an average of approximately 8 times lower than the true instantaneous derivative. The average rise time for the fast transition portion only was 390 ns which yielded a much more reasonable estimation of peak current derivative, averaging approximately two times lower than the true instantaneous derivative. The electric field peak derivatives averaged 20.3 V/m-μs when normalized to 100 km. This value is in good agreement with the estimates of Weidman and Krider and lends further support to the calculated return stroke derivative values.

Unidentified pulses were recorded which had peak magnitudes of 10-100 V/m and rise times ranging from 300 ns to 40 ns (or less). The pulses were recorded during visually confirmed flashes. The high frequency characteristics of these data may present a significant coupling source to the aircraft and will be investigated further.

REFERENCES

1. Fisher, R.J. and M.A. Uman, Measured Electric Field Risetimes for First and Subsequent Lightning Return Strokes, J. Geophys. Res., V. 77, No. 3, Jan 1972.

2. Lennon, K., LDAR III - System Description and Performance Objectives, Federal Electric Corporation, RF Systems Branch, Kennedy Space Center, 26 April 1977 (unpublished).

3. Rustan, P.L., Properties of Lightning Derived From Time Series Analysis of VHF Radiation Data, PhD dissertation, University of Florida, 1979.

4. Baum, C.E., the Circular Parallel Plate Dipole, AFWL Electromagnetic Pulse Sensor and Simulation Notes, AFWL EMP 1-6, Note 80, July 1971.

5. Baum, C.E., A Technique for Distribution of Signal Inputs to Loops, AFWL Electromagnetic Pulse Sensor and Simulation Notes, AFWL EMP 1-1, Note 23 Dec 1966.

6. Baum, C.E., Further Considerations for Multiturn Cylindrical Loops, AFWL Electromagnetic Pulse Sensor and Simulation Notes, AFWL TR 73-168, Note 127 April 1971.

7. Grover, F.W., Inductance Calculations, Dover Publications, N.Y., N.Y., 1946.

8. Weidman, C.D. and E.P. Krider, The Fine Structure of Lightning Return Stroke Waveforms, J. Geophys. Res., V. 83, No. C12, Dec 1978.

9. Uman, M.A., R.D. Brantley, Y.T. Lin, J.A. Tiller, E.P. Krider, and D.K. McLain, Correlated Electric and Magnetic Fields From Lightning Return Strokes, J. Geophys. Res., V. 80, No. 3, Jan 1975.

10. Uman, M.A., Y.T. Lin, R.B. Standler, M.J. Master, and R.J. Fisher, Calculations of Lightning Return Stroke Electric and Magnetic Fields Above Ground, Symposium on Lightning Technology, NASA CP-2128, 1980.

11. Cabayan, H.S. and J.E. Zicker, Review of Article "A case for Submicrosecond Rise Time Lightning Current Pulses for use in Aircraft Induced Coupling Studies", by D.W. Clifford, E.P. Krider, and M.A. Uman, Lawrence Livermore Laboratory, University of California, Memorandum No. EMS 80-0016, Jan 17, 1980.

12. Krider, E.P., C.D. Weidman, and R.C. Noggle, The Electric Fields Produced by Lightning Stepped Leaders, J. Geophys. Res., V. 82, No. 6, Feb 20, 1977.

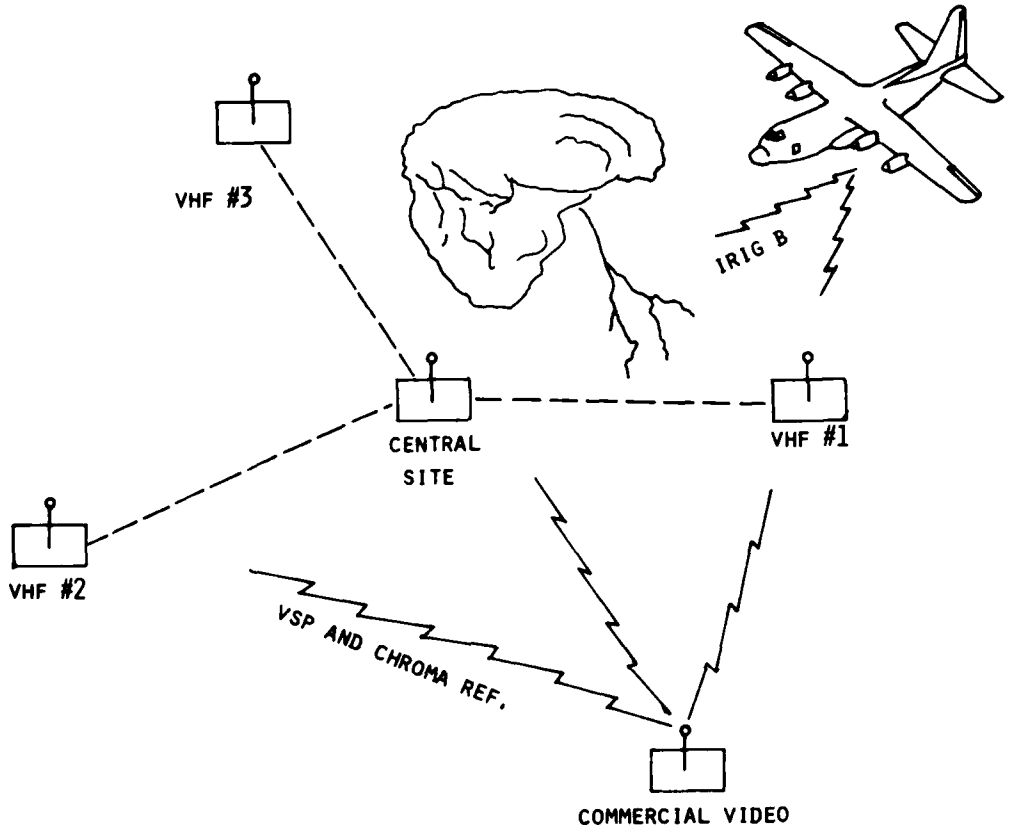

Figure 1. Orientation of Ground Sites and Test Aircraft

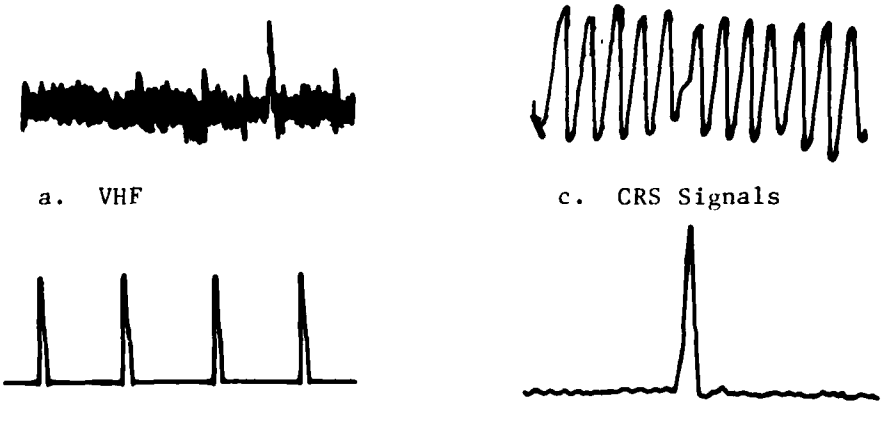

a. VHF

c. CRS Signals

b. Vertical Sync Pulse

d. Derived Pulse

Figure 2. Illustration of Typical VHF Source Pulses & Timing Signals (not to scale)

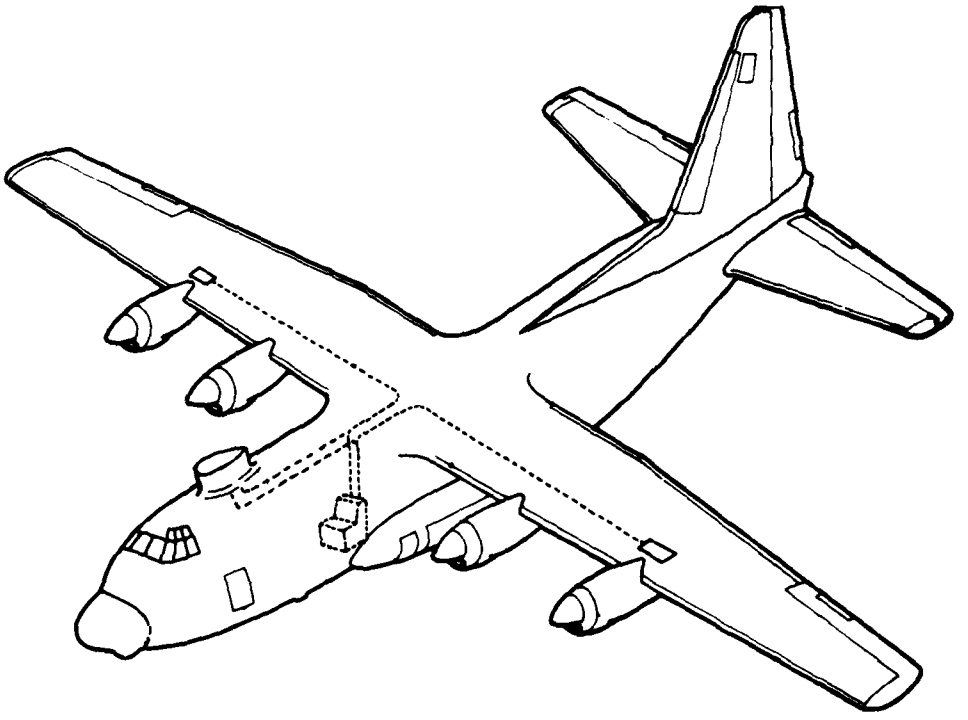

Figure 3. Aircraft Sensor Locations

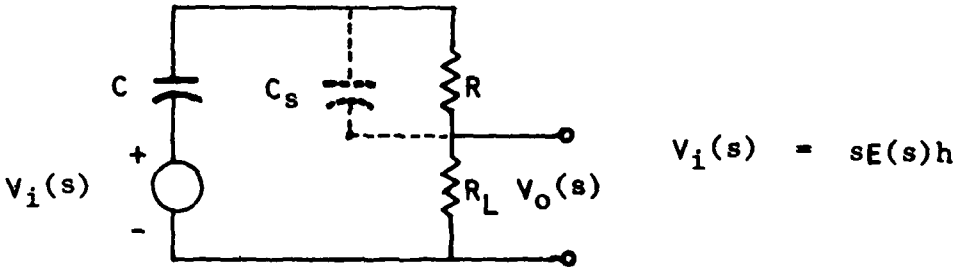

Figure 4. E Field Sensor Equivalent Circuit

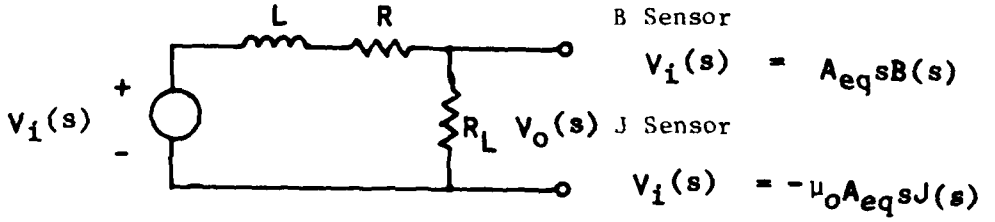

Figure 5. B and J Sensors Equivalent Circuit

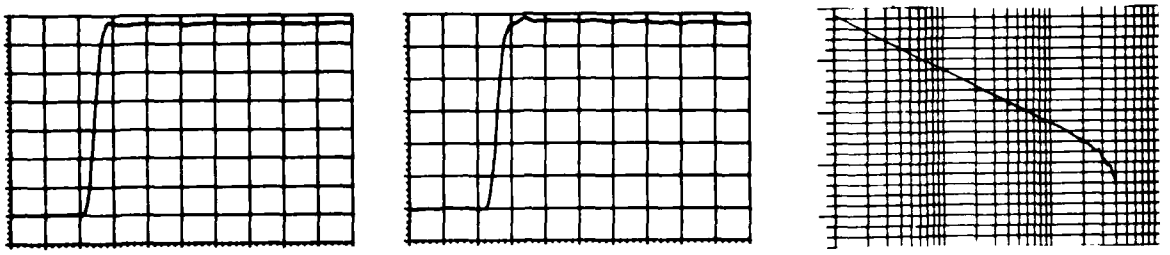

Applied Voltage | Applied Current | Applied Spectrum

a. Input Characteristics

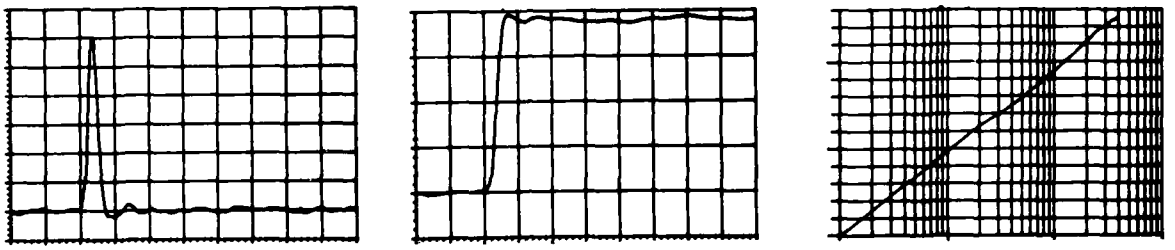

Output Voltage | Integrated Output | Frequency Response

b. Electric Field Sensor

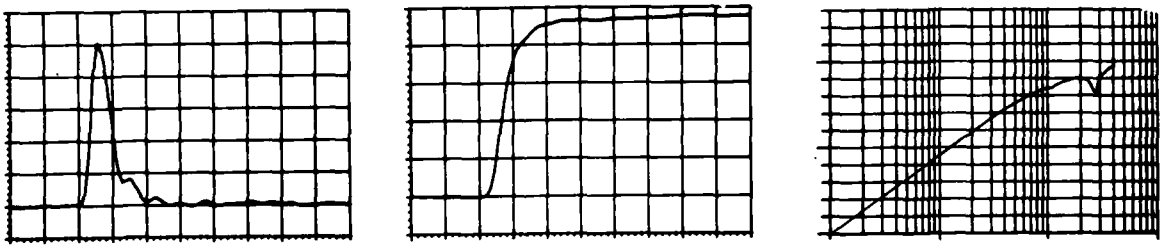

Output Voltage | Integrated Output | Frequency Response

c. Magnetic Field Sensor

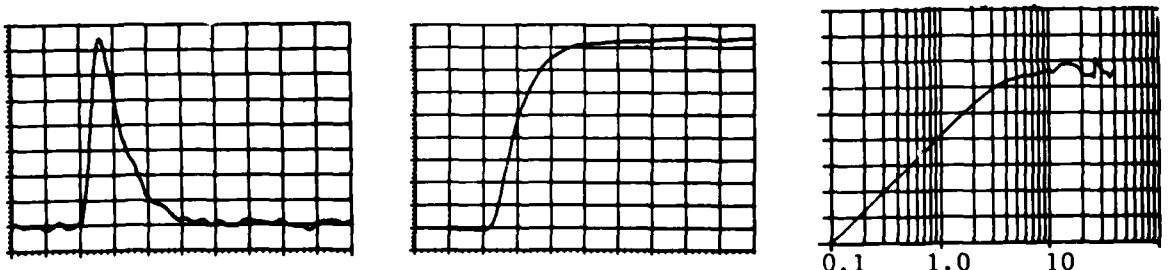

50 nanoseconds/div | 50 nanoseconds/div

Output Voltage | Integrated Output | Frequency Response

d. Surface Current Sensor

Figure 6. Sensor Response Characteristics

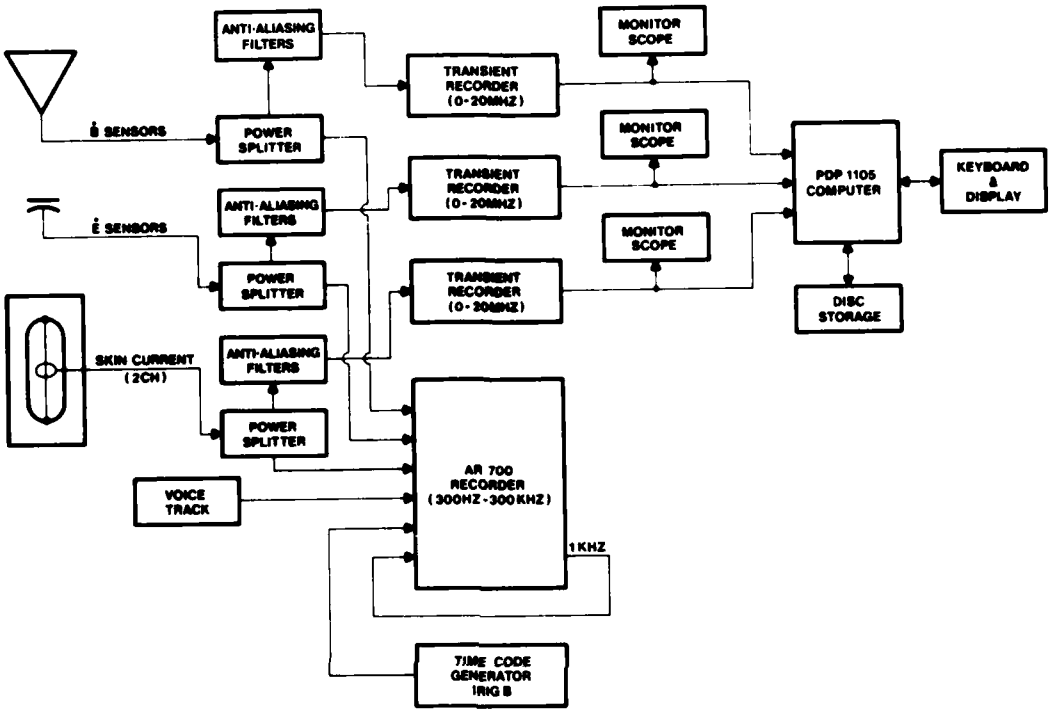

Figure 7. Airborne Instrumentation Diagram

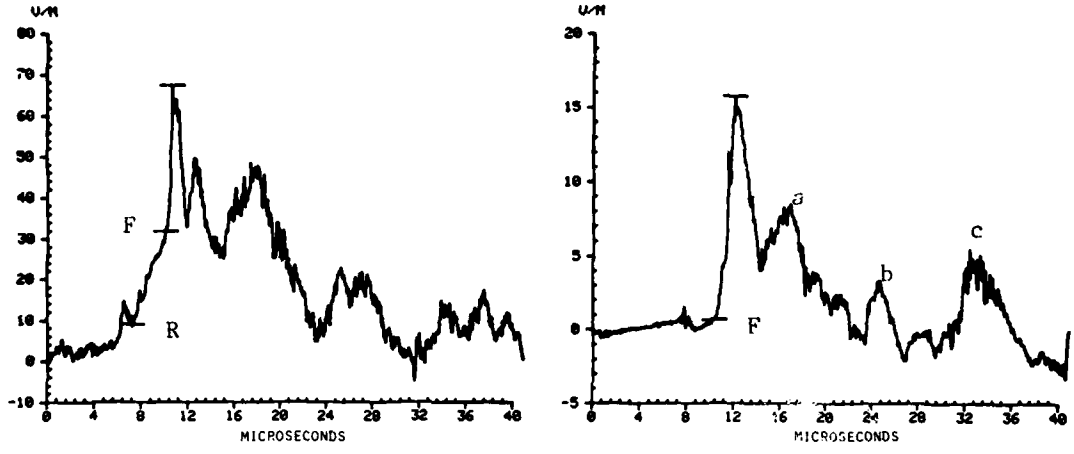

a. b.

Figure 8. Typical First (a) and Subsequent (b) Return Stroke Radiation Field Waveforms

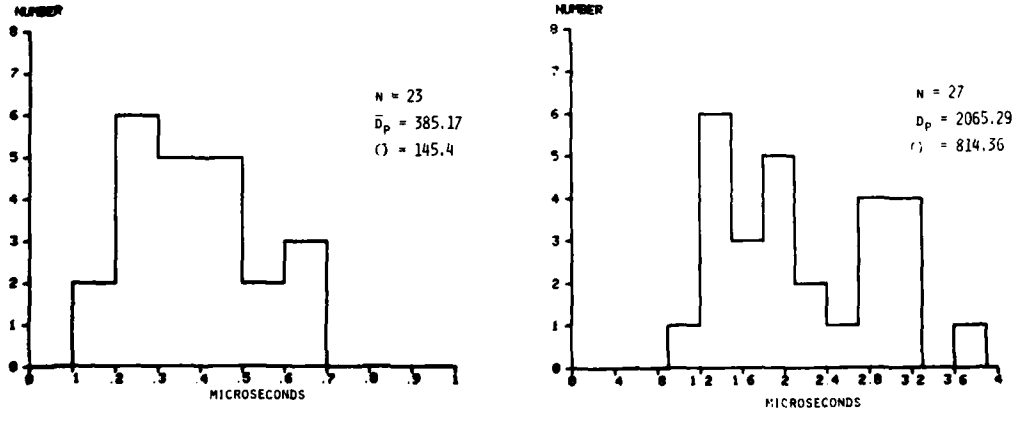

a. b.

Figure 9. Distribution of First Stroke Risetimes : (a) Fast Transition Time Only, and (b) Fast Transition Plus Slow Front.

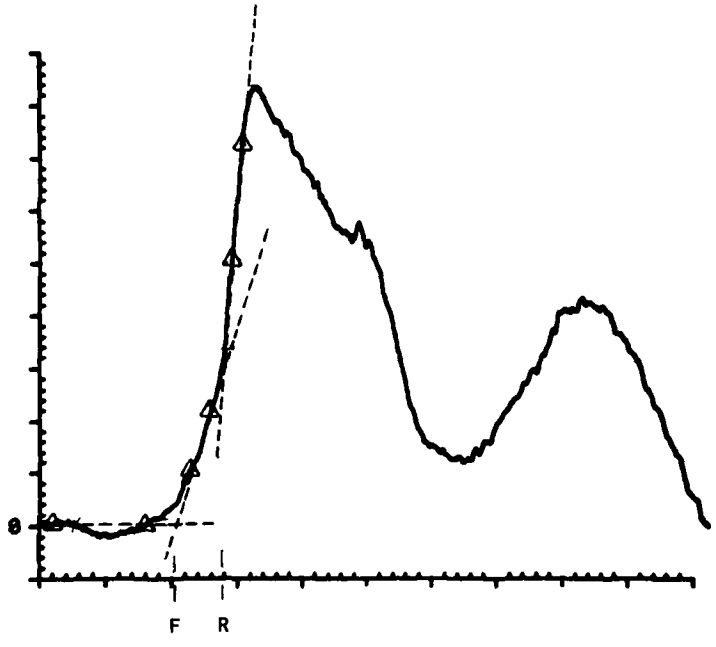

Figure 10. Rise Time Calculation from Best-Fit Segment Intersection

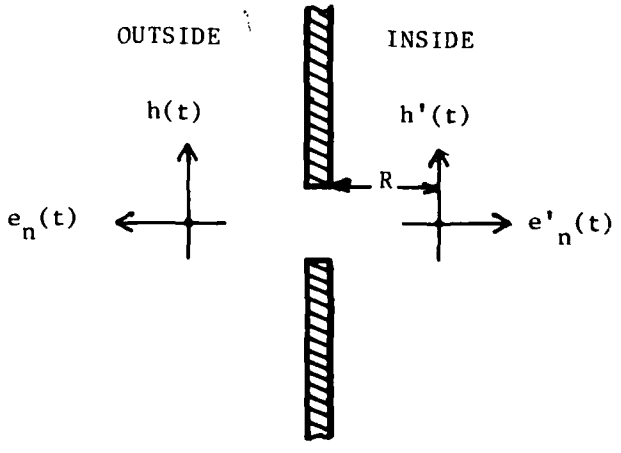

Figure 11. Aperture Geometry

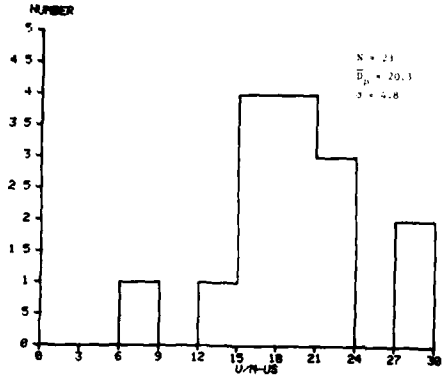

Figure 12. Distribution of Peak Electric Field Derivatives Normalized to 100 km.

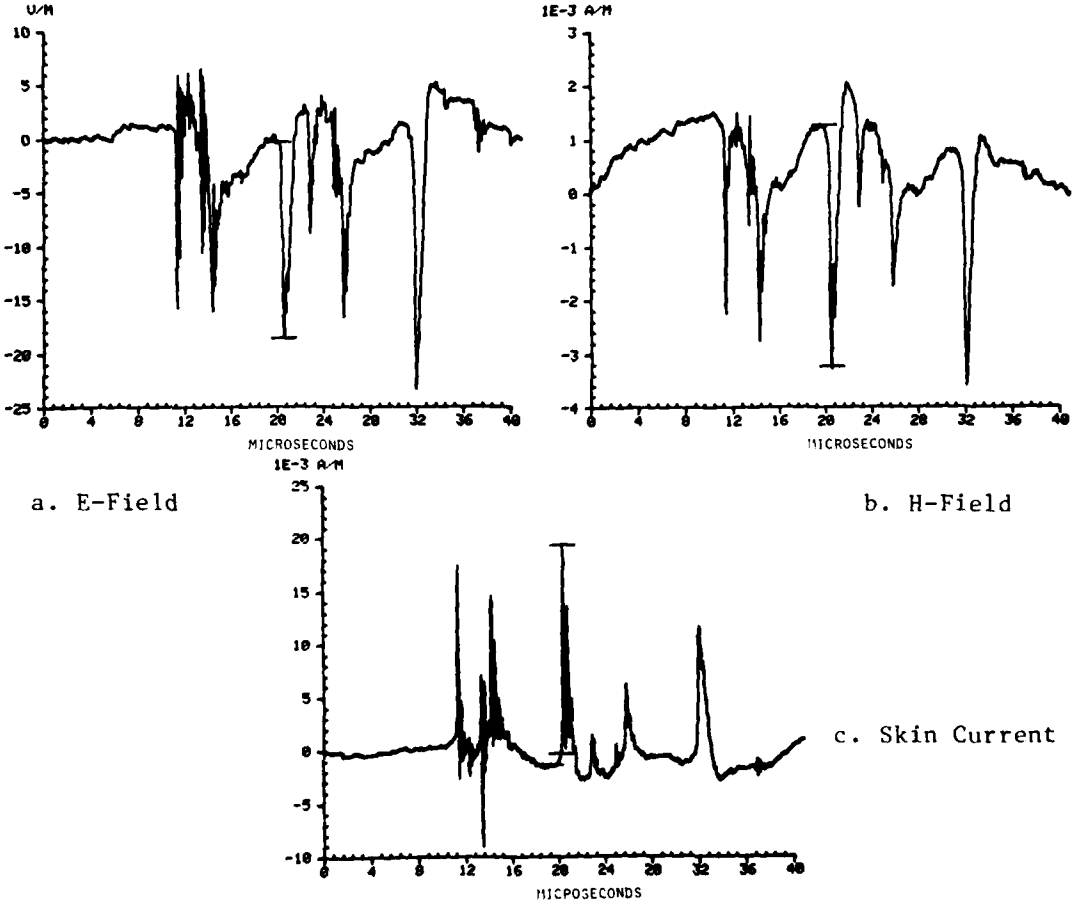

a. E-Field

b. H-Field

c. Skin Current

Figure 13. Typical Electric and Magnetic Field Pulse Waveforms and Corresponding Induced Aircraft Skin Current

EXPERIMENTAL RESOLUTION OF SYSTEM RESONANCES PRODUCED BY SIMULATED LIGHTNING EXCITATION

J. E. Lenz, D. W. Clifford and W. G. Butters
McDonnell Aircraft Company
McDonnell Douglas Corporation
St. Louis, Missouri

ABSTRACT

Laboratory studies of the electromagnetic response of aircraft-type structures to lightning-type excitations reveal that the response is in the form of damped sinusoidal waveforms containing frequency components which can be related to specific geometrical properties of the test article and other elements of the test circuit. Measurements were made of high-frequency skin currents on a long cylindrical test object whose length could be varied in 2.5 m increments. EMP-type B-dot sensors were used to make the measurements with the cylinder initially hard-wired into the high-voltage generator circuit. The cylinder was then isolated from the test circuit by using long sparks to complete the circuit from the generator, through the cylinder, to ground. In the final case, skin currents were set up by radiated E-field excitation of the cylinder. Fourier transforms of the measured skin currents showed that in the first two cases the resonance peaks related to the length of the cylinder were overshadowed by resonance peaks related to the test circuit configuration. This paper will present the results of these experiments and will discuss the implications for lightning testing of vehicle avionics systems.

Introduction

During simulated lightning tests of full-scale aircraft or large aircraft structural components, it has been observed that the transient signals measured on internal wiring exhibit damped sinusoid components with frequencies characteristic of the circuits' physical configuration.[1,2] It was assumed that the circuits were being excited by simulated lightning return stroke currents flowing on the aircraft skin. Tests on an isolated cylinder showed that transients on internal circuits could be excited by fast-changing E-fields irradiating the structure or by high-voltage streamer attachment to the cylinder prior to the arrival of the return stroke current pulse.[3,4] Regardless of the excitation source, the induced oscillatory transients on the internal wires did not change in frequency although the amplitude varied with different excitation sources.

Observation of the primary discharge current waveforms usually indicate the presence of high-frequency resonances superimposed on the low-frequency driving current. Analyses of other test results[5] indicated that test circuit parameters other than the aircraft could influence the skin currents. In addition, it was desired to know what degree of impedance mismatch might be produced by using long sparks to complete the discharge circuit rather than hard-wiring the generator to the test article. This information could help deduce the corresponding modification to aircraft resonances resulting from the long lightning arc channel attached to the aircraft. Attempts to calculate transients induced on internal circuits require a good understanding of the currents flowing on the exterior skin of the structure. For these reasons, it was decided to conduct a series of tests concentrating on the measurement of skin currents as the test circuit parameters and excitation mode were varied from the hard-wired case, to the arc-attachment case, and finally the radiated-excitation case.

Experimental Arrangements

The experimental setup has been described previously[4] and is shown photographically in Figure 1. The 1.6-MV generator used as the lightning simulator is shielded from the test cylinder electrostatically to reduce spurious excitation of the cylinder by fields radiated from the generator.

The current on the surface of the cylinder was measured at two points, using Model MGL-S74 B-dot sensors. These sensors have a sensitivity of 0.1 mV/Tesla/sec and a frequency response of

1800 MHz. The output of the skin current sensor is converted into an optical signal at the cylinder and is transmitted to the shielded screen room via fiber optics. Inside the screen room, the optical signal is converted back into an electrical signal and is stored in the memory of a Biomation Model 8100 or Model 6500 transient digital recorder. The resulting data are transferred to magnetic tape for permanent storage or for processing on the laboratory computer. The computer converts the data to the frequency domain using a Fourier transform algorithm and then feeds it to an X-Y plotter for display. The frequency response of the system is currently limited by the fiber optic units which have a bandwidth to approximately 20 MHz. Higher frequency units are being prepared for future use.

FIGURE 1
PHOTOGRAPH OF TEST SETUP

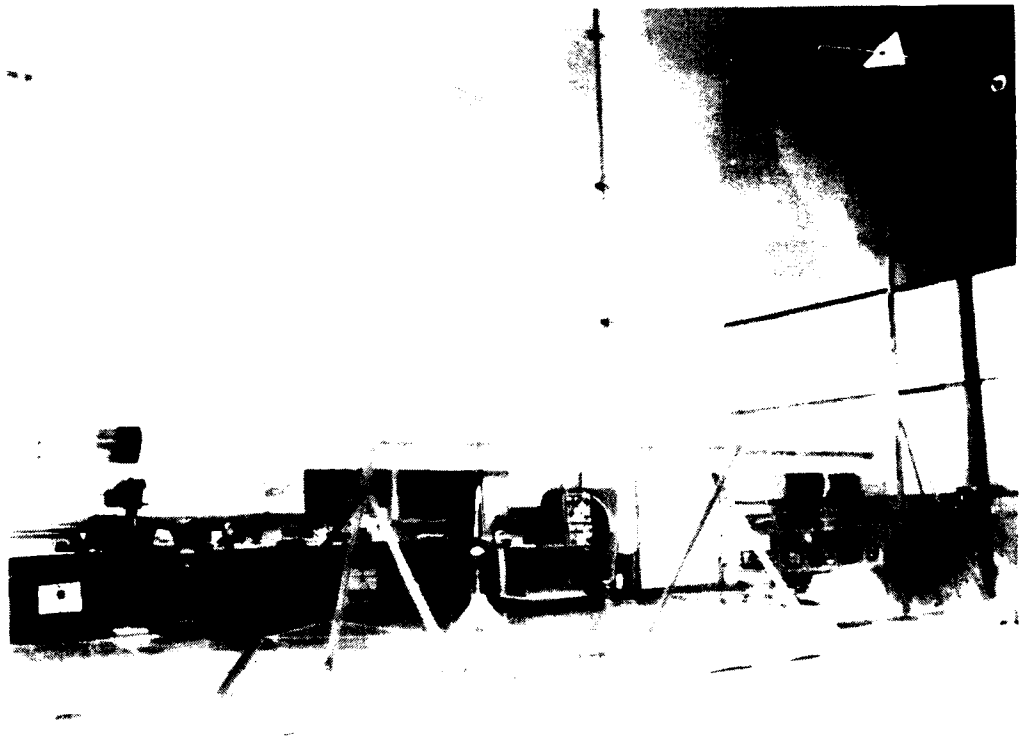

Experimental Program

During the experimental program, the cylinder was excited first by passing a current pulse from the high-voltage generator through the cylinder which was hard-wired to the generator and to ground. The connecting wires were then removed and one-meter sparks were used to connect the generator output probe to the cylinder and to connect the cylinder to ground. Third step was to irradiate the cylinder by triggering the generator with a long wire extended parallel to the cylinder about two meters above it while the cylinder was ungrounded. The series was then repeated as the length of the cylinder was varied in 2.5-meter (8-foot) increments. In each case, the skin current was measured at two points on the cylinder. One measurement was made at the generator end of the cylinder and the other at the longitudinal midplane.

A schematic of the hard-wire test case and the excitation waveform is shown in Figure 2. This is labeled a hard-wired test because there are no sparks to the cylinder, only a direct current path through it. The current waveform is measured with a current transformer at the base of the cylinder which is also used as the trigger for the transient recorders. Some evidence of circuit reflections can be seen on the current waveform.

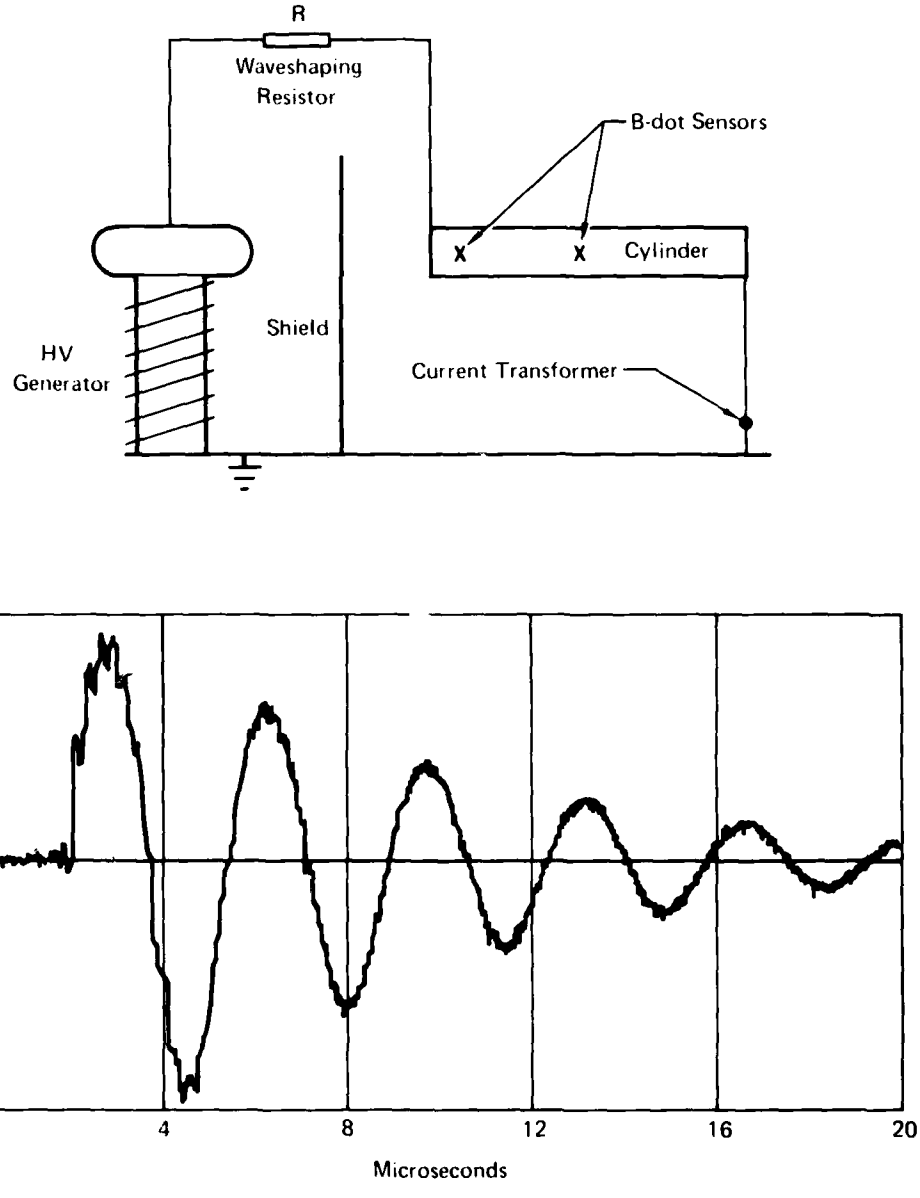

FIGURE 2
SCHEMATIC OF HARD-WIRE TEST AND EXCITATION WAVEFORM

Figure 3 shows a schematic of the double arc test and the corresponding excitation waveform measured. In this case, a more complex excitation waveform is involved, as discussed in Reference 4. At the instant voltage is applied to the output electrode, the isolated cylinder is irradiated by a rapidly changing E-field. A few microseconds later, streamers from the output probe contact the cylinder and charge it up to the output voltage of the generator. A short time later the cylinder is grounded by the lower spark and the current waveform shown in Figure 3 is recorded. In order to observe the lower energy high-frequency resonance peaks, the ground spark was taken off the same end of the cylinder as the generator spark. The source and frequency of the reflections will be discussed later.

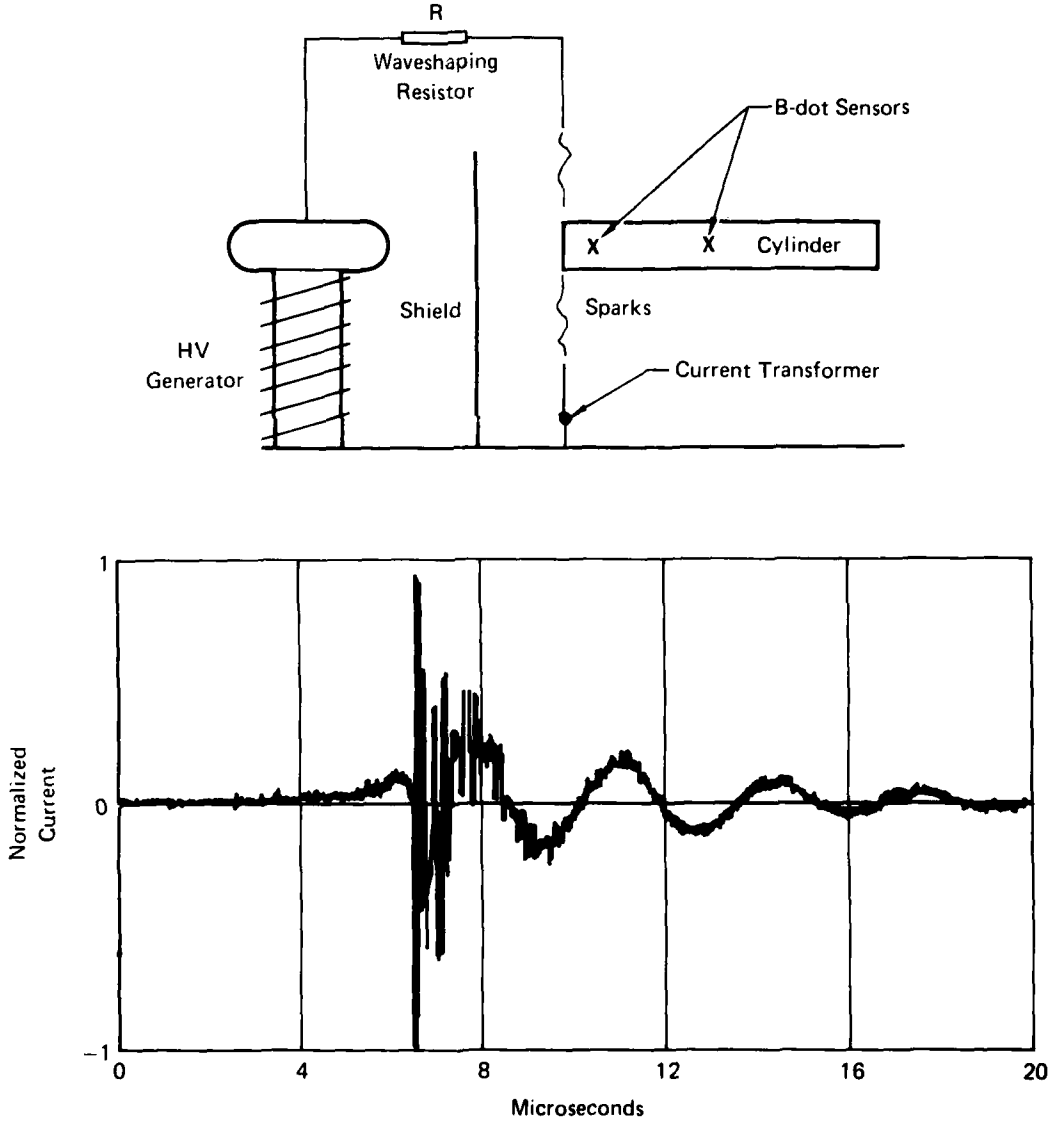

FIGURE 3
SCHEMATIC OF DOUBLE SPARK TEST AND EXCITATION WAVEFORM

In the third case, the test schematic and excitation source are shown in Figure 4. This case is called an induced test because the cylinder is not part of the main current path circuit so that any currents recorded on the cylinder are induced by transient charge on the wire. The excitation waveform shown in Figure 4 is the electric field from the wire.

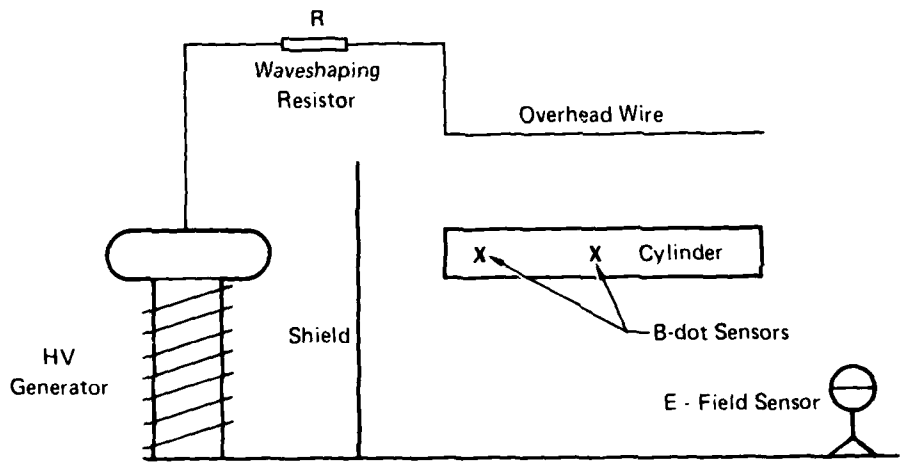

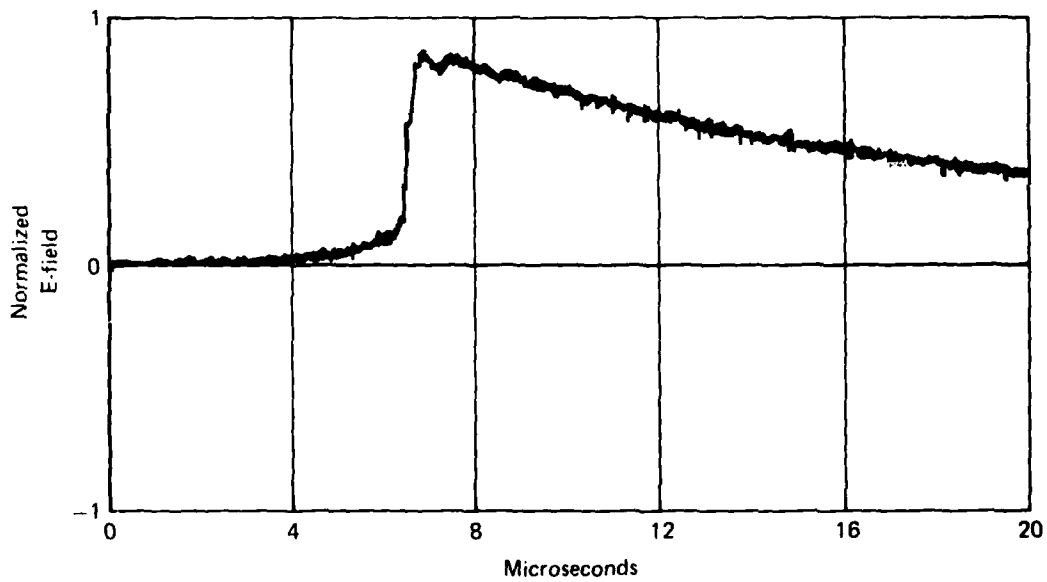

FIGURE 4
SCHEMATIC OF INDUCED WIRE TEST AND EXCITATION WAVEFORM

In each case, the output of the B-dot sensors can be related to the current flowing in the cylinder. The relationship between the magnetic field (B) and current (I) flowing in a nonmagnetic cylinder of radius r_o is: $B = \frac{\mu_o I}{2\pi r_o}$

The output from the B-dot sensors fits a numerical expression of

$$\frac{dB(t)}{dt} = Ae^{-t/\tau} (B \cos \omega t + C \sin \omega t) \qquad \text{for a single resonance.}$$

Integrating $B(t) = A\tau e^{-t/\tau} (C\omega \cos \omega t - B\omega \sin \omega t)$

thus, from above $I(t) = \frac{2\pi r_o}{\mu_o} A\tau e^{-t/\tau} (C\omega \cos \omega t - B\omega \sin \omega t)$

Most important for this paper is that the resonant frequencies and damping coefficients from the B-dot sensors are the same as that for the current transients along the cylinder.

Experimental Results

Hard-wire Case - Each test configuration was investigated for current resonances. The variation of these resonances was followed as the cylinder length was varied. Figure 5 shows the output from the skin current sensor placed at the midpoint on a ten-meter cylinder during a hard-wire test (Figure 2). The placement of the sensor along the cylinder during this hard-wire test configuration (i.e., at either end or center) has no effect on the measured waveform. During this testing, two peaks were predominate in the data. One is a low-frequency resonance near 300 kHz, and another is near four MHz. Data corresponding to a zero length cylinder were taken by running a straight wire from the generator output directly to ground, thus excluding the cylinder from the circuit. These two resonances are plotted as a function of cylinder length in Figure 6. The lower frequency is readily seen to be the total circuit resonance. It should be noted that the Fourier transform is normalized to the strongest peak. Therefore, higher frequency components could be present, but not evident.

The lower frequency can be predicted from RLC circuit theory, as shown in Figure 7. The general solution for the current in this circuit is

$$I(t) = I_o e^{-t/\tau} . (A \cos \omega t + B \sin \omega t) \text{ where } \tau = \frac{2L}{R} \text{ and } \omega = 2\pi f = \sqrt{1/LC - R^2/4L^2}$$

Using the values of the circuit components shown in Table 1, the circuit is underdamped, and the damping factor (τ) and the resonant frequency (f) agree with the measured data. The cylinder adds a small inductance to the circuit which varies only slightly with cylinder length. This underdamped waveform was used rather than a double exponential waveform simply to provide a more graphic demonstration of the relative frequencies involved in this type of test.

After some investigation, it was determined that the higher frequency resonance evident in this data is characteristic of the high-voltage generator which is a rather high inductance system. A hard wire test was done with a different (low inductance) generator substituted and only the low-frequency total circuit resonance was evident. Thus, this higher resonance is characteristic of the external circuit configuration used during the testing. The linear variation of this resonance with cylinder length can be attributed to increasing loop inductance.

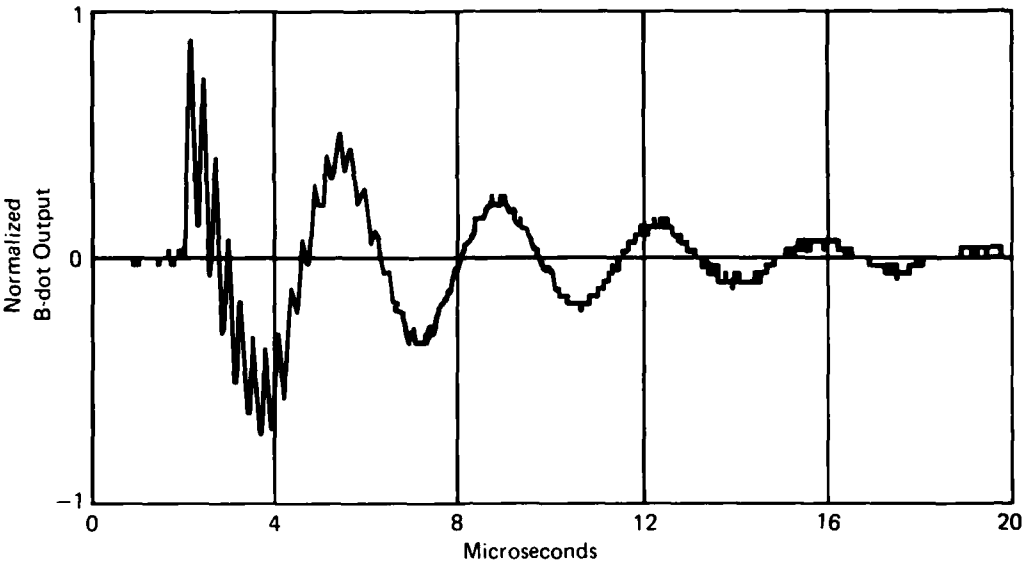

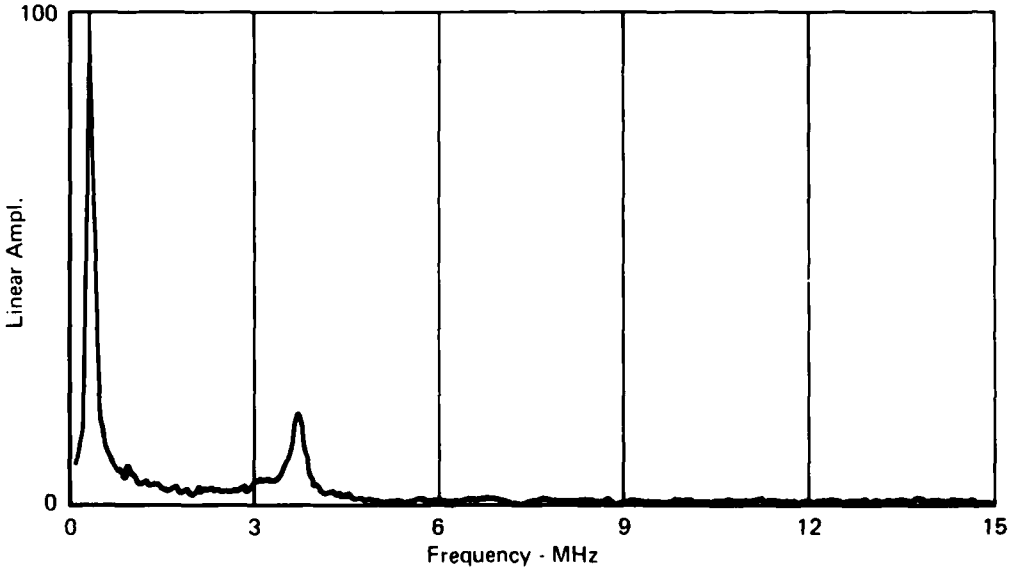

FIGURE 5
B-DOT SENSOR OUTPUT DURING HARDWIRED TEST OF 15 METER CYLINDER AND CORRESPONDING FOURIER TRANSFORM

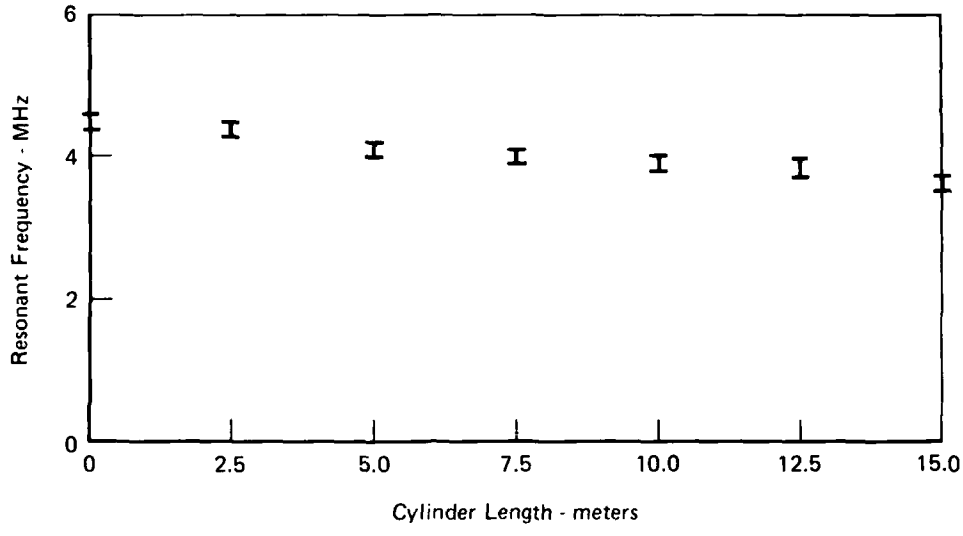

FIGURE 6
CURRENT RESONANCES ON CYLINDER DURING HARD-WIRE TEST

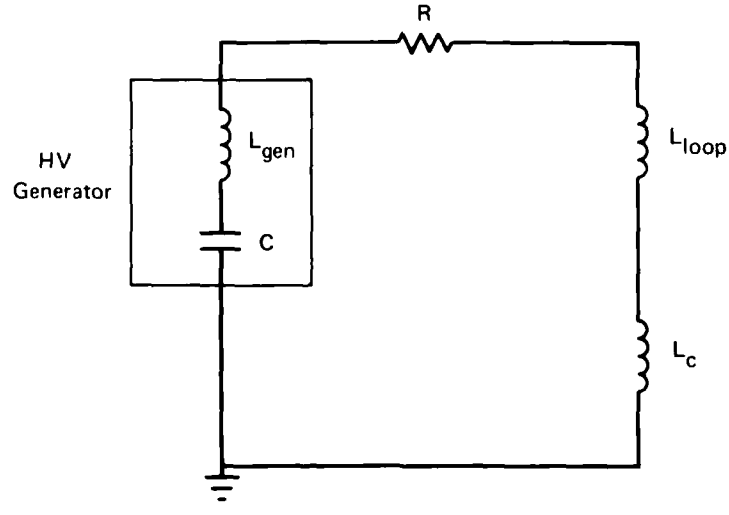

FIGURE 7
EQUIVALENT CIRCUIT DURING HARD-WIRE TEST

TABLE 1
VALUES OF CIRCUIT COMPONENTS

Generator Capacitance	C = 6060 pf
Circuit Inductance	$L_T = L_{gen} + L_{loop} = 46.3\ \mu h$
Damping Resistor	R = 22 Ω
Inductance Due to Cylinder	L_C = { 0-Straight Wire 3.3 μh-Cylinder in Circuit

(1) Circuit is underdamped
(2) Damping factor $\tau = 4.2\ \mu sec$
(3) Resonant Frequency $f = 1/2\pi\sqrt{LC}$ = { 300KHz Straight Wire
290KHz Cylinder in Circuit.

Double Arc Case - Data from a double arc test (Figure 3) on a ten-meter cylinder are shown in Figures 8 and 9 with the corresponding Fourier transforms. The ground spark was located at the same end as the attach spark, so that the total circuit current did not appear as skin current in this series. In Figure 8, the skin current sensor placement is near the arc attach point on the cylinder, and in Figure 9, the skin current sensor placement is near the cylinder's longitudinal center. The closer the sensor is placed to the arc attach point on the cylinder, the more the generator circuit resonance is recorded. A new resonance peak is evident in Figures 8 and 9 in addition to the peak discussed previously in the hard-wire test (Figure 5). This new higher frequency resonance, which is not the natural resonance of the cylinder, dominated the cylinder's skin current; it is plotted versus cylinder length in Figure 10. Note that a bar is plotted off each data point. This corresponds to the bandwidth of the resonance peak shown in the Fourier transform.

Also shown in Figure 10 are predicted resonances which were calculated for the capacitance of the various length cylinders above a ground plane. These resonances correlate very closely to the resonance peaks observed. An equivalent circuit for this double spark test is shown in Figure 11. In this test, the cylinder is not wired to ground; thus the capacitance of the cylinder is not shorted out. When the high-voltage streamers of the upper spark attaches to the cylinder, the cylinder capacitance is charged. Once the lower spark gap is closed to ground, a resonance occurs between the cylinder capacitance to ground and the circuit inductance due to the cylinder and ground spark. This calculated resonant frequency as a function of cylinder length is tabulated in Table 2.

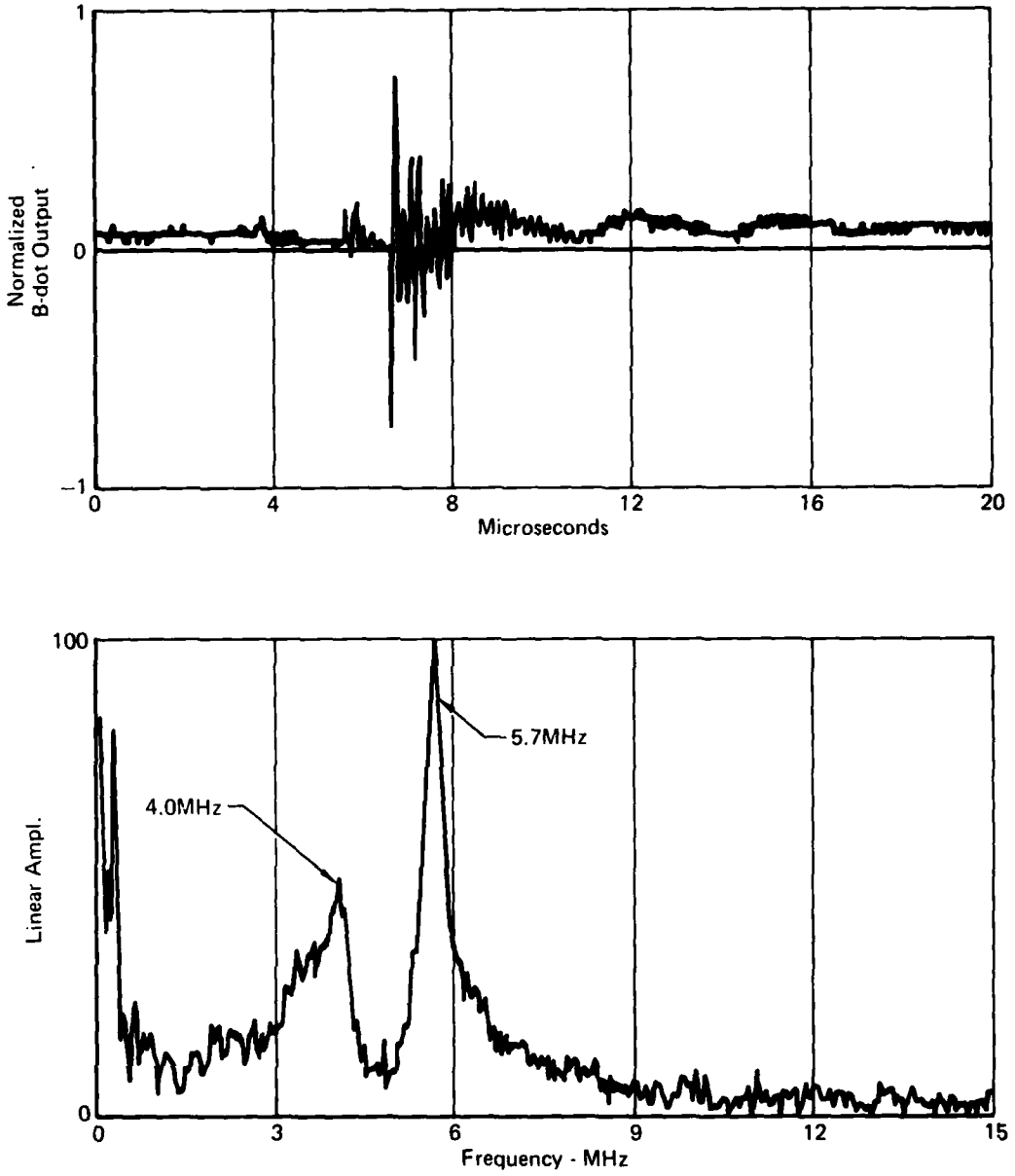

FIGURE 8
END B-DOT SENSOR DURING DOUBLE SPARK TEST ON 10-METER CYLINDER AND CORRESPONDING FOURIER TRANSFORM

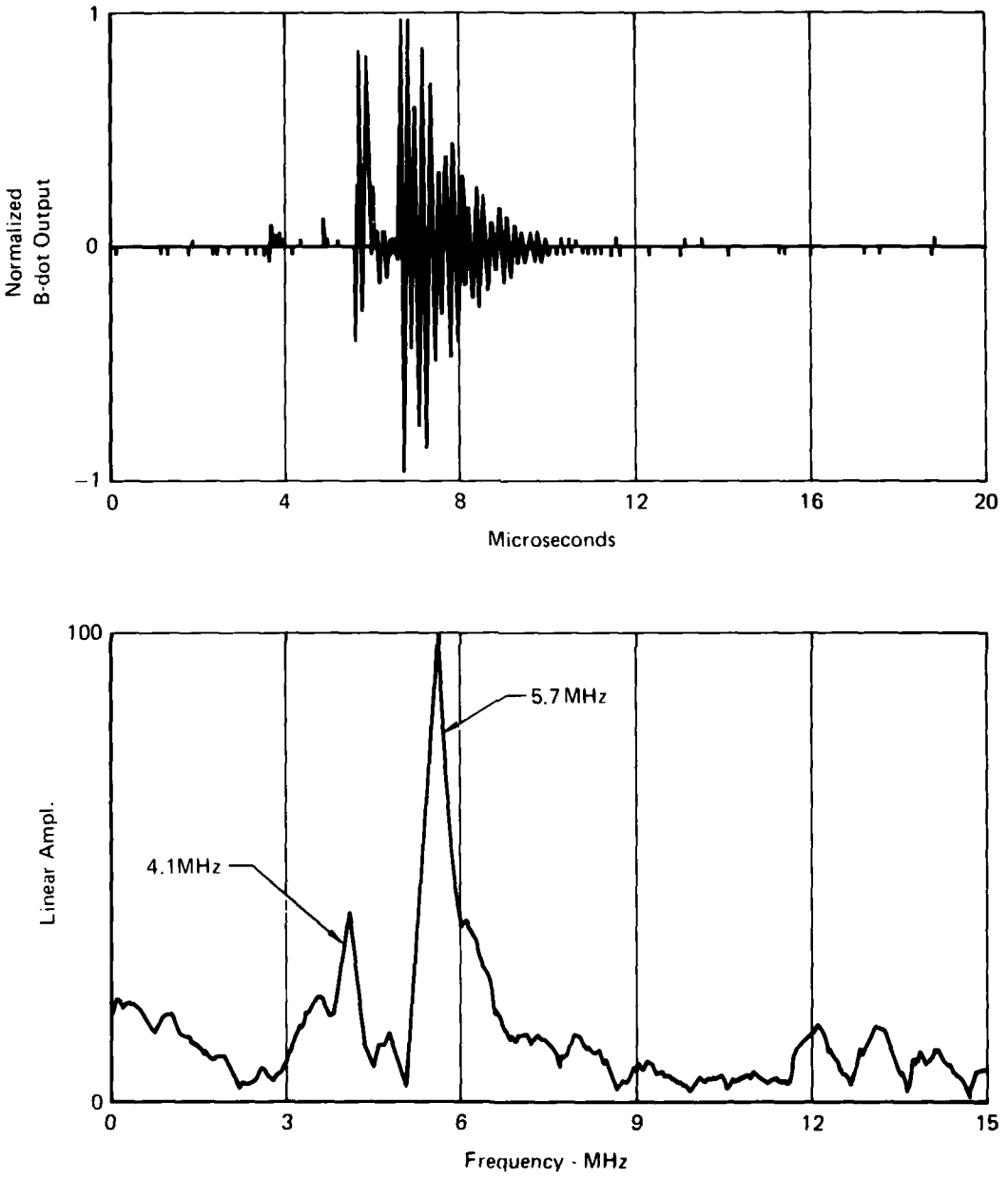

FIGURE 9
CENTER B-DOT SENSOR DURING DOUBLE SPARK TEST ON 10 METER CYLINDER AND CORRESPONDING FOURIER TRANSFORM

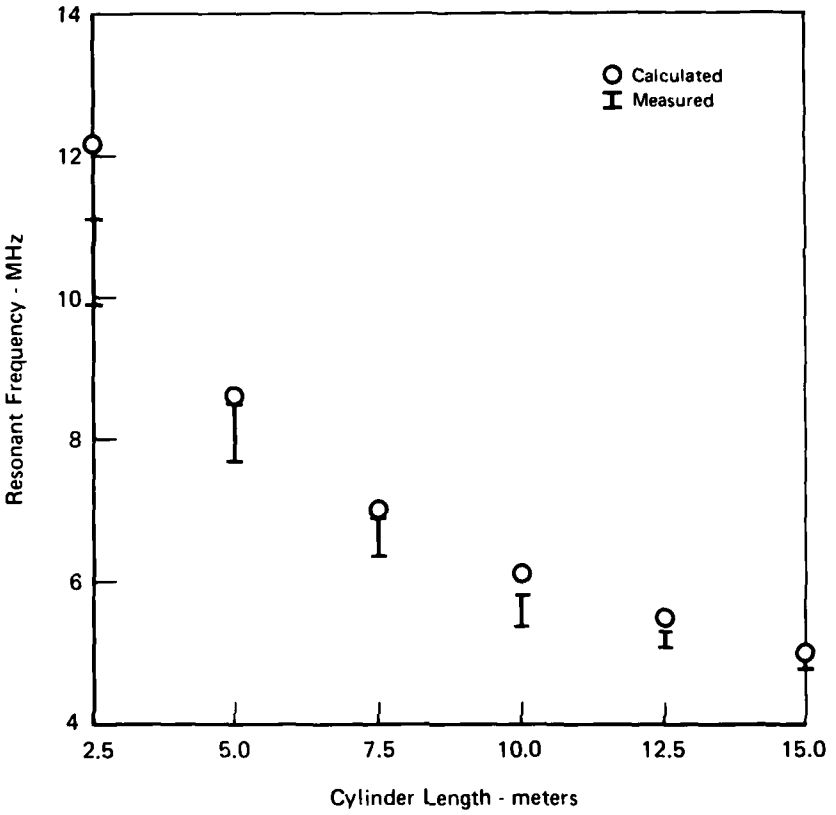

FIGURE 10
CURRENT RESONANCES ON CYLINDER DURING DOUBLE SPARK TEST

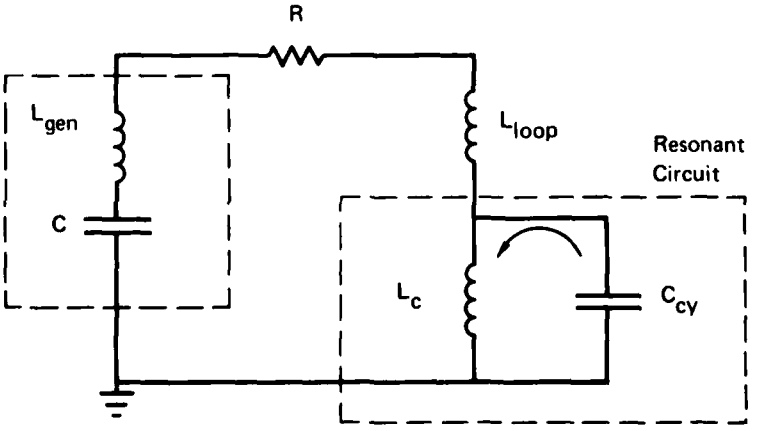

FIGURE 11
EQUIVALENT CIRCUIT OF DOUBLE SPARK TEST

TABLE 2
RESONANCE DUE TO CYLINDER CAPACITANCE

$$C_{cy} = \frac{\ell \cdot 2\pi\epsilon}{\ln(2h/r)}$$

ϵ = 8.85 pf/m
h = 1.4 m
r = .19 m

Cylinder Length (m)	L_C (μh)	C_{cy} (pf)	f_{cy} (MHz)
2.5	3.3	51.7	12.2
5	3.3	103.3	8.6
7.5	3.3	155.0	7.0
10	3.3	206.7	6.1
12.5	3.3	258.4	5.5
15	3.3	310.0	5.0

Radiated Case - A radiated E-field induced skin currents on the cylinder in the third case (Figure 4). Figure 12 shows an example of the output from a skin current sensor on a ten-meter cylinder during this test and the corresponding Fourier transform. The placement of the B-dot sensors along the cylinder has no effect on the output waveform. The resonance peak dominant in this test configuration is plotted versus cylinder length in Figure 13. For the 2.5- and 5.0-meter cylinders, a resonance peak was not evident in the data due to the 20-MHz limit of the data acquisition system.

Also shown in Figure 13 are curves predicting the natural resonance of the cylinder as a function of the speed of the skin current along the cylinder. Since the cylinder is physically isolated from the discharge circuit, resonances due to RLC circuit components will not be present. The cylinder simply acts as an antenna which is excited by external field changes. A natural resonance due to the length of the cylinder (ℓ) and the propagation velocity of the skin current can be computed. A travel time, t, for the length of the cylinder can be computed as: $t = \ell/ac$ where a is a fraction of the speed of light, c, that corresponds to the skin current propagation velocity. For an ungrounded cylinder, the frequency of the skin current would be $f = 1/2t = ac/2\ell$. Table 3 lists this calculation as a function of the cylinder length and the fraction of the speed of light. It can be seen that the measured data correspond most closely to a propagation velocity about 0.88 C.

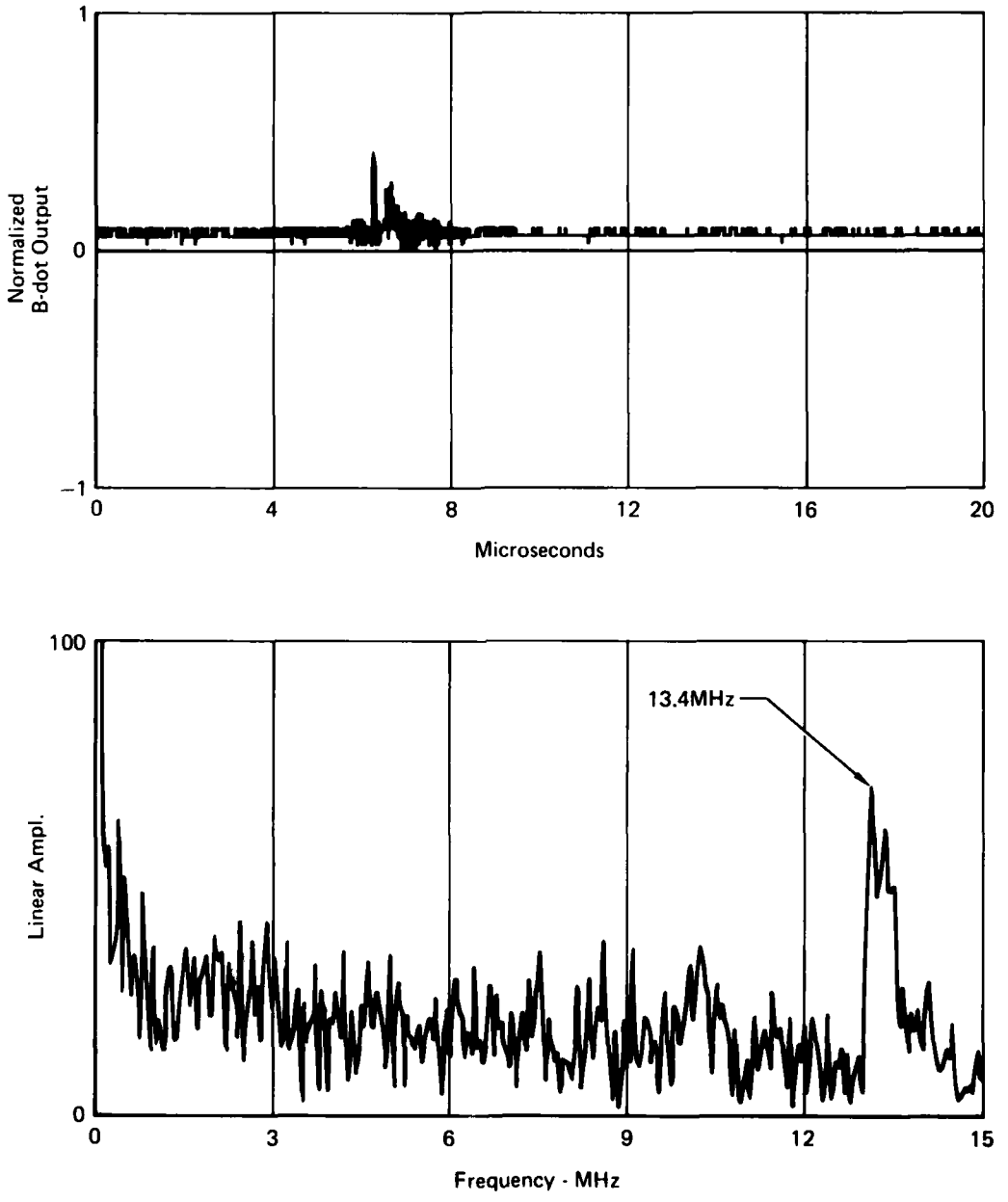

FIGURE 12
B-DOT SENSOR OUTPUT DURING INDUCED WIRE TEST OF ISOLATED 10 METER CYLINDER AND CORRESPONDING FOURIER TRANSFORM

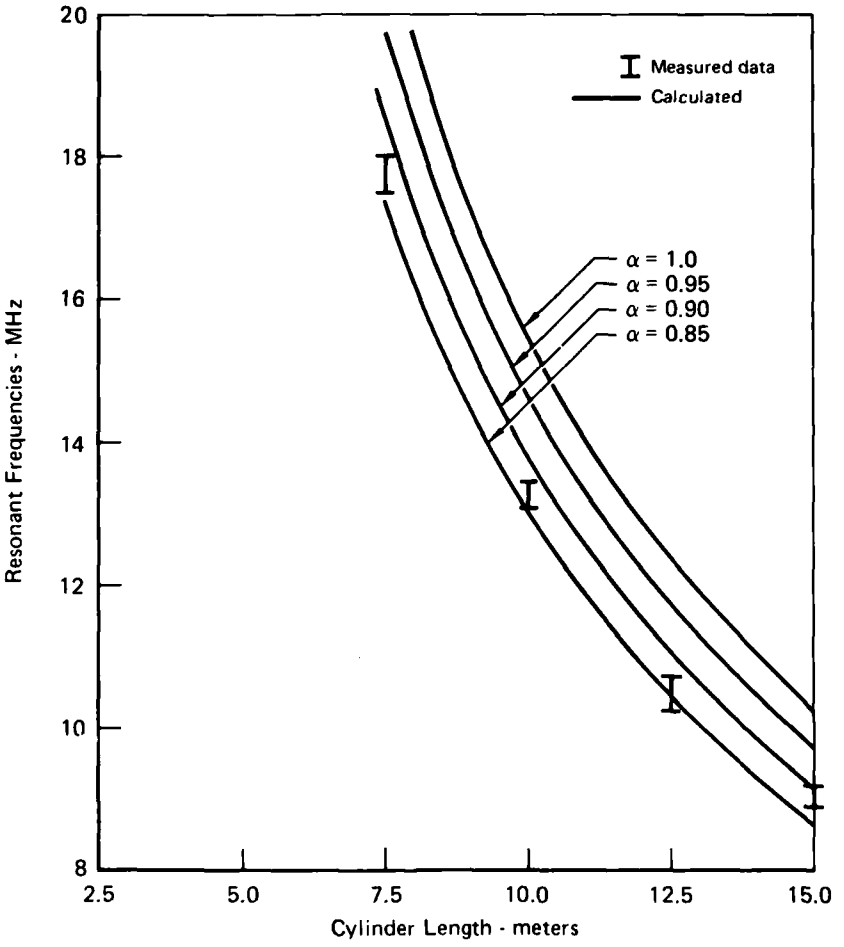

FIGURE 13
CURRENT RESONANCE ON CYLINDER DURING INDUCED WIRE TEST

TABLE 3
NATURAL RESONANCE OF FREE FLOATING CYLINDER

$$f = \frac{a.c}{21}, \quad C = 3.10^8 \text{ m/sec}$$

Cylinder Length (m)	f(a = 1.0) MHz	f(a = 0.95) MHz	f(a=0.9) MHz	f(a=0.85) MHz
2.5	61.5 MHz	58.4 MHz	55.4 MHz	52.3 MHz
5.0	30.8	29.2	27.7	26.1
7.5	20.5	19.5	18.5	17.4
10	15.4	14.6	13.8	13.1
12.5	12.3	11.7	11.1	10.5
15.0	10.25	9.73	9.23	8.7

Discussion

The results of this study are very significant for ground-based lightning tests of full-scale aircraft. They indicate that the skin currents flowing on the vehicle are dominated by interactions between the vehicle and the ground plane or by other components in the test circuit, depending on the excitation mode.

A damped oscillatory excitation waveform was used in these studies to illustrate more clearly the relative contributions of the main driving waveform and the resonances excited on the test article. It is clear from this study and previous ones,[3,4] that in the case of the hard-wired test, no significant vehicle resonances are generated if the driving waveform rise time is slow compared to the electrical length of the test article. However, resonances in the associated circuitry can be readily excited by switching transients and even relatively slow excitation waveforms. In this case, resonances characteristic of the 1.6-MV generator were obvious in all of the tests where it was used.

When the test article was isolated from ground and one-meter sparks were used to connect the cylinder into the discharge circuit, the resonant frequencies characteristic of the cylinder capacitance and inductance to ground dominated the skin currents. (The resonance due to the high-voltage generator was also present in this case.) The cylinder/ground plane resonance is excited in the spark case because the capacitance of the cylinder is fully charged to the generator output voltage before the spark to ground is established. When the path to ground is established, the charge on the cylinder rapidly discharges to ground, leading to the resonance peak observed.

In previous tests,[4] it was seen that the magnitude of transients produced on an internal wire pair were greatly increased when the cylinder was allowed to spark to ground rather than being hard-wired. It cannot be seen from the double spark data presented in this paper how the main excitation current amplitude compares to the cylinder to ground resonance current. However, the data reported in Reference 4 indicates that they are comparable in amplitude, while the rate of change of the cylinder/ground resonance current is more than an order of magnitude greater. Therefore, the high frequency resonance would be expected to dominate the coupling to internal circuits.

Only in the case of the irradiated cylinder was the basic cylinder resonance observed. With no physical connection to ground, the EM wave propagation time on the cylinder determined the response frequency of the cylinder. The response magnitude was quite low compared to the direct drive cases. The observed resonance corresponded to a wave propagation velocity on the cylinder of about 0.88 times the speed of light.

Conclusions

The role of system resonances in the production of lightning-induced transients in aircraft are of primary importance. The skin current resonances observed in the hard-wire test are characteristic of the total ground test circuit configuration. The resonances observed in the shock excitation test (double spark case) are characteristic of the vehicle to ground coupling and may or may not be a resonable simulation of the in-flight condition. More work is needed, both experimental and analytical, to determine the effect of lightning arc attachments on aircraft system resonances. The result of this test series give some indication that impedance mismatches between the vehicle and the arc channel may not be so great as to allow the basic vehicle resonance to dominate. The primary resonance in the natural lightning case may be more nearly related to the surge impedance of the arc channel and the electrical parameters of the aircraft. Skin current measurements on research aircraft struck by lightning are needed to fianlly clarify this issue. Such measurements may be forthcoming from planned government in-flight lightning research programs.

REFERENCES

[1]C. D. Skouby and G. R. Smith, "Survivable Flight Control System Lightning Susceptibility Evaluation," AFFDL-TR-75-160 (February 1976).

[2]J. A. Plumer, "Lightning Effects on the NASA F-8 Digital Fly-by-Wire Airplane," 1975 Lightning and Static Electricity Conference, Culham Laboratory, England (14-17 April 1975).

[3]W. G. Butters and D. W. Clifford, "Lightning Induced Electrical Transient Testing on Aircraft Wiring Systems," 1977 IEEE International Symposium on EMC, Seattle, Washington (August 1977).

[4]D. W. Clifford and K. S. Zeisel, "Evaluation of Lightning Induced Transients in Aircraft Using High-Voltage Shock Excitation Techniques," 1979 IEEE International Symposium on EMC, San Diego, California (October 1979).

[5]D. F. Strawe, M. O'Bryne, and S. Sandberg, "Electromagnetic Coupling Analysis of a Lear Jet Aircraft," AFFDL-TR-78-121 (September 1978).

IMPLEMENTATION AND EXPERIENCE WITH LIGHTNING HARDENING MEASURES ON THE NAVY/AIR FORCE COMBAT MANEUVERING RANGES

J. E. Nanevicz and E. F. Vance
SRI International

ABSTRACT

This paper describes the development and implementation of lightning hardening treatements on a medium-size ground installation. The treatments are discussed in light of the topological-zoning concept of electromagnetic shielding.

The first-level treatments have been implemented on the Tracking Instrumentation Subsystem (TIS) of the Navy Air Combat Maneuvering Range (ACMR) with great success. Prior to the implementation of these treatments extensive component damage occurred when the antenna tower associated with the system was struck by lightning. Since the implementation of recommended treatments many direct strikes to the same antenna have been witnessed by operating personnel without any damage to components in the treated system and with no loss of operating time on the range.

I INTRODUCTION

As is indicated in the companion paper (ref. 1), shield topology offers a powerful tool for the development of lightning hardening techniques. system topology was first introduced as an aid to the analysis of the system response to incident EMP.[2] It has since evolved into a powerful tool for decomposing very complicated systems into simple elements such as transmission lines, antennas, cavities, apertures, etc., that are amenable to analysis.[3,4]

The concept of shield topology is also extremely useful in designing system hardness.[5,6] Whereas susceptibility analysis uses topology to separate a system into tractable pieces, the system designer must reverse the process to synthesize a shield topology that will restrict penetration of lightning-induced effects to a tolerable level. This must be done without unduly compromising the performance of the primary functions of the system and without radically increasing the cost of the system.

In general, interference control is concerned with separating undesirable sources from susceptible circuits. The perfectly conducting closed shield completely isolates the volume enclosed by the shield from electromagnetic sources outside the shield (Figure 1). Therefore, if a system could be enclosed in such a shield, it would be completely immune to lightning, and other external sources of interference.

However, a serious practical limitation on the use of perfect shields is the fact that such a closed system does not allow electromagnetic signals to enter or leave the system. Since a system with which one cannot communicate is not useful, the shield is almost always compromised to allow information to flow into and out of the system. Further compromises are also usually necessary to supply power, to dispose of waste heat and to allow access for equipment installation and service. These deviations from the perfect shield mean that two or more levels of shielding may be required to protect small-signal circuits from lightning. An example of a two-level shield system is shown in Figure 2.

Conceptually, the development of a system hardening approach involves defining shield boundaries and then striving to control the violations of shields created by apertures or penetrating conductors. These concepts were applied to Navy/Air Force Air Combat Maneuvering Range Instrumentation Systems (ACMR/I) as was discussed in Reference 7. Since the ACMR/I is an operating system, treatments had to be applied gradually on a non-interference basis. At present, virtually all of the recommended first-level treatments have been implemented and will be discussed here, together with an indication of the improvements achieved in system lightning immunity.

II THE SYSTEM

The Navy/Air Force Air Combat Maneuvering Range/Instrumentation (ACMR/I) system consists of remote tracking antennas, a tracking instrumentation subsystem (TIS), and a control computing and recording facility located at a Navy or Air Force training range. Our concern here is with the TIS. The TIS consists of two all-metal vans. One of these vans contains electronic data processing and communication equipment. The vans are installed within communication range of the remote range tracking antennas, with which they communication through a tower-mounted VHF antenna located within a few meters of the vans. The radio antenna tower is normally about 156-m tall and is a frequent target for lightning.

A sketch of a typical TIS layout is shown in Figure 3. The equipment in the van is operated from commercial power, and local telephone service is provided to the vans. Both the power amplifiers for the transmitting antennas and the preamplifiers for the receiving antennas are mounted on the tower base about 1 m above ground. Coaxial cables run from these amplifiers up the tower to the antennas, and also from the amplifiers to the equipment van. Power cabling runs from the van to supply the amplifier operating power. The all-metal equipment van is grounded externally by a large cable connected to a steel supporting beam on the underside of the van and to the tower footing about 10 m away. The ac power system is grounded to one or more ground rods located 5 to 10 m from the van near the distribution transformers.

From the topological zoning point of view, the TIS originally had the configuration shown in Figure 4. The shield provided by the metal skin of the van was violated in a number of places, and the high currents induced by lightning on these penetrating conductors could flow to the sensitive equipment contained in the cabinets.

The treatments recommended to improve the lightning hardness of the TIS illustrate an important basic concept for maintaining shield integrity. They will be discussed in the next section.

III HARDENING TREATMENTS

Basically, the hardening techniques employed in the TIS involve the application of the concepts discussed in Figure 5 of Reference 1, which, for completeness, is reproduced here as Figure 5. Although two similar installations were considered in the hardening program discussed in Reference 7, only the installation at Nago Head will be discussed.

A metal entry panel connected to the skin of the van was installed where the coaxial cables enter the van in Figures 3 and 4. Cable connectors were installed in the entry panel to connect the shield to the panel thereby forcing the harsh lightning currents flowing on the coaxial cable shield to flow to the outside of the skin as suggested in the left illustration of Figure 5(b).

The ac power lines were treated as is suggested in the left of Figure 5(c). A secondary lightning arrester was installed on each of the incoming lines to "close the aperture" and divert the line current to the outside skin whenever the magnitude of the line voltage exceeds the surge limiter threshold as the result of a lightning stroke. Further application of Figure 5(c) was achieved by installing a line regulation transformer after the secondary lightning arrester. This unit provides voltage regulation and filtering to further limit the frequency and amplitude range of the signals that can penetrate through this aperture.

The safety wire ("green wire") was treated as suggested in the left illustration in Figure 5(a). The ac power entry details were to assure that the green-wire grounding conductor does not go outside the van, and that the outside electrical grounding conductor does not enter the van. This arrangements avoids having lightning-induced currents flowing to the interior of the van on the safety ground system, as might happen if the arrangements at the right of Figure 5(c) were followed.

The power supply leads to the preamplifiers were treated following the concept illustrated at the left of Figure 5(c). Details of the treatment are shown in Figure 6. Since the power supply is contained in an equipment cabinet, the leads penetrate two layers of shielding. In this way, amplitude limiting was applied at the penetration of each shield. The gas tubes associated with the van shield were located in a small "dog house" installed on the entry panel discussed earlier. Thus, lightning-induced currents bypassed by the gas tube are forced to flow on to the exterior of the van skin. A TRANSZORB was installed where the power supply lead entered the equipment cabinet in order to maintain the integrity of this second shield by amplitude - sensitive shorting of the undesired lightning-induced currents to the skin of the cabinet.

Treatment of the telephone entry was of lower priority since the telephone system is not intimately connected to the rest of the system. Thus, this work is just now getting underway.

Aside from the limiting discussed in connection with the preamplifier power supply leads, no treatment at the secondary shield level has been undertaken.

IV HARDENING SYSTEM PERFORMANCE

There has been no computer damage since the RF cable treatment and ac power limiters were installed. The system has operated for the last 2 years without any damage even though the antenna tower has been struck by lightning on numerous occasions. For example, 3 direct strikes were observed by operating personnel during the summer of 1979. They also reported that at least an equal number of probable strikes occurred. If this many strikes occurred when operating personnel were present, it is reasonable to assume that a substantial number of strikes occurred when no one was present.

On Sunday, 9 March 1980, an extremely severe storm occurred at Nags Head. On the following Monday, operating personnel found that transistors in the preamplifiers located in the boxes on the antenna tower had been damaged. It should be recalled from Figure 6 that protection was applied to the power supply leads entering the van, but that no protection was applied at the preamplifier itself.

Since the lightning treatment program was initiated, no time has been lost on the range.

V CONCLUSIONS

Lightning hardening treatments developed from the shield topological point of view have been applied at the first level of shielding of a medium-size facility. Prior to the installation of these treatments, the system suffered extensive damage to electronic circuitry whenever a lightning strike occurred to the antenna tower, which was part of the system. The damage was sufficiently severe that the system had to be shut down for repair.

Since the installation of the hardening treatments, numerous strikes to the same tower have occurred during a two-year period, without causing any damage. During this same period, no range time has been lost as the result of lightning effects.

The hardening treatments were simple and straightforward to install. Actual installation occurred during times when the range was closed--because of weather or other operational considerations. The cost of purchasing the hardware and installing the treatments is much less than the expense of repairing the unmodified system after a lightning strike.

REFERENCES

1. Vance, E. F., and Tesche, F. M., "Shield Topology in Lightning Transient Control", Copanion paper in the proceedings of this conference.

2. Baum, C. E.: How to Think About EMP Interaction. Proceeding of the 1974 Spring FULMEN Meeting, Air Force Weapons Laboratory, April 1974.

3. Tesche, F.M., et al. "Internal Interaction Analysis: Topological Concepts and Needed Model Improvements," Interaction Note 248, Air Force Weapons Laboratory, Kirtland AFB, New Mexico, July 1975.

4. Tesche, F. M.: Topological Concepts for Internal EMP Interaction. IEEE Trans. A.P., vol. EMC-20, February 1978, pp. 60-64.

5. Vance, E. F.: Shielding and Grounding Topology for Interference Control. Interaction Note 306, Report No. FAA-RD-77-84, pp 331-350, FAA-FIT Workshop on Grounding and Lightning, May 1977, Federal Aviation Administration, Washington, D.C.

6. Vance, E. F., Nanevicz, J. E., and August, G. A., "Technical Inputs and EMP Design Practices for Intrasite Cabling of Telecommunication Facilities," Final Report, Contract DAAG-39-76-C-0021, June 1977.

7. Nanevicz, J. E., and Vance, E. F., "Techniques for Increasing the Lightning Tolerance of the Navy/Air Force Air Combat Maneuvering Range/Instrumentation Systems," 1979 FAA Workshop on Grounding and Lightning Protection, Melbourne, Florida, March 1979.

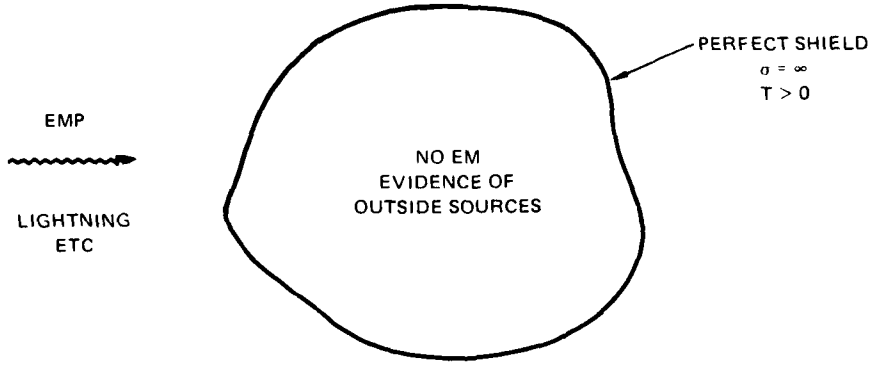

FIGURE 1 ELECTROMAGNETIC ISOLATION WITH A PERFECT SHIELD

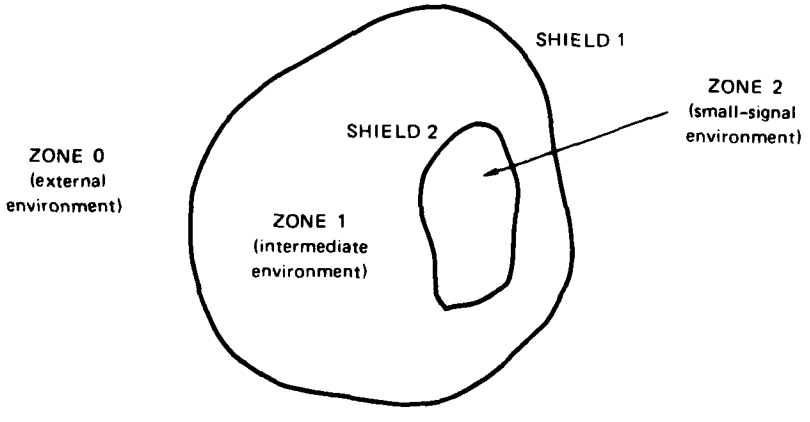

FIGURE 2 TOPOLOGY OF A TWO-LEVEL SHIELD SYSTEM

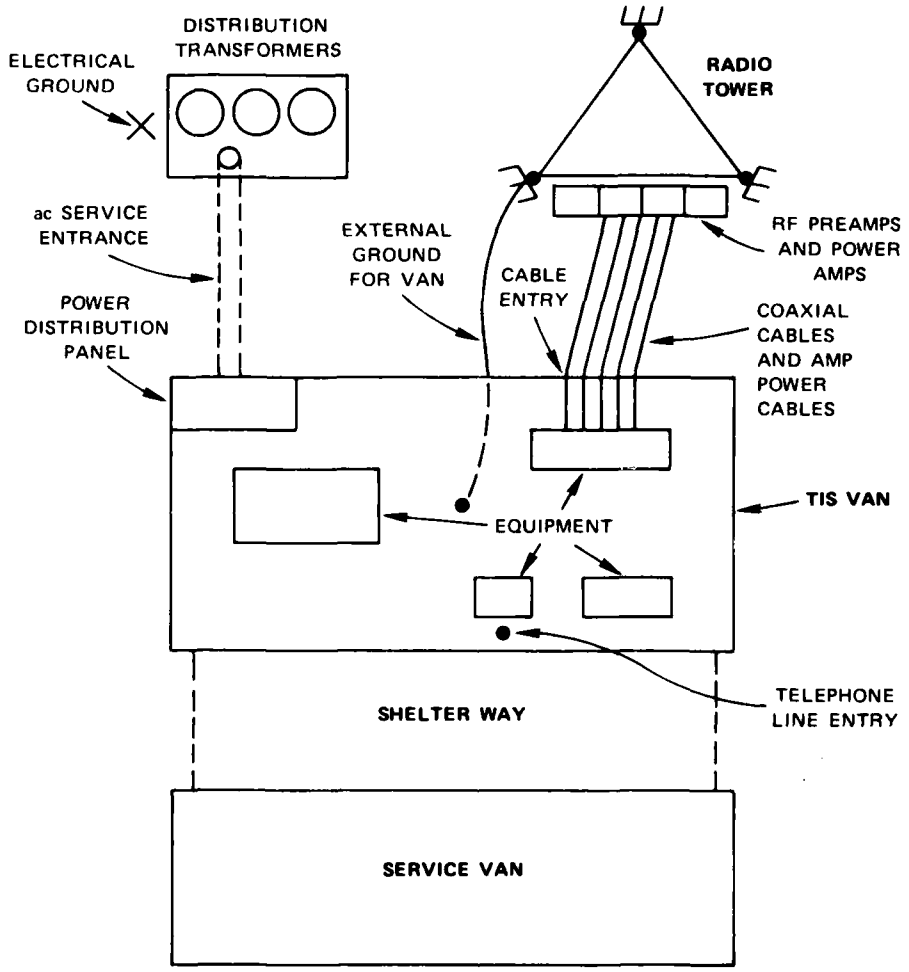

FIGURE 3 SKETCH OF A TIS INSTALLATION

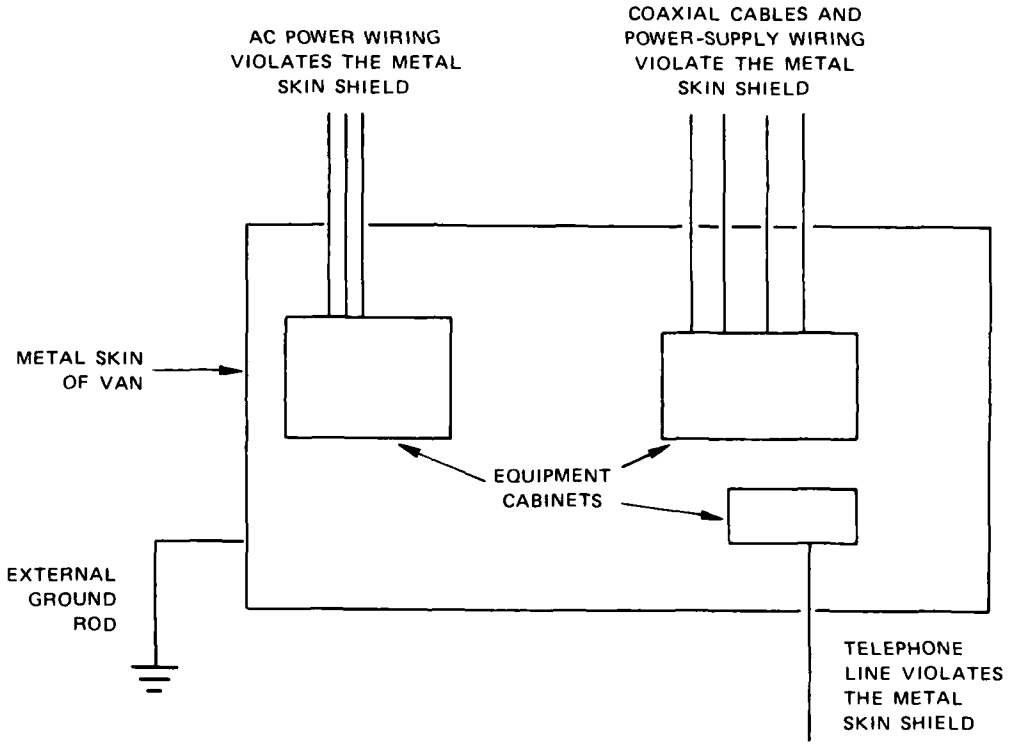

FIGURE 4 SCHEMATIC OF TIS INSTALLATION SHOWING SHIELD PENETRATIONS

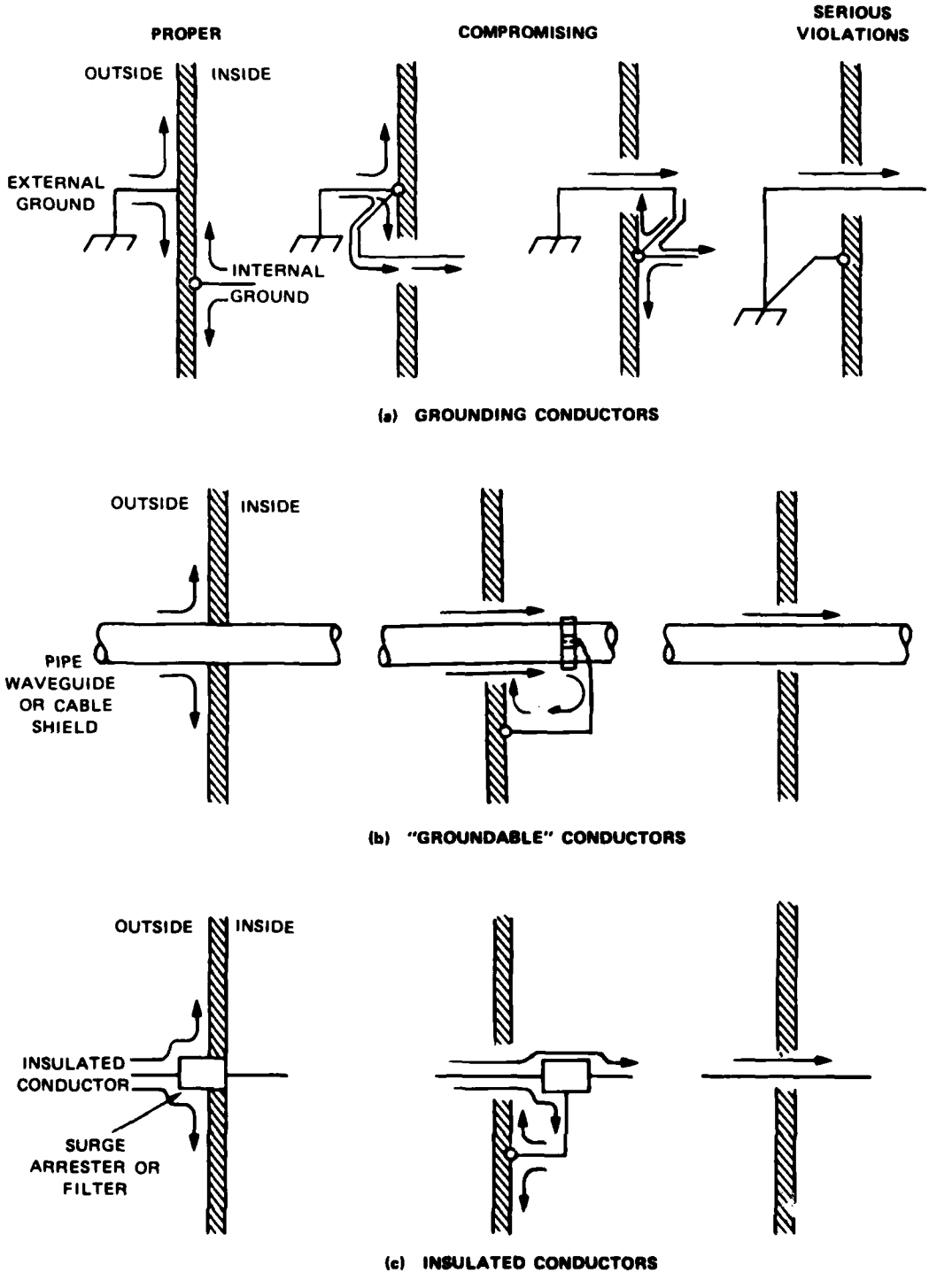

FIGURE 5 SHIELDING INTEGRITY NEAR INTERFERENCE-CARRYING EXTERNAL CONDUCTORS

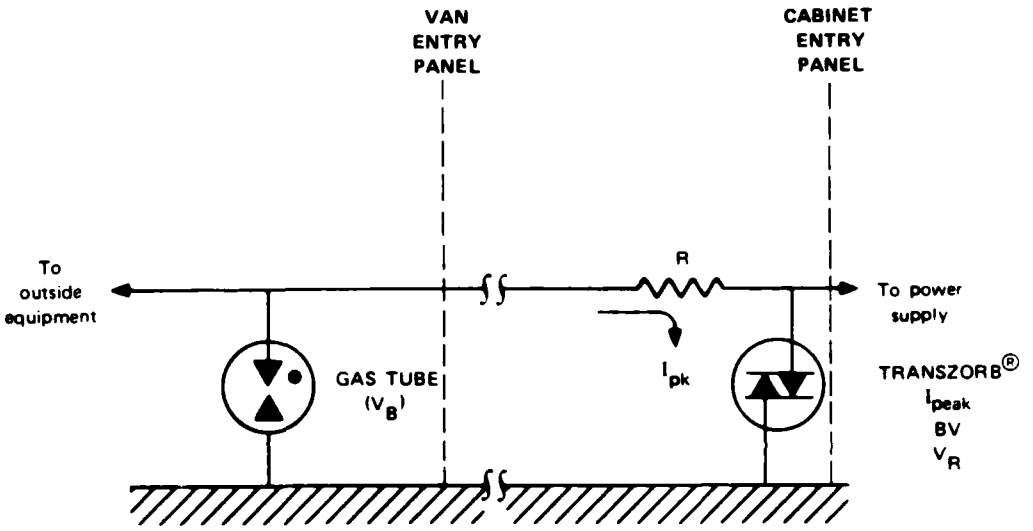

V_B = BREAKDOWN VOLTAGE OF GAS TUBE (typical values 100-300 volts)

I_{peak} = PEAK CURRENT LIMIT FOR TRANSZORB® (typical values 30-40 amperes for 30-50 V clamping voltage)

V_R = STANDOFF VOLTAGE

BV = BREAKDOWN VOLTAGE ($> V_R$)

FIGURE 6 TREATMENT OF POWER LEADS TO PREAMPLIFIERS ON TOWER

THE FAA LIGHTNING PROTECTION MODULES DESIGNED FOR LEADLESS DEVICES

Richard M. Cosel and Manuel Figueroa
Florida Institute of Technology

SUMMARY

The silicon avalanche transient suppressor is widely used to protect low level solid state devices against voltage transients. There has been a problem, however, in providing suitable low loss, low inductive installation mountings especially in retrofit cases. This report describes two mounting systems developed for the FAA, a barrier strip designated FA9455, for direct current, pulsed or audio lines and coaxial holder designated FA9479 for 50 or 72 ohm video or R.F. lines. Tests were performed using both conventionally constructed suppressors and low capacity units at voltage ratings varying from 6.8 volts to over 50 volts and including bipolar and unipolar devices. Square wave tests on the barrier strip, insertion loss tests on the coaxial module and surge testing of both modules indicated that within test parameters, the devices are limited only by the capabilities of the surge suppressor used. i.e. They are device limited.

INTRODUCTION

The use of silicon avalanche diodes for suppression of induced transients has been widely documented. The standard low power units which appeared on the market were packaged much the same as ordinary rectifier diodes, i.e. axial or stud mounting. While these were reasonably simple to wire into existing circuitry, several inherent problems surfaced. The problems mainly involved the packaging (physical arrangement) to provide protection at line termination points such as the demarcation box at a facility entrance, and the inductance (which could be significant) added by device leads.

The FAA, recognizing these problems decided to attack on both fronts simultaneously. First of all in conjunction with General Semiconductor Industries, a family of leadless devices was developed. These devices - Figure 1 - are now catalog items in breakdown voltages ranging from 6 to 115 volts in both unipolar and bipolar form. Also available are low capacity units which have been tested for insertion loss at frequencies up to 1.0 GHz.

The second task, a logical outgrowth of the first was to develop a family of suitable holders or modules which meet the following goals:

Ease of installation
Minimum lead length
Use with single or multiple twisted pair lines
Use with coaxial lines.

Through the RADC Post Doctoral program, Florida Institute of Technology was given the task of development of both a holder which would replace the typical barrier strip and a second unit for use in coaxial line. The resulting barrier strip shown in figure 2, A and B is made in two lengths. The FA9455A is a five device unit while the B version holds 10 devices. Illustration 2A shows a module with components for a typical protection circuit in stages of installation. While five or ten devices can be accommodated, this does not necessarily equate to five or ten lines. The size and shape of the diode inserts were specifically selected so that the unit would be interchangeable with available miniature gas tubes. Thus in a more complex suppression circuit, two or more positions can be used with one line. The crossover connector provided is shown at the top.

The coaxial module FA9479 Figure 3, was fabricated using a standard UG 28A/U type N Tee. As can be seen from the illustration, the throughput goes through the head of the Tee and the protection device is in the modified leg. The center line connector has been replaced with a flat head screw and insulating cup. The low capacity units available in the leadless configuration were unipolar devices. In order to accommodate two diodes for bipolar operation, the cap was redesigned, extended to provide added space. Originally a conical spring was used as the internal contact. However, because the spring had too much inductance the cap was redesigned to make use of a flat belleville washer type spring. In production, the adjustable screw would be replaced with a fixed contact.

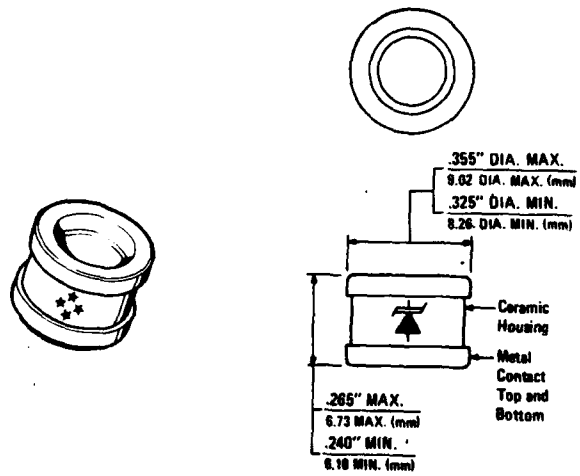

Figure 1

General Semiconductor Leadless TransZorb [C]

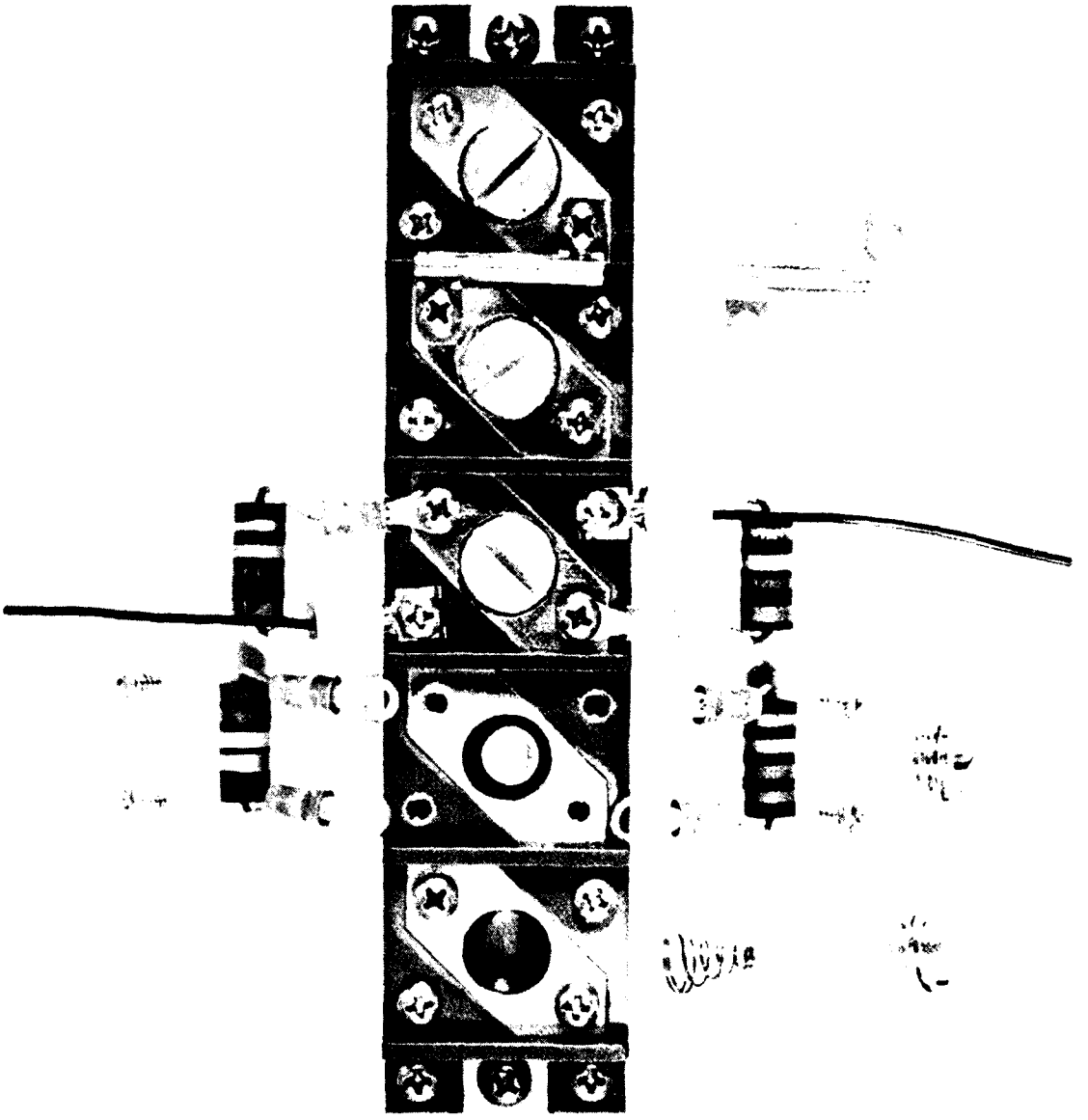

Figure 2A

Lightning Protection Module (LPM) FA9455A showing diode insertion and resistor mounting for the most common arrangement.

Resulting Circuit

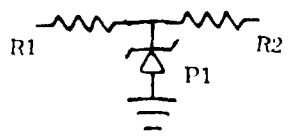

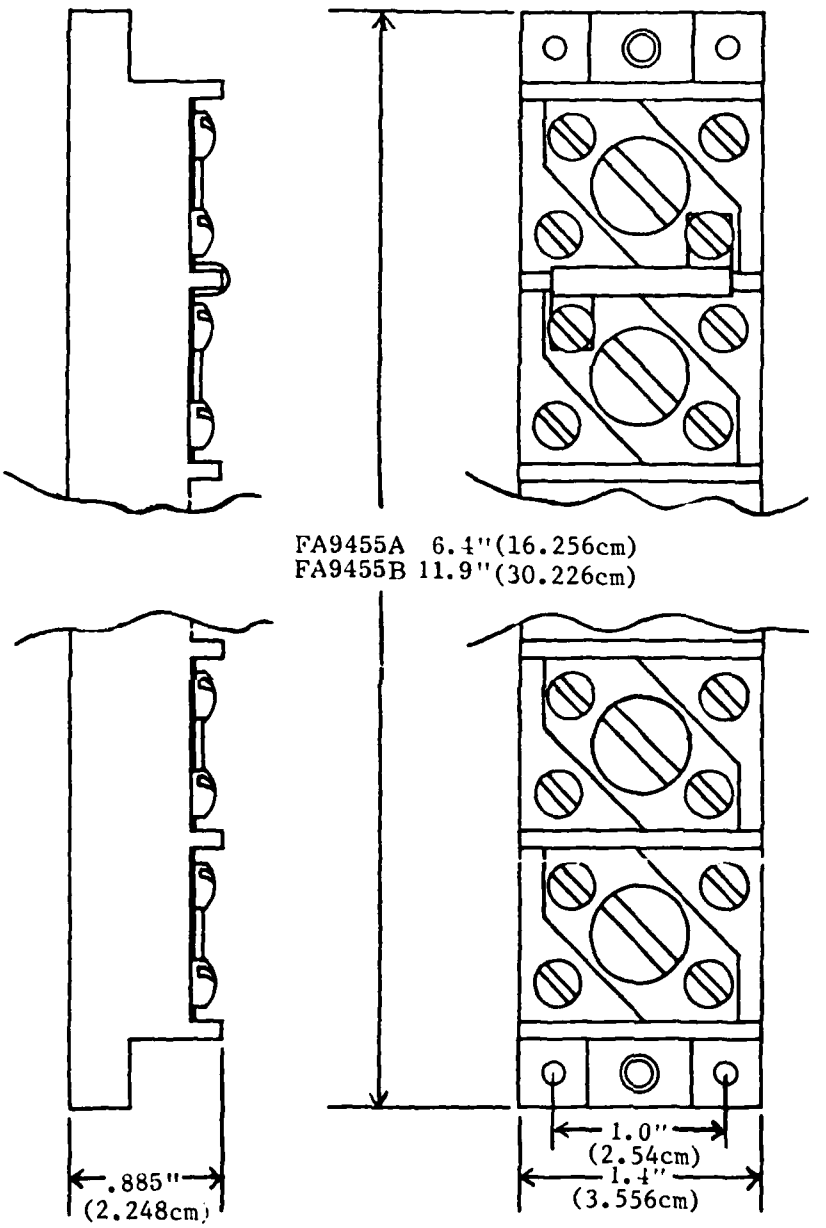

Figure 2B

Lightning Protection Module, Plan View

The 5 Terminal unit is designated FA9455 A
The 10 terminal unit designated FA9455 B

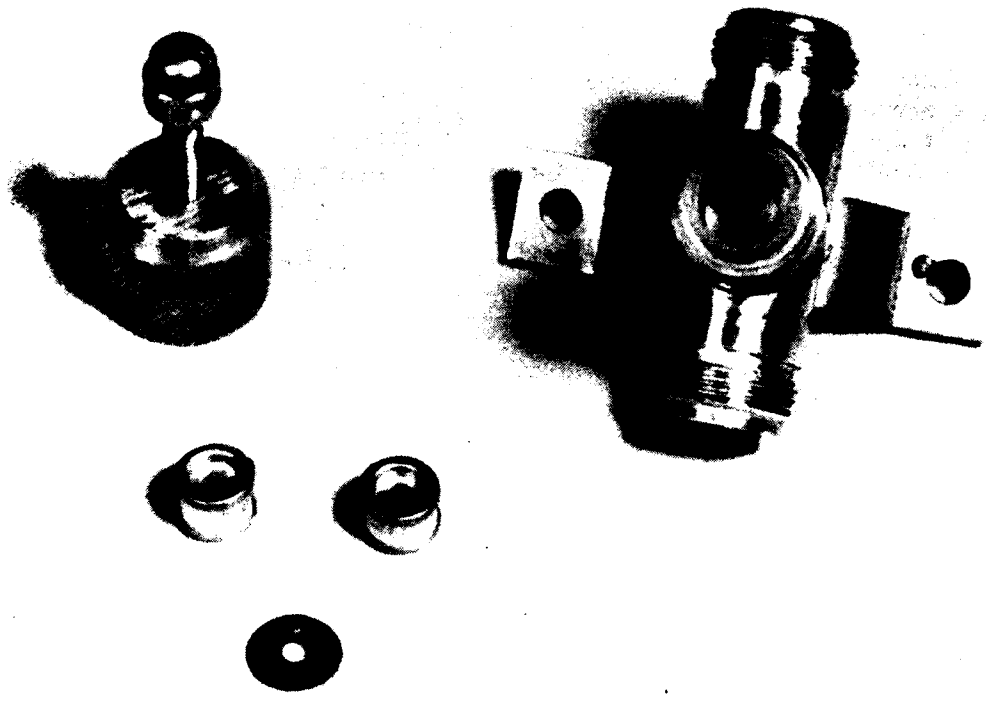

Figure 3

FA 9479

Lightning Protection Module, Coaxial (LPMC)

Note that a cupped "belleville" type washer has been substituted for the conical spring washer substantially reducing inductance effects. Space for two suppression devices has been extended using a redesigned cap. In production, the adjustable screw contact would be replaced by a fixed contact.

TEST PROGRAM

A. Barrier Strip, FA9455

Suppression Characteristics, such as peak power dissipation and breakdown voltage of the protective devices are listed in appropriate catalogs. Of specific interest in applying the devices to existing circuits is the effect the device and its holder may have on the quality and level of the signal being transmitted.

The barrier strip is commonly used to connect single or twisted pair telephone type lines. Signals include pulsed d.c. and sinusoidal signals from low frequency power (60 or 400 Hertz) and control lines and the audio frequency range.

In special cases, clock synchronization pulses up to 10 MHz are accommodated on twisted pair. However, the input and output circuitry is specially conditioned and designed to accommodate degraded pulse shapes.

1. Square Wave Tests

A series of square wave tests were run using both standard and low capacity diodes. Degradation effect of the lines themselves was minimized by using short leads and no termination in order to picture solely the effect of the suppression device in combination with the module. The square wave pulse generator used was a Hewlett Packard 211A with a maximum frequency of 1 MHz and an output of 55 volts across a 600Ω internal impedance. The rise time specification is less than .1μ sec.

The barrier strip was tested using the following devices: 1.5KC7.5, 1.5KC 36, 1.5KC51, GZ92111A, GZ92111B and the GZ60316B. All are unipolar devices. Tests with available bipolar units showed no significant differences. Test results are shown in figures 4 through 10. In each case the test voltage shown is just below the clipping point unless otherwise indicated. It is interesting to note that in this "large signal" test case, with the exception of the 6.8 volt device, GZ60316B, the apparent square wave distortion is related more to the device voltage rating than to the diode "low signal" capacitance. Thus the 36 volt devices 1.5KC36 (standard capacity) and the GZ92111A (low capacity), show essentially similar wave shapes at corresponding frequencies. The GZ60316Bs, low capacity devices of earlier manufacture had all been subjected to extensive surge testing and exhibited rounded zener knees indicative of leakage. The insertion loss curve, Figure 21, also shows an apparent resonance effect which seems to be unique to the construction of this particular series. Figures 11A and B shows the comparison of the 'knees' of the GZ260316B and GZ92111A both to the same scale of 5 volts/division. Figure 11C shows the 'knee' of the GZ60316B somewhat expanded at 2 volts/division.

2. Surge Test

Surge testing was performed using a laboratory fabricated generator, courtesy of G.K. Huddleston, Georgia Institute of Technology. The basic test circuit is shown in figure 12.

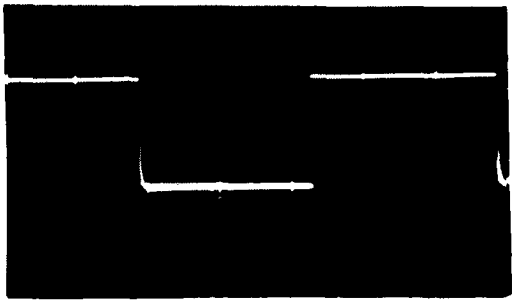

1. 1000 H_Z
   5 v/cm, 100 μsec x 2

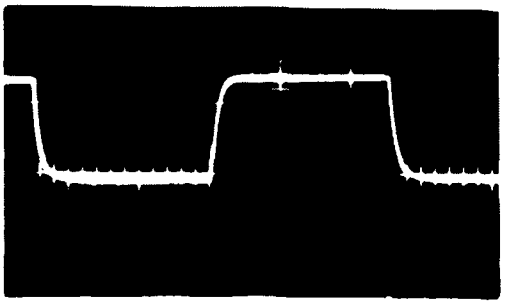

2. 10 KH_Z
   5 v/cm, 10 μsec x 2

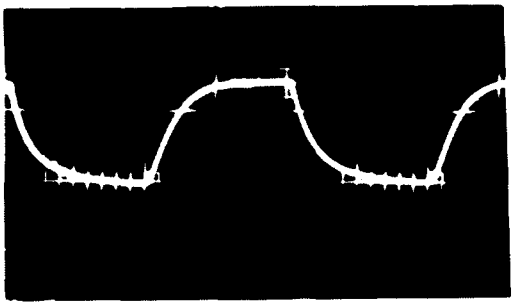

3. 50 KH_Z
   5 v/cm, 1 μsec x 5

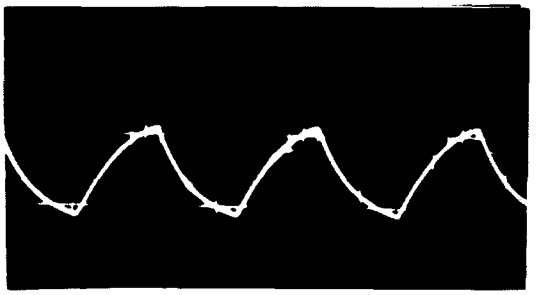

4. 100 KH_Z
   5 v/cm, 1 μsec x 5

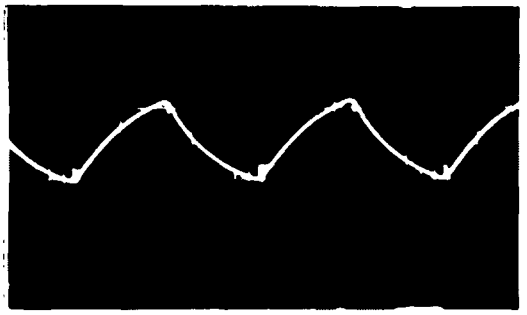

5. 200 KH_Z
   5 v/cm, 1 μsec x 2

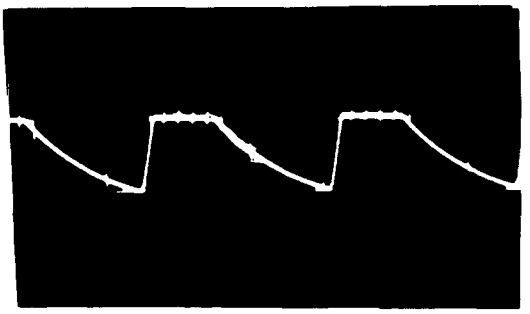

6. 200 KH_Z
   5 v/cm, 1 μsec x 2
   (Showing Clipping Action)

Figure 4
Square Wave Test
1.5KC7.5 (V_B 7.76) Mounted in LPM 9455A

1. 1000 Hz
10 v/cm, 100 μsec x 2

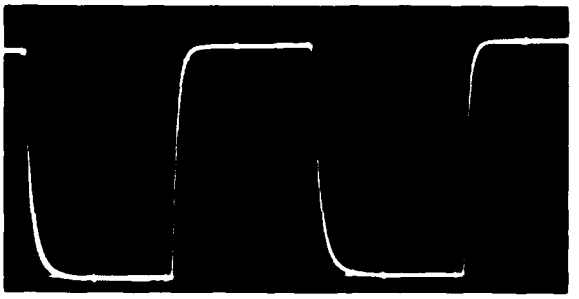

2. 50 KHz
10 v/cm, 1 μsec x 5

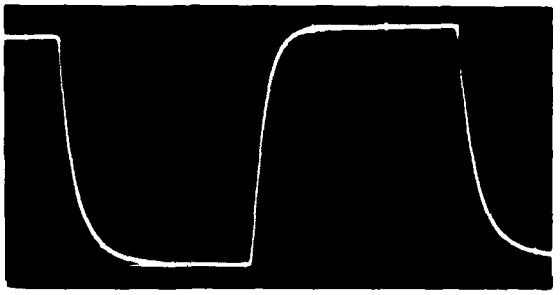

3. 100 KHz
10 v/cm, 1 μsec x 2

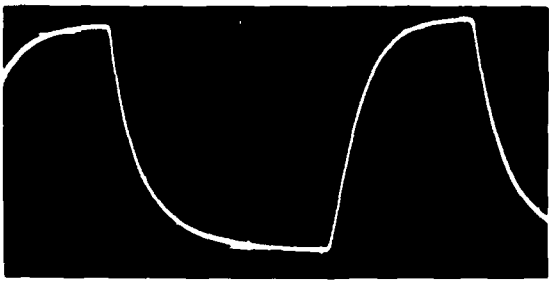

4. 200 KHz
10 v/cm, 1 μsec x 1

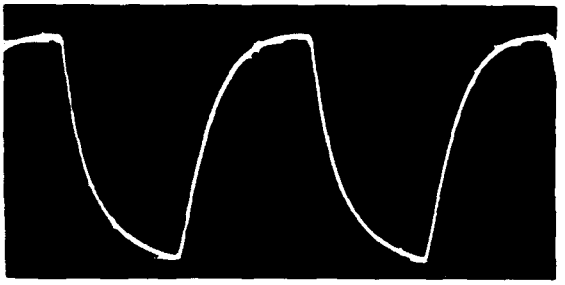

5. 300 KHz
10 v/cm, 1 μsec x 1

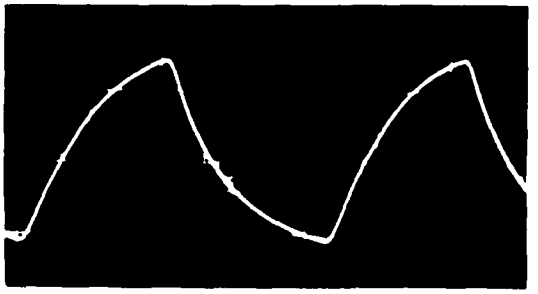

6. 500 KHz
10 v/cm, .1 μsec x 5

Figure 5
Square Wave Test
1.5KC36 (V_B 33.36) Mounted in LPM 9455A

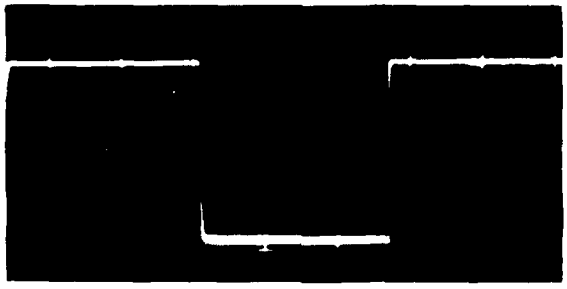

1. 10 KHz
   20 v/cm, 10 μsec x 2

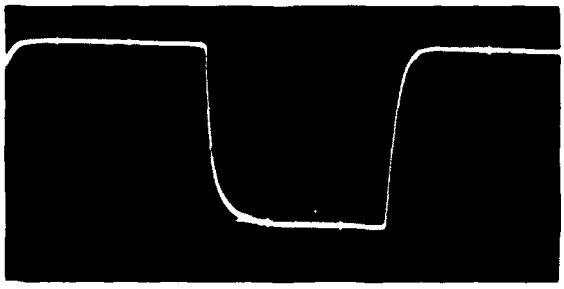

2. 100 KHz
   20 v/cm, 1 μsec x 2

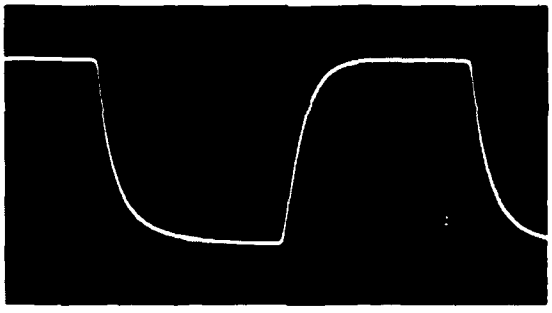

3. 200 KHz
   20 v/cm, 1 μsec x 1

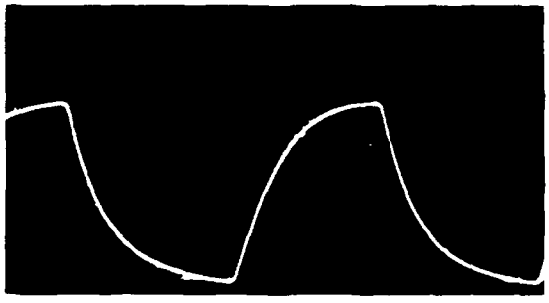

4. 500 KHz
   20 v/cm, .1 μsec x5

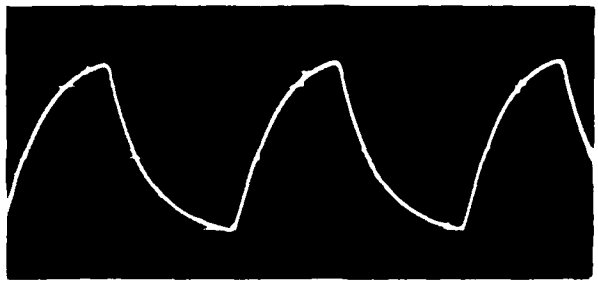

5. 650 KHz
   20 v/cm, .1 μsec x 5

Figure 6
Square Wave Test
1.5KC51 (V_B 52.65) Mounted in LPM 9455A

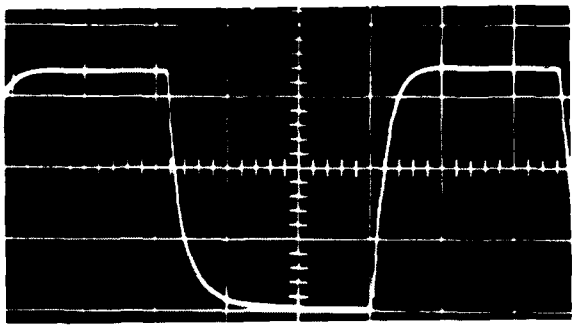

1. 100 KHz
   10 v/cm, 1 μsec x 2

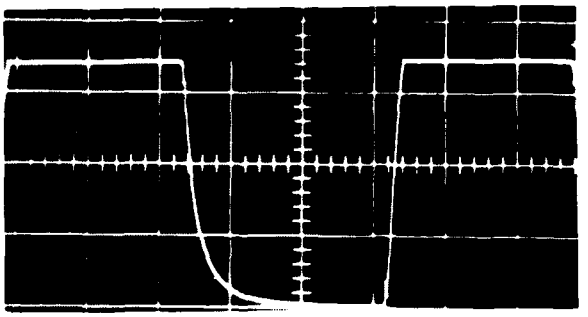

2. 100 KHz (Showing Clipping)
   10 v/cm, 1 μsec x 2

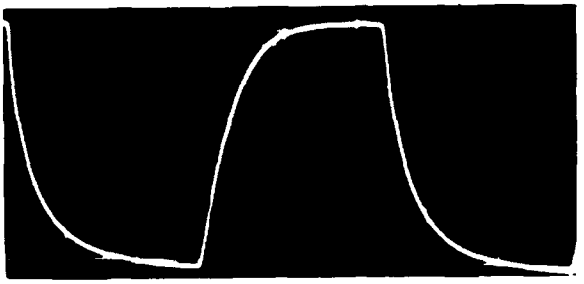

3. 200 KHz
   10 v/cm, 1 μsec x 1

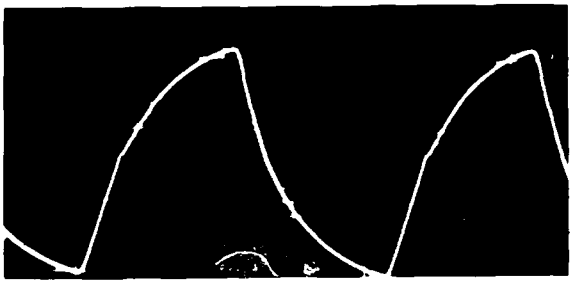

4. 500 KHz
   10 v/cm, .1 μsec x 5

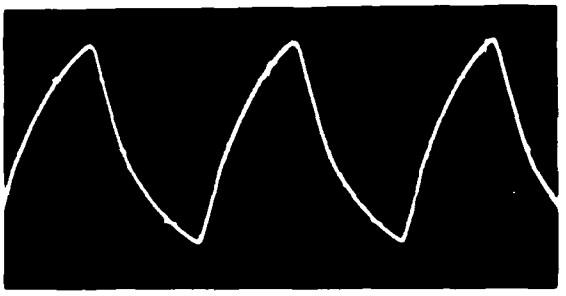

5. 750 KHz
   10 v/cm, .1 μsec x 1

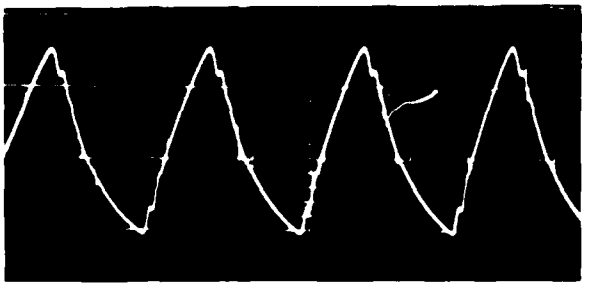

6. 1000 KHz
   10 v/cm, .1 μsec x 5

Figure 7
Square Wave Test
GZ 92111A (V_B 35.1v) Mounted in LPM 9455A

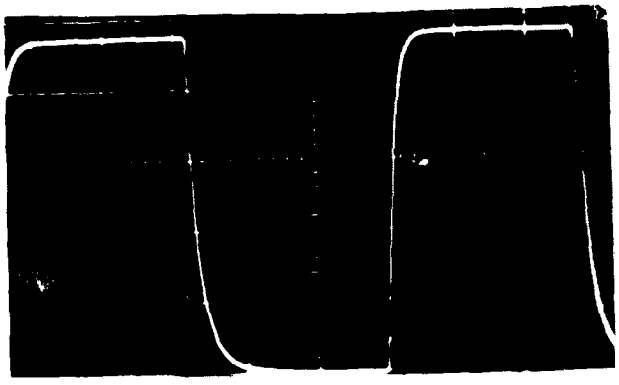

1. 100 KHz
   10 v/cm, 1 μsec x 2

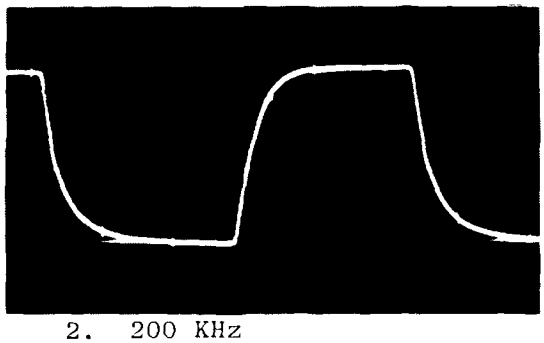

2. 200 KHz
   20 v/cm, 1 μsec x 1

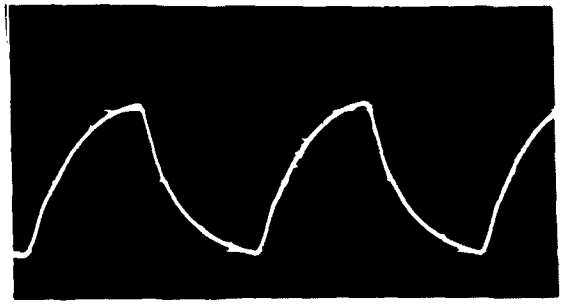

3. 650 KHz
   20 v/cm, .1 μsec x 5

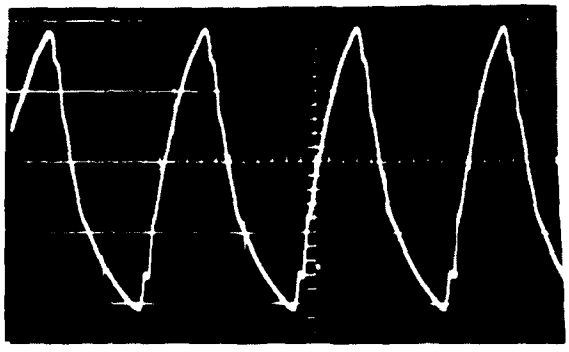

4. 1000 KHz
   10 v/cm, .1 μsec x 5

Figure 8
GZ 92111B (V_B 50.4) Mounted in LPM 9455A

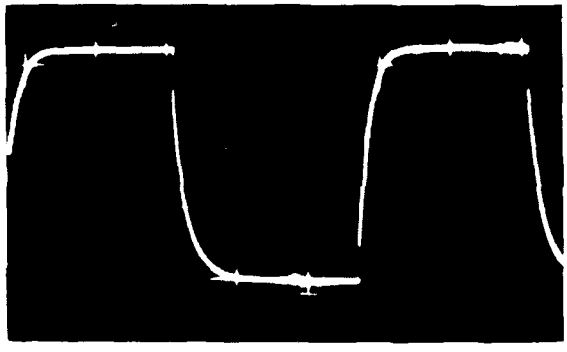

1. 10 KHz
   2 v/cm, 10 µsec x 2

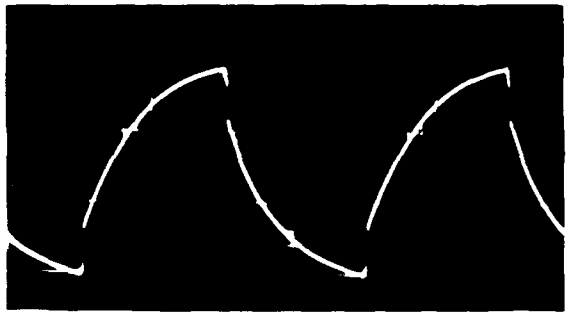

2. 50 KHz
   2 v/cm, 1 µsec x 5

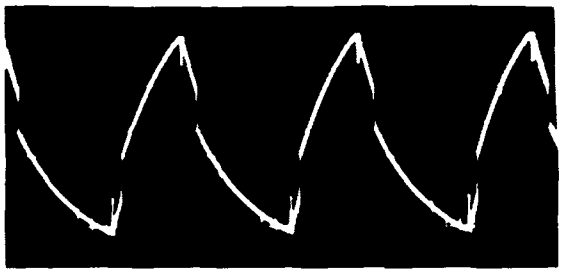

3. 200 KHz
   2 v/cm, 1 µsec x 2

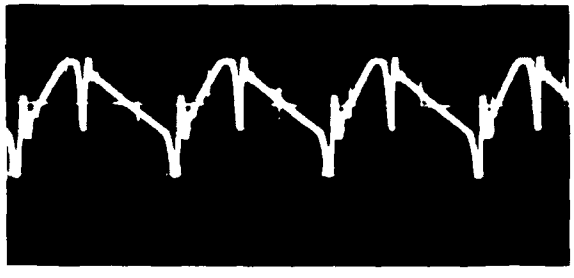

4. 1000 KHz
   2 v/cm, .1 µsec x 5

Figure 9
GZ 60316B (V_B 6.8v) Mounted in LPM 9455A

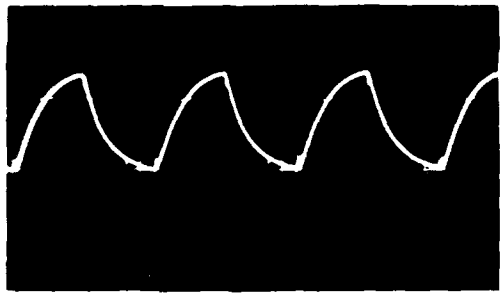

1. 1.5KC7.5 100 KHz
   5 v/cm, 1 μsec x 5

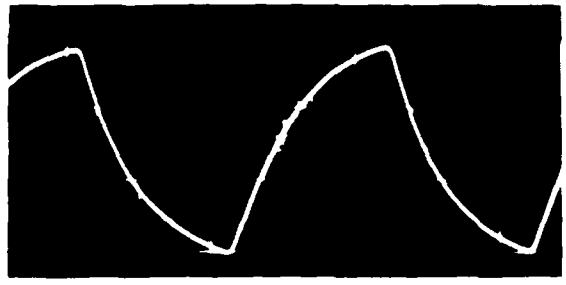

2. 1.5KC36 500 KHz
   10 v/cm, .1 μsec x 5

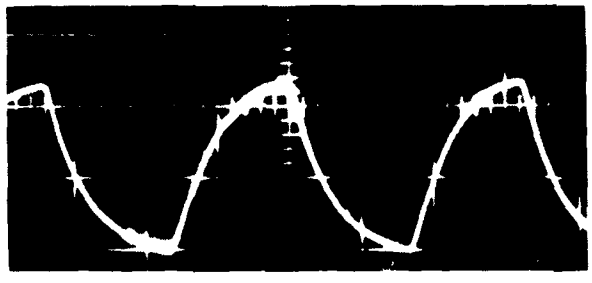

3. 1.5KC51 650 KHz
   20 v/cm, .1 μsec x 5

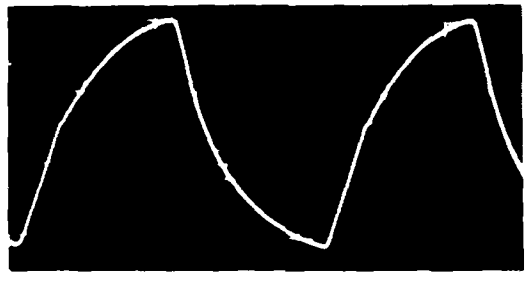

4. GZ92111A 500 KHz
   10 v/cm, .1 μsec x 5

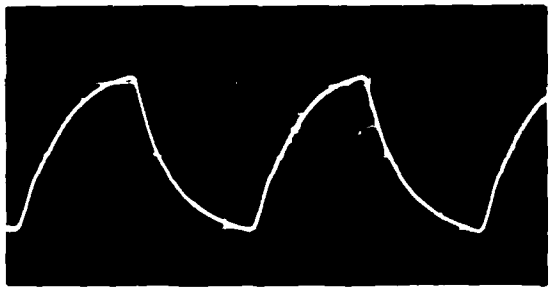

5. GZ92111B 650 KHz
   20 v/cm, .1 μsec x 5

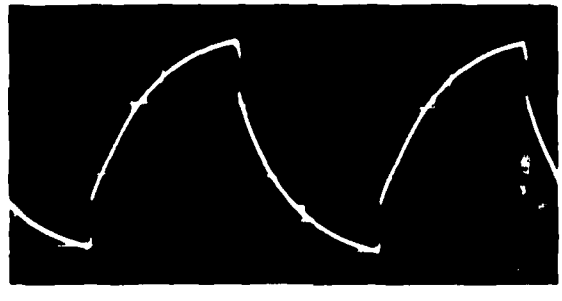

6. GZ60316B 50 KHz
   2 v/cm, 1 μsec x 5

Figure 10

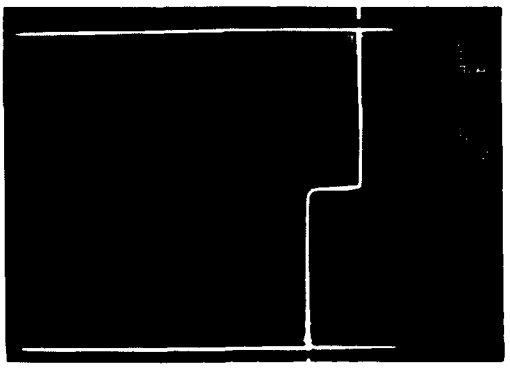

A

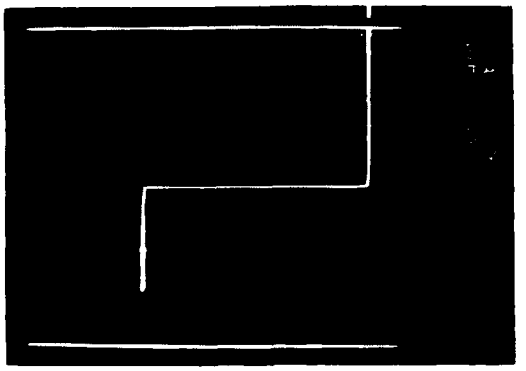

B

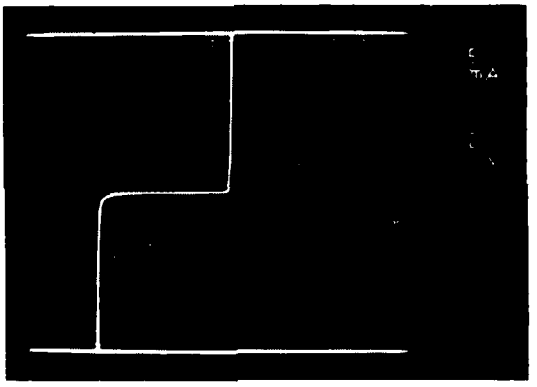

C

Figure 11

Zener Curves
A and C GZ60316B
B GZ92111A

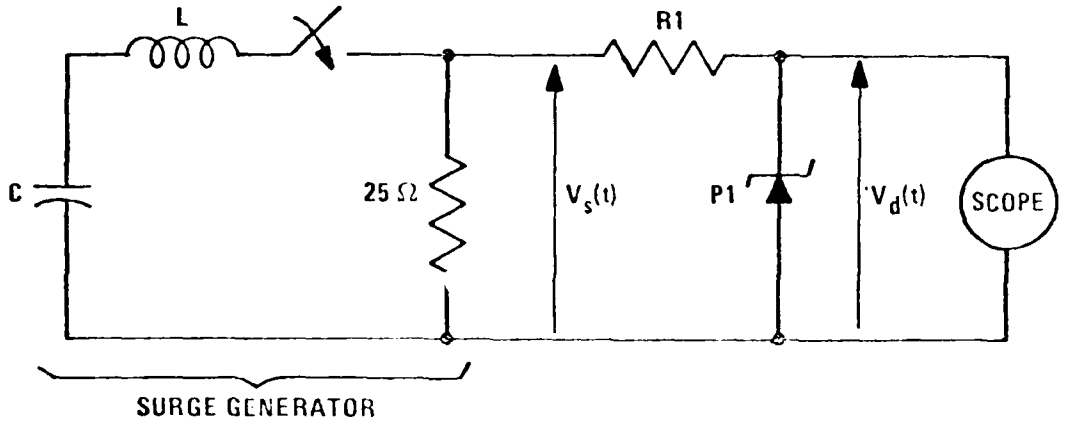

Figure 12

C = 67.5 Mfd, 1200 Volt
V_S = 1000 Volts
V_D = Dependent on device
R_1 = 120

Figure 13 shows a typical response curve, effectively a 10 x 1000 waveform.

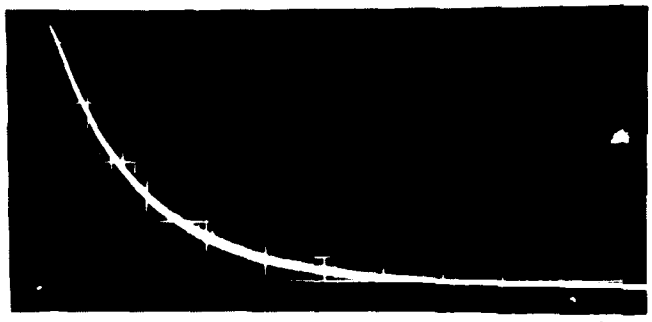

200 Volts/cm

1 millisecond/cm

Figure 13

The output of the surge generator was connected to the barrier strip through an 18" length of RG58 coaxial cable. The oscilloscope, barrier strip and surge generator shared a common ground. Tests were conducted using a representative group of leadless TransZorbs with the conical coil spring internal contact furnished with the LPMs.

Also tested were two Joslyn leadless gas tube supressors and two transient suppressors with leads. All results are shown graphically in the following series of photographs. It can be seen that all units clamped essentially within tolerance limits.

The discharge curves for the unipolar and bipolar devices are essentially the same. Apparent differences in peak values can be attributed to jitter in the vertical amplifier of the oscilloscope.

Two devices with leads were connected using maximum lead length, totaling 2 inches. Results are pictured in Figure 16. Note the accentuated peak occurring

in the first millisecond of clamping.

As shown in Figure 17 gas tube devices essentially show a short circuit during conduction. When conduction ceases, voltage rises to the point determined by the discharge characteristic. For low voltage circuit protection they are normally used in combination with a silicon avalanche diode or devices with similar low voltage protection capability. The FA9455 LPMs will readily accept the Joslyn two electrode miniature gas tube surge protectors and those of other manufacturers with similar dimensions.

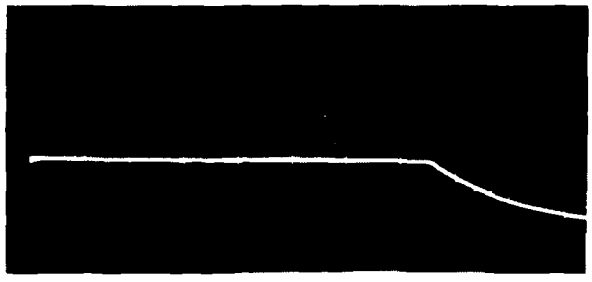

A. 1.5 KC 7.5 5 V/cm

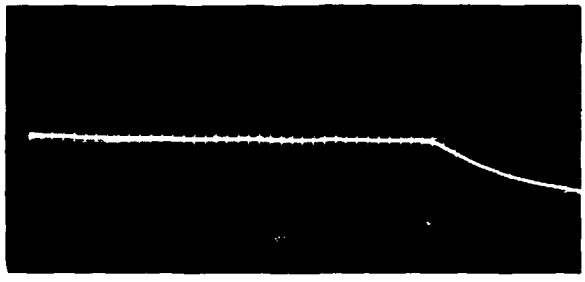

B. 1.5 KC 7.5C 5 V/cm

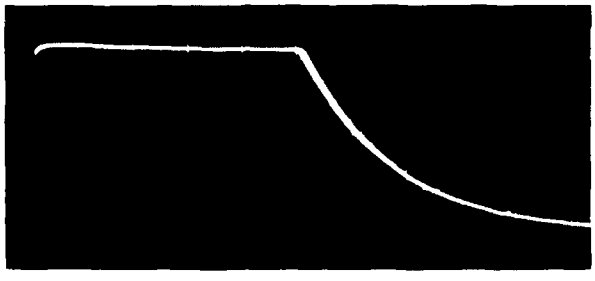

C. 1.5 KC 36 10 V/cm

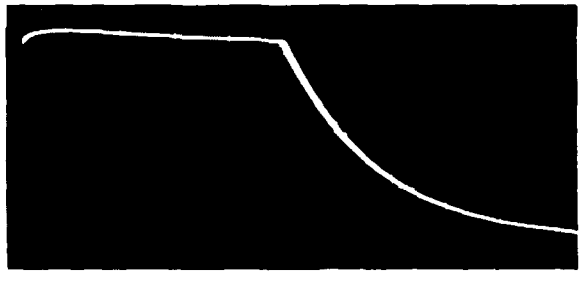

D. 1.5 KC 36C 10 V/cm

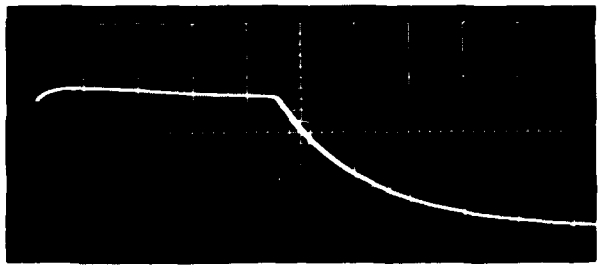

E. 1.5 KC 51 20 V/cm

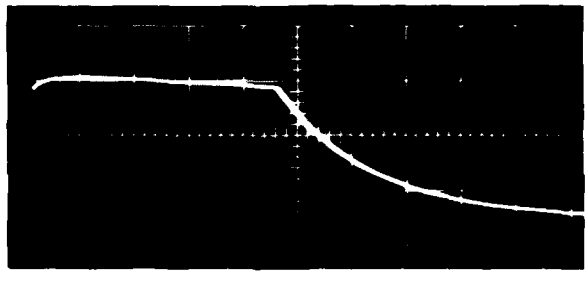

F. 1.5 KC 51C 20 V/cm

Figure 14

Stock TransZorbs (C= Bipolar)
Mounted in FA9455A
V_S + 1000 Volts R_1 = 120

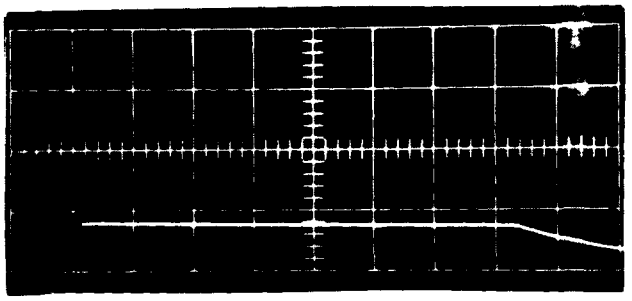

A. GZ60316B 10 V/cm

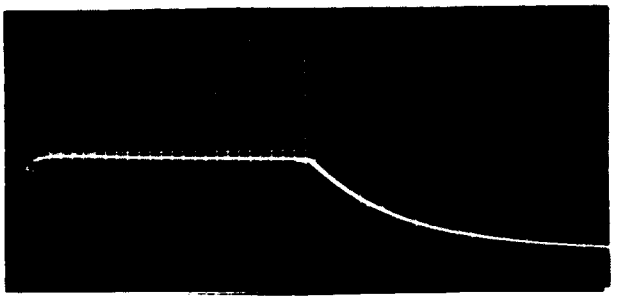

B. GZ92111A 20 V/cm

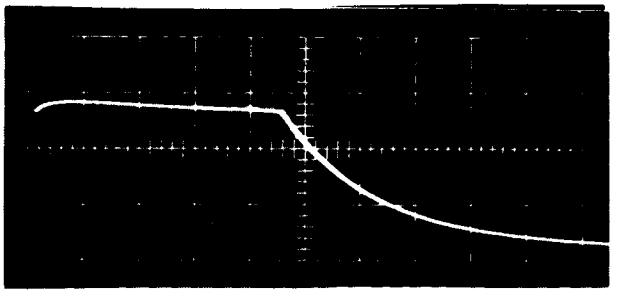

C. GZ92111B 20 V/cm

Figure 15

Low Capacity Unipolar Units
Mounted in FA9455A
V_S = 1000 Volts R_1 =120Ω

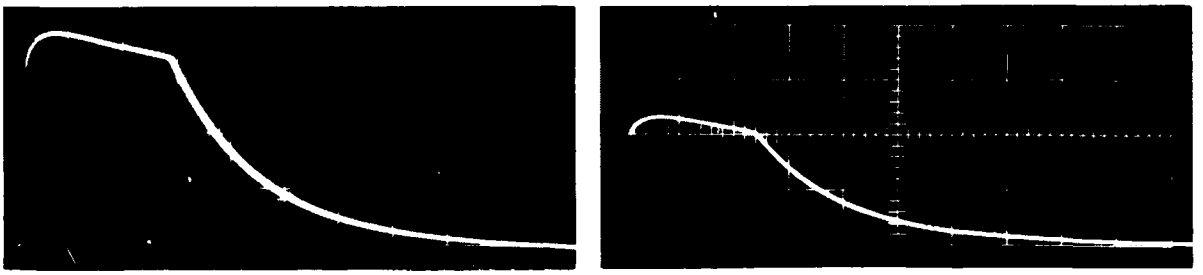

A. IN5662A 50 V/cm B. 1.5 KE200CA 100 V/cm

Figure 16

Avalanche Diodes With Leads
V_S= 1000 Volts R_l = 120

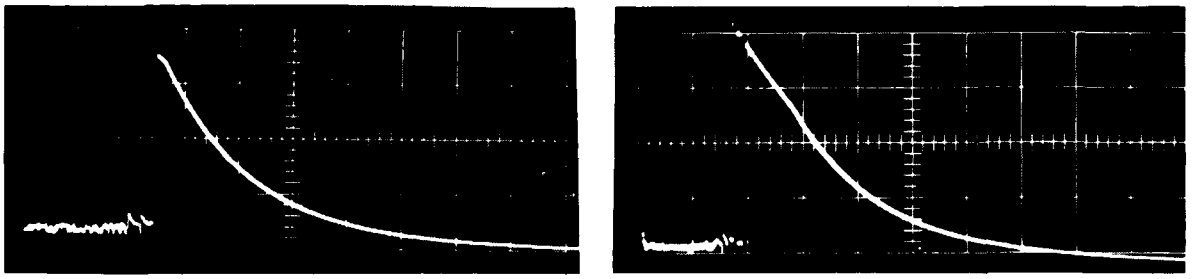

A. Joslyn 2022-12* 50 V/cm B. Joslyn 2021-12* 50 V/cm

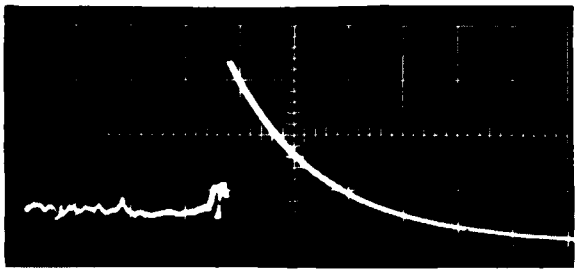

C. NE-51 20 Vcm

Figure 17

Gas Tube Devices in FA9455A
V_s= 1000 Volts R_l = 120

* Leads Removed

B.Coaxial Module, FA 9479

1.Insertion Loss Tests

The coaxial module alone and in combination was tested for insertion loss at frequencies ranging from 10 MHz to 1 GHz. The devices used in conjunction with the module were pairs; GZ60316B, V_b 6.8v nominal; GZ92111A, V_b 36v nominal; and GZ92111B, V_b 51v nominal. Tests were performed on a Hewlett Packard 8507B Automatic Network Analyzer through the courtesy of the Harris Corporation. Results are tabulated in Tables 1, 2, 3 and 4. Table 5 is the calibration check. Results are plotted graphically in Figures 18, 19, 20 and 21. The GZ92111A's and GZ92111B's both exhibit smooth rising curves with the higher voltage device exhibiting less loss because of its lower junction capacitance. The much lower voltage GZ60316B, figure 21, has a sharply pronounced peak loss at approximately 370 MHz indicative of leakage and a possible resonance in the low capacity diode circuit incorporated in the device.

Depending on application, either insertion loss or VSWR may be used as the criteria for maximum usable frequency. An insertion loss of 3db or a VSWR of 1.5 to 1 are commonly used (but not equivalent) limits, 3db being the half power point while a VSWR of 1.5 to 1 yields 96% power transmission. Referring to the printouts from the Network Analyzer note that the insertion (transmission) loss is provided directly. VSWR is derived from the return loss using nomographs for VSWR.* It should be noted that the second column of the printout which identifies the transmission loss does not include the power dissapated in the device. It is not the complement of the return loss and therefore cannot be used to enter the nomograph to obtain the VSWR. (ie It is not the "Transmission Loss" as defined in the nomograph) The transmission loss in the column indicates the percentage of power which gets past the LPM to the load. The method of measuring the return loss using reflected power is consistent with the requirement of the nomograph and is used to find the VSWR. For a further discussion, see Appendix A.

An insertion loss curve for a module without diodes is shown in figure 18. Note that the module alone at one GHz shows less than 1db insertion loss. Curves for the coaxial modules with low capacity diodes are shown in figures 19, 20 and 21. Table 6 shows the results for the module with pairs of low capacity diodes in bipolar configuration.

TABLE 6

Protection	96% Transmission or 1.5:1 VSWR	50% Transmission Point or 3db Insertion Loss
2 GZ60316B	30 MHz	110 MHz
2 GZ92111A	170 MHz	690 MHz
2 GZ92111B	270 MHz	850 MHz

*Electronics Engineers' Handbook, Donald G. Fink, Editor in Chief. First Edition, pages 9-5 and 9-6.

FREQUENCY MHZ	RETURN LOSS INPUT (S11) DB	ANG	TRANS. LOSS FORWARD (S21) DB	ANG	TRANS. LOSS REVERSE (S12) DB	ANG	RETURN LOSS OUTPUT (S22) DB	ANG
			TYPE "N" MODIFIED TEE					
10.000	42.3	-110.7	0.00	-0.7	0.00	-0.8	43.4	-81.8
35.000	35.6	-77.0	0.00	-2.6	0.00	-2.6	35.6	-72.9
60.000	31.9	-82.5	0.00	-4.4	0.00	-4.5	33.4	-109.3
85.000	28.8	-86.1	0.01	-6.3	0.01	-6.3	32.9	-148.0
110.000	26.3	-98.7	0.01	-8.1	0.02	-8.1	32.6	165.3
135.000	25.5	-114.6	0.01	-9.8	0.01	-9.8	31.4	125.6
160.000	27.5	-119.3	0.01	-11.7	0.01	-11.7	28.1	73.8
185.000	28.1	-91.3	0.01	-13.6	0.02	-13.7	26.2	23.7
210.000	23.4	-92.9	0.02	-15.5	0.03	-15.3	24.6	-26.8
235.000	21.7	-105.3	0.04	-17.3	0.04	-17.4	22.9	-66.9
260.000	21.7	-110.3	0.04	-19.1	0.04	-19.2	21.2	-97.3
285.000	21.2	-105.9	0.05	-21.0	0.05	-21.0	19.8	-123.1
310.000	20.0	-104.2	0.06	-22.9	0.06	-22.9	19.0	-150.1
335.000	19.0	-101.9	0.08	-24.9	0.08	-24.9	18.3	-176.0
360.000	17.7	-100.4	0.09	-26.2	0.09	-26.1	18.4	154.8
385.000	16.6	-103.0	0.10	-28.7	0.10	-28.1	18.3	119.1
410.000	15.7	-105.1	0.11	-30.9	0.13	-29.9	18.4	76.3
435.000	14.4	-110.1	0.14	-32.9	0.14	-32.8	18.6	31.4
460.000	13.6	-119.8	0.18	-34.9	0.18	-34.8	19.1	-13.5
485.000	14.2	-128.5	0.17	-36.7	0.18	-36.5	18.5	-46.2
510.000	15.2	-128.9	0.18	-38.6	0.17	-38.5	17.0	-76.0
535.000	14.9	-124.1	0.21	-40.7	0.21	-40.7	14.8	-106.8
560.000	14.0	-124.1	0.26	-42.5	0.26	-42.6	13.1	-138.6
585.000	13.2	-123.0	0.27	-44.2	0.28	-44.5	12.2	-168.0
610.000	11.8	-124.8	0.30	-46.1	0.31	-46.3	11.6	165.5
635.000	10.9	-133.6	0.34	-47.5	0.33	-47.8	10.8	138.6
660.000	11.3	-141.8	0.31	-49.2	0.32	-49.6	10.7	106.7
685.000	12.1	-141.8	0.33	-51.5	0.34	-51.6	11.0	70.8
710.000	11.9	-139.4	0.39	-53.7	0.41	-53.7	11.8	33.8
735.000	11.7	-142.0	0.42	-55.6	0.42	-55.4	12.4	-2.5
760.000	12.1	-141.7	0.45	-57.7	0.45	-57.5	12.1	-39.2
785.000	11.8	-135.2	0.48	-59.8	0.49	-59.6	11.4	-77.1
810.000	10.6	-135.7	0.54	-61.7	0.55	-61.7	10.4	-116.2
835.000	10.0	-139.9	0.59	-63.7	0.61	-63.6	9.4	-152.5
860.000	9.4	-142.6	0.62	-65.4	0.64	-65.4	8.6	175.1
885.000	8.9	-147.1	0.65	-67.5	0.66	-67.4	7.8	144.2
910.000	8.7	-151.3	0.69	-69.6	0.69	-69.6	7.4	113.6
935.000	8.9	-153.2	0.74	-71.7	0.74	-71.6	7.4	83.9
960.000	8.6	-153.8	0.82	-73.9	0.83	-73.9	7.7	53.9
985.000	8.6	-155.6	0.91	-75.3	0.93	-76.0	8.0	22.7

Table 1

FREQUENCY	RETURN LOSS INPUT (S11)		TRANS. LOSS FORWARD (S21)		TRANS. LOSS REVERSE (S12)		RETURN LOSS OUTPUT (S22)	
MHZ	DB	ANG	DB	ANG	DB	ANG	DB	ANG
			GZ 92111A					
10.000	26.2	-119.6	0.19	-2.7	0.20	-2.8	25.5	-119.1
30.000	20.4	-128.3	0.50	-5.9	0.50	-6.0	20.1	-129.5
50.000	17.8	-134.9	0.76	-8.0	0.76	-8.0	17.9	-135.6
70.000	16.4	-140.7	0.95	-9.7	0.96	-9.7	16.6	-139.5
90.000	15.9	-144.9	1.08	-11.0	1.09	-10.9	15.7	-142.5
110.000	15.4	-146.5	1.17	-12.5	1.17	-12.4	15.1	-145.4
130.000	14.9	-147.3	1.25	-13.9	1.24	-13.7	14.8	-147.9
150.000	14.3	-148.9	1.31	-15.1	1.30	-15.1	14.6	-149.2
170.000	14.1	-150.3	1.34	-16.7	1.34	-16.7	14.4	-150.0
190.000	13.9	-150.3	1.40	-18.2	1.39	-18.2	14.0	-149.8
210.000	13.5	-150.1	1.45	-19.8	1.45	-19.7	13.5	-149.9
230.000	13.0	-151.2	1.49	-21.2	1.49	-21.1	13.1	-150.1
250.000	12.7	-152.2	1.52	-22.6	1.53	-22.6	12.7	-151.0
270.000	12.4	-152.2	1.57	-24.2	1.58	-24.2	12.2	-151.5
290.000	12.1	-152.9	1.63	-25.8	1.62	-25.8	11.9	-152.2
310.000	11.8	-153.2	1.68	-27.3	1.67	-27.3	11.5	-152.5
330.000	11.4	-153.9	1.72	-28.8	1.72	-28.8	11.2	-153.2
350.000	11.0	-154.5	1.77	-30.5	1.77	-30.5	11.0	-153.7
370.000	10.7	-155.0	1.83	-32.0	1.83	-31.9	10.6	-154.3
390.000	10.4	-155.8	1.89	-33.6	1.89	-33.6	10.4	-154.8
410.000	10.0	-156.8	1.94	-35.2	1.94	-35.1	10.1	-155.7
430.000	9.8	-157.9	1.99	-36.8	1.99	-36.8	9.9	-156.6
450.000	9.5	-159.5	2.07	-38.4	2.05	-38.5	9.6	-157.9
470.000	9.3	-160.1	2.12	-40.0	2.11	-40.0	9.5	-158.9
490.000	9.0	-160.5	2.19	-41.6	2.18	-41.6	9.2	-160.0
510.000	8.7	-161.5	2.25	-43.2	2.25	-43.1	9.0	-160.9
530.000	8.4	-163.0	2.32	-44.1	2.33	-44.7	8.7	-161.8
550.000	8.2	-164.3	2.39	-45.7	2.40	-46.1	8.4	-163.0
570.000	7.9	-165.8	2.50	-47.2	2.49	-47.7	8.2	-164.7
590.000	7.6	-167.7	2.59	-48.7	2.57	-48.7	7.9	-166.2
610.000	7.5	-169.9	2.67	-50.2	2.65	-50.2	7.7	-167.6
630.000	7.4	-170.5	2.76	-51.6	2.76	-51.7	7.5	-168.8
650.000	7.3	-171.1	2.85	-52.9	2.84	-53.1	7.2	-169.7
670.000	7.0	-172.2	2.94	-54.5	2.94	-54.7	7.1	-170.8
690.000	6.8	-173.6	3.00	-56.8	3.01	-56.4	6.8	-172.6
710.000	6.6	-175.1	3.11	-58.6	3.12	-58.0	6.7	-173.6
730.000	6.4	-176.2	3.22	-60.2	3.21	-59.5	6.6	-175.0
750.000	6.2	-178.0	3.33	-62.0	3.32	-61.3	6.4	-176.3
770.000	6.0	179.9	3.45	-63.6	3.45	-63.4	6.3	-177.5
790.000	5.9	178.4	3.57	-65.4	3.57	-65.2	6.1	-178.8
810.000	5.8	177.2	3.71	-67.0	3.71	-66.6	5.8	179.7
830.000	5.6	175.7	3.85	-68.4	3.84	-68.1	5.6	178.2
850.000	5.5	174.1	3.98	-69.9	3.99	-69.4	5.5	176.3
870.000	5.3	172.8	4.12	-71.5	4.12	-71.0	5.3	174.7
890.000	5.2	171.4	4.25	-72.7	4.25	-72.3	5.1	173.0
910.000	4.9	170.1	4.38	-74.1	4.38	-73.7	5.0	171.5
930.000	4.7	167.9	4.55	-75.6	4.55	-75.3	4.8	169.8
950.000	4.6	166.0	4.71	-76.9	4.72	-76.8	4.6	168.2
970.000	4.5	164.1	4.89	-78.4	4.91	-78.2	4.5	166.5
990.000	4.3	162.3	5.10	-79.7	5.11	-79.6	4.4	165.0

Table 2

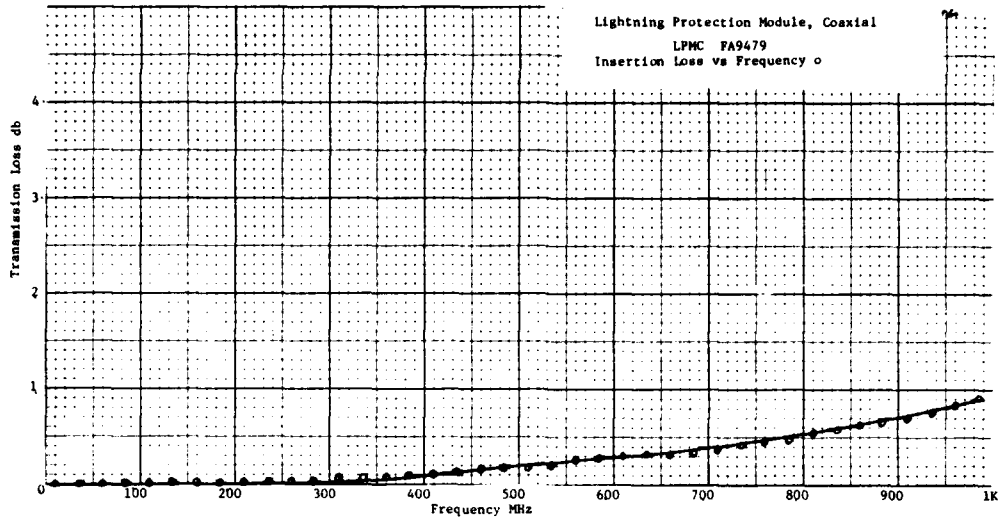

Figure 18

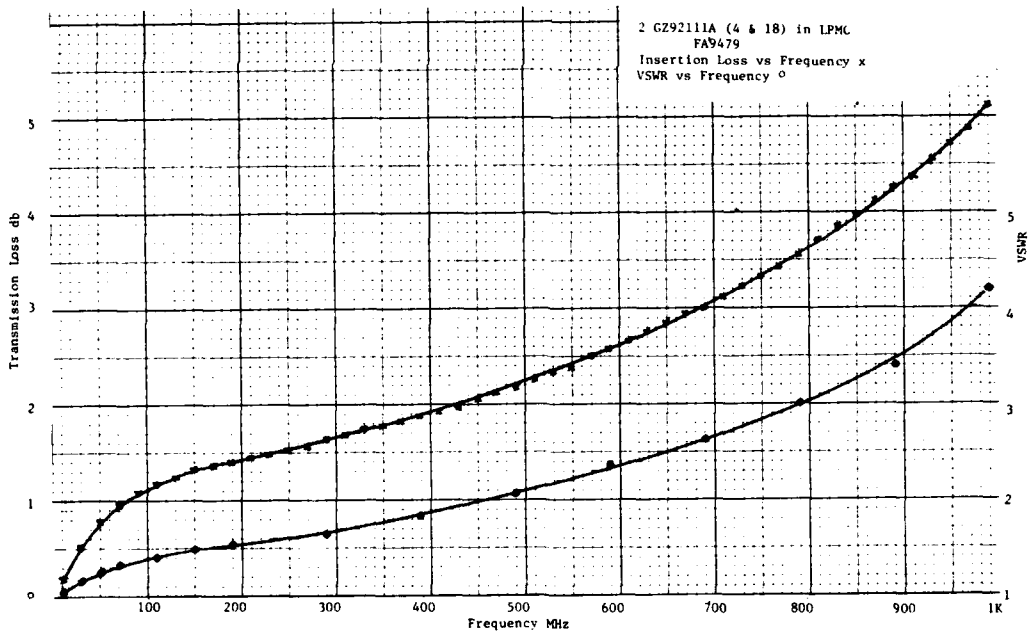

Figure 19

FREQUENCY MHZ	RETURN LOSS INPUT (S11) DB	ANG	TRANS. LOSS FORWARD (S21) DB	ANG	TRANS. LOSS REVERSE (S12) DB	ANG	RETURN LOSS OUTPUT (S22) DB	ANG
			GZ 92111B					
10.000	29.4	-115.3	0.11	-2.1	0.12	-2.1	28.4	-115.0
30.000	23.2	-123.5	0.33	-4.9	0.33	-5.0	22.9	-125.2
50.000	20.4	-130.0	0.51	-6.6	0.51	-6.7	20.5	-130.7
70.000	19.0	-135.4	0.63	-8.2	0.64	-8.3	19.2	-133.7
90.000	18.4	-139.2	0.72	-9.6	0.72	-9.6	18.3	-135.7
110.000	17.9	-139.5	0.77	-11.3	0.77	-11.2	17.6	-138.3
130.000	17.2	-139.4	0.82	-12.8	0.81	-12.7	17.1	-140.5
150.000	16.6	-140.7	0.85	-14.1	0.85	-14.1	16.9	-141.3
170.000	16.3	-141.7	0.87	-15.6	0.87	-15.6	16.6	-141.2
190.000	15.9	-141.0	0.91	-17.2	0.90	-17.2	16.1	-140.4
210.000	15.4	-140.4	0.94	-18.8	0.94	-18.8	15.5	-140.0
230.000	14.8	-141.6	0.98	-20.3	0.98	-20.4	14.9	-140.2
250.000	14.5	-142.4	1.00	-21.9	1.01	-21.9	14.3	-141.1
270.000	14.1	-142.3	1.04	-23.5	1.05	-23.5	13.8	-141.8
290.000	13.6	-142.7	1.09	-25.2	1.09	-25.2	13.3	-142.5
310.000	13.1	-143.2	1.12	-26.8	1.11	-26.8	12.8	-143.0
330.000	12.6	-144.1	1.16	-28.3	1.16	-28.4	12.4	-143.7
350.000	12.2	-144.7	1.21	-30.0	1.20	-30.0	12.1	-144.1
370.000	11.9	-145.4	1.25	-31.6	1.25	-31.6	11.7	-144.8
390.000	11.5	-146.3	1.29	-33.4	1.30	-33.4	11.4	-145.4
410.000	11.1	-147.7	1.34	-34.9	1.35	-34.9	11.1	-146.3
430.000	10.7	-149.0	1.38	-36.6	1.38	-36.6	10.8	-147.3
450.000	10.4	-150.7	1.44	-38.2	1.43	-38.2	10.6	-148.6
470.000	10.2	-151.3	1.48	-39.9	1.47	-39.9	10.3	-149.7
490.000	9.8	-151.7	1.54	-41.4	1.54	-41.4	10.1	-150.8
510.000	9.4	-152.8	1.59	-43.0	1.58	-43.0	9.8	-151.7
530.000	9.1	-154.5	1.64	-44.1	1.65	-44.8	9.5	-152.7
550.000	8.8	-156.0	1.71	-45.8	1.73	-46.2	9.1	-154.1
570.000	8.6	-157.6	1.79	-47.3	1.79	-47.8	8.8	-156.0
590.000	8.3	-159.6	1.87	-48.8	1.86	-48.8	8.5	-157.7
610.000	8.2	-162.0	1.93	-50.5	1.92	-50.4	8.3	-159.2
630.000	8.1	-162.4	2.01	-51.9	2.02	-52.0	8.1	-160.4
650.000	7.9	-162.7	2.09	-53.3	2.08	-53.5	7.9	-161.4
670.000	7.5	-163.8	2.15	-54.9	2.15	-55.1	7.6	-162.3
690.000	7.3	-165.4	2.20	-57.4	2.21	-57.0	7.4	-164.2
710.000	7.2	-166.7	2.29	-59.1	2.30	-58.6	7.1	-165.7
730.000	6.9	-167.9	2.38	-61.0	2.37	-60.3	6.9	-166.6
750.000	6.6	-170.1	2.47	-62.7	2.45	-62.4	6.9	-168.0
770.000	6.5	-172.2	2.55	-64.7	2.55	-63.9	6.7	-168.9
790.000	6.4	-173.6	2.65	-66.6	2.66	-66.3	6.5	-170.2
810.000	6.3	-174.7	2.77	-68.3	2.77	-67.9	6.3	-171.7
830.000	6.1	-176.0	2.88	-69.9	2.87	-69.6	6.0	-173.5
850.000	5.9	-177.6	2.99	-71.4	2.99	-71.0	5.8	-175.2
870.000	5.7	-178.9	3.09	-73.3	3.10	-72.8	5.7	-176.9
890.000	5.5	179.9	3.21	-74.7	3.21	-74.2	5.5	-178.5
910.000	5.3	178.4	3.32	-76.3	3.32	-75.9	5.3	179.9
930.000	5.1	176.2	3.45	-78.0	3.44	-77.7	5.1	178.2
950.000	4.9	174.3	3.58	-79.6	3.58	-79.5	4.9	176.5
970.000	4.8	172.5	3.71	-81.4	3.74	-81.3	4.8	175.0
990.000	4.6	170.8	3.89	-83.2	3.91	-83.0	4.6	173.5

Table 3

FREQUENCY MHZ	RETURN LOSS INPUT (S11) DB	ANG	TRANS. LOSS FORWARD (S21) DB	ANG	TRANS. LOSS REVERSE (S12) DB	ANG	RETURN LOSS OUTPUT (S22) DB	ANG
			GZ 60316B					
10.000	20.7	-108.8	0.22	-5.2	0.22	-5.3	20.4	-109.5
30.000	13.2	-115.5	0.64	-13.3	0.63	-13.4	13.2	-116.7
50.000	9.7	-122.1	1.12	-20.5	1.11	-20.5	9.7	-122.9
70.000	7.6	-128.9	1.68	-26.8	1.68	-27.1	7.5	-129.3
90.000	6.2	-135.0	2.28	-32.7	2.31	-32.7	6.0	-134.9
110.000	5.1	-140.6	2.98	-38.3	2.99	-38.1	5.0	-140.9
130.000	4.2	-146.2	3.75	-43.2	3.78	-42.9	4.2	-146.2
150.000	3.6	-151.2	4.48	-47.0	4.45	-47.0	3.6	-150.7
170.000	3.0	-156.1	5.34	-51.1	5.33	-51.2	3.1	-155.6
190.000	2.6	-160.6	6.33	-54.5	6.32	-54.5	2.6	-160.2
210.000	2.2	-165.2	7.40	-57.2	7.40	-57.2	2.3	-164.7
230.000	1.9	-169.3	8.54	-59.0	8.55	-58.9	2.0	-169.0
250.000	1.7	-173.5	9.79	-60.0	9.81	-59.9	1.7	-173.1
270.000	1.5	-177.5	11.18	-60.1	11.18	-59.9	1.5	-177.0
290.000	1.4	178.8	12.61	-58.2	12.71	-58.2	1.4	179.2
310.000	1.3	175.6	14.21	-54.1	14.26	-54.3	1.3	175.6
330.000	1.2	171.4	15.88	-46.5	15.95	-46.6	1.2	172.1
350.000	1.1	168.0	17.38	-34.6	17.35	-34.7	1.1	168.7
370.000	1.0	164.5	18.08	-18.5	18.15	-18.5	1.1	165.3
390.000	1.0	161.1	17.76	-2.0	17.82	-2.0	1.0	162.0
410.000	1.0	157.9	16.64	10.9	16.69	10.9	1.0	158.7
430.000	1.0	154.8	15.29	19.2	15.23	19.2	1.0	155.5
450.000	1.1	151.6	13.92	24.0	13.86	24.0	1.0	152.5
470.000	1.1	149.1	12.63	25.9	12.56	26.5	1.1	149.5
490.000	1.2	146.3	11.47	27.3	11.51	27.1	1.1	146.7
510.000	1.2	143.3	10.48	27.3	10.52	27.3	1.2	143.7
530.000	1.3	140.4	9.52	27.3	9.58	26.7	1.2	140.9
550.000	1.4	137.6	8.75	26.2	8.73	26.0	1.3	138.3
570.000	1.4	134.6	8.05	25.0	8.05	24.6	1.4	135.5
590.000	1.6	132.0	7.42	23.5	7.35	23.4	1.5	133.5
610.000	1.7	129.6	6.78	21.6	6.83	21.7	1.6	130.8
630.000	1.8	127.4	6.34	20.0	6.29	19.9	1.8	128.3
650.000	1.9	124.9	5.83	18.3	5.86	18.0	1.9	125.8
670.000	2.0	121.7	5.46	16.1	5.47	15.9	2.0	123.2
690.000	2.2	118.9	5.06	13.6	5.07	13.6	2.2	120.3
710.000	2.3	116.3	4.72	11.3	4.71	11.3	2.3	117.9
730.000	2.5	113.8	4.42	8.9	4.39	8.9	2.5	115.8
750.000	2.8	111.7	4.10	6.6	4.11	6.4	2.6	113.5
770.000	3.0	110.4	3.85	4.2	3.87	4.2	2.8	111.3
790.000	3.1	108.8	3.59	1.9	3.61	2.0	3.0	109.2
810.000	3.3	106.8	3.35	-0.4	3.35	-0.3	3.2	107.0
830.000	3.4	104.7	3.12	-2.5	3.11	-2.5	3.4	104.9
850.000	3.6	102.6	2.90	-4.9	2.90	-4.8	3.6	103.1
870.000	3.7	100.3	2.68	-7.2	2.68	-7.1	3.9	101.4
890.000	3.9	98.0	2.47	-9.2	2.46	-9.2	4.1	99.5
910.000	4.2	95.8	2.28	-11.6	2.28	-11.7	4.3	97.7
930.000	4.4	94.6	2.13	-13.9	2.13	-13.9	4.5	95.8
950.000	4.7	93.2	1.98	-16.2	2.00	-16.3	4.8	93.8
970.000	4.9	91.7	1.85	-18.5	1.88	-18.5	5.0	92.1
990.000	5.1	89.6	1.76	-20.6	1.76	-20.6	5.2	90.1

Table 4

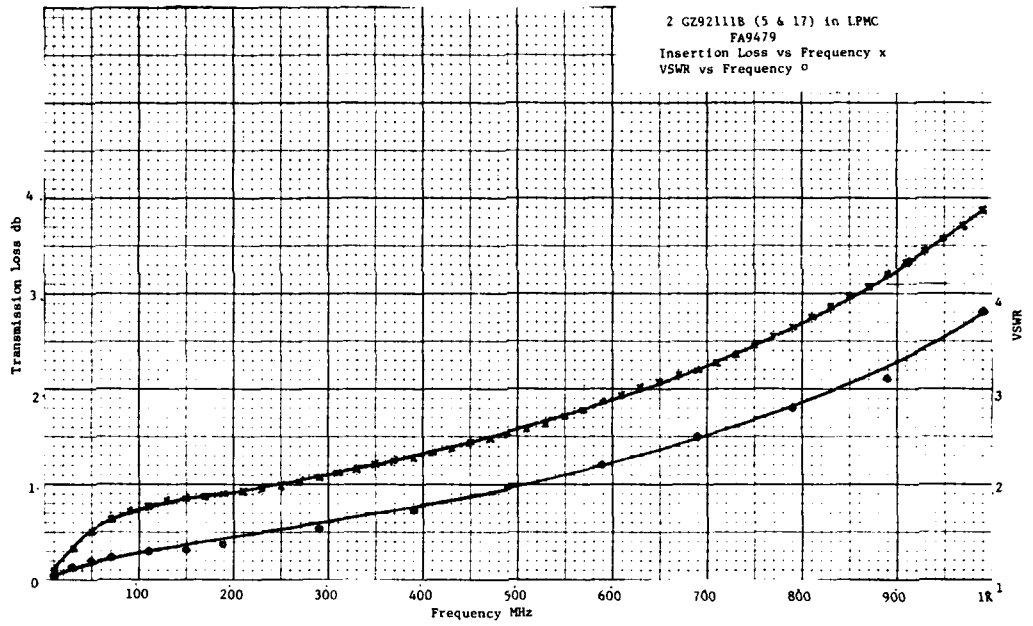

Figure 20

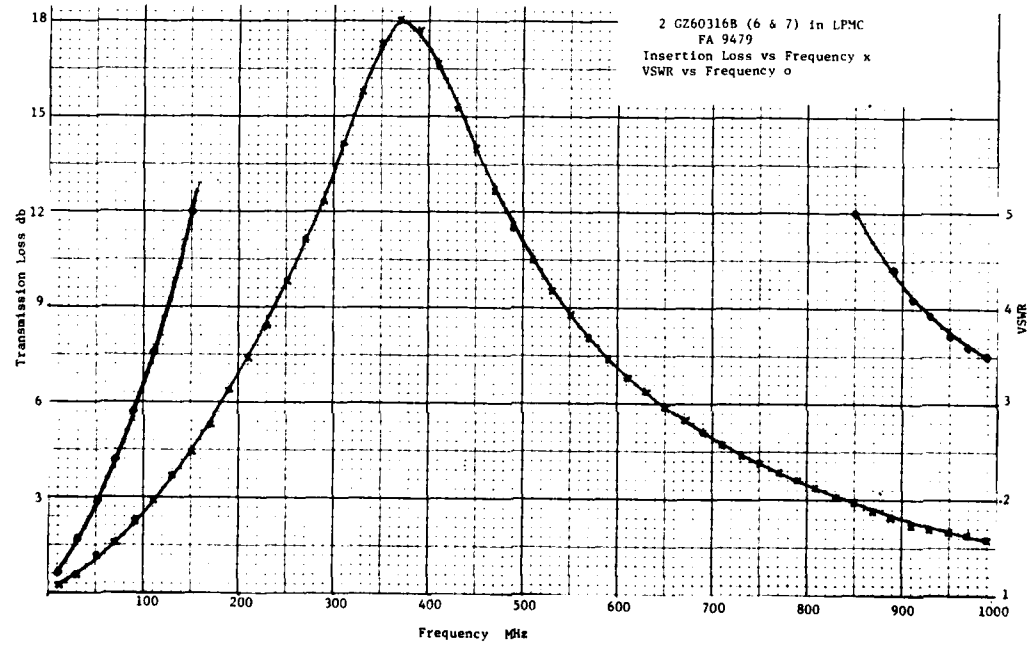

Figure 21

FREQUENCY MHZ	RETURN LOSS INPUT (S11) DB	ANG	TRANS. LOSS FORWARD (S21) DB	ANG	TRANS. LOSS REVERSE (S12) DB	ANG	RETURN LOSS OUTPUT (S22) DB	ANG
	CALIBRATION CHECK (THRU)							
10.000	47.7	-121.1	0.01	-0.0	0.01	-0.0	41.5	-112.3
30.000	49.5	-64.1	0.00	0.1	0.01	-0.0	44.6	-105.4
50.000	42.2	-76.7	0.00	0.1	0.01	-0.0	42.7	-74.9
70.000	40.2	-100.4	0.00	-0.0	0.01	-0.1	38.8	68.9
90.000	44.5	-118.9	0.01	0.1	0.01	0.1	37.5	-75.5
110.000	48.0	-84.7	0.01	-0.0	0.00	0.1	37.9	-88.9
130.000	41.3	-81.2	0.00	-0.0	0.00	0.1	41.1	-104.5
150.000	39.1	-100.0	0.01	0.0	0.01	0.0	44.4	-114.3
170.000	41.9	-117.9	0.01	0.0	0.01	0.0	57.5	-102.1
190.000	45.5	-94.2	0.01	-0.0	0.00	-0.0	48.6	-63.7
210.000	40.2	-90.0	0.01	-0.0	0.01	-0.0	42.5	-69.8
230.000	37.9	-99.1	0.01	-0.0	0.01	0.1	38.1	-83.9
250.000	39.5	-110.4	0.01	0.1	0.02	0.0	35.3	-93.7
270.000	39.5	-92.7	0.01	0.0	0.02	0.0	33.8	-97.7
290.000	37.5	-82.1	0.02	0.0	0.02	0.0	33.1	-98.4
310.000	35.7	-87.0	0.02	-0.0	0.01	0.1	31.3	-95.0
330.000	33.3	-89.3	0.01	-0.0	0.01	-0.0	30.8	-92.4
350.000	32.8	-89.0	0.02	-0.0	0.01	-0.1	30.5	-91.1
370.000	31.5	-88.4	0.03	-0.0	0.02	-0.0	30.1	-89.5
390.000	30.5	-90.3	0.03	-0.1	0.03	-0.0	30.2	-88.9
410.000	29.6	-93.2	0.03	-0.0	0.03	-0.0	30.0	-89.4
430.000	28.9	-96.7	0.03	-0.0	0.02	-0.1	30.0	-89.3
450.000	28.8	-100.9	0.04	-0.1	0.04	-0.1	30.2	-93.8
470.000	29.6	-99.2	0.04	0.0	0.03	0.0	31.2	-97.4
490.000	29.0	-89.4	0.03	-0.1	0.03	-0.1	31.5	-98.6
510.000	27.7	-85.1	0.03	-0.6	0.02	0.1	31.5	-96.9
530.000	26.6	-87.9	0.03	-0.1	0.03	-0.1	31.2	-89.8
550.000	26.3	-88.4	0.04	-0.1	0.04	-0.0	29.3	-87.6
570.000	25.4	-89.0	0.06	-0.1	0.05	-0.7	27.8	-90.3
590.000	24.4	-93.8	0.07	-0.1	0.06	-0.1	27.0	-95.0
610.000	24.6	-103.5	0.08	0.0	0.07	0.0	27.2	-98.1
630.000	26.4	-108.1	0.07	0.2	0.08	0.1	27.2	-97.6
650.000	27.6	-96.4	0.05	0.2	0.05	0.2	27.2	-92.4
670.000	26.3	-85.1	0.05	0.2	0.05	0.0	27.3	-86.7
690.000	25.7	-85.1	0.04	0.1	0.04	-0.0	26.6	-84.4
710.000	25.6	-86.3	0.05	0.0	0.05	-0.1	26.0	-86.0
730.000	25.1	-82.5	0.05	-0.0	0.05	-0.1	26.1	-89.9
750.000	23.7	-85.1	0.05	-0.1	0.05	-0.1	26.3	-92.6
770.000	23.1	-93.4	0.06	-0.1	0.06	-0.0	27.9	91.4
790.000	23.7	-100.7	0.05	-0.1	0.05	-0.1	27.9	-87.2
810.000	24.9	-100.4	0.05	0.0	0.05	-0.1	27.1	-82.9
830.000	24.9	-98.5	0.07	0.0	0.06	-0.1	25.5	-82.2
850.000	25.1	-100.7	0.08	-0.1	0.08	0.0	25.1	-85.1
870.000	26.0	-102.0	0.08	0.0	0.08	-0.1	24.4	-87.6
890.000	26.6	-92.9	0.06	0.0	0.06	0.0	24.2	-87.9
910.000	25.5	-84.5	0.06	-0.0	0.07	-0.0	23.6	-87.4
930.000	24.3	-85.0	0.07	-0.1	0.07	-0.1	23.3	-87.2
950.000	23.5	-88.9	0.08	-0.1	0.09	-0.2	23.0	-87.1
970.000	23.2	-92.3	0.09	-0.2	0.10	-0.3	23.0	-89.3
990.000	23.1	-95.6	0.10	-0.0	0.11	-0.1	23.4	-89.5

Table 5

2. Surge Tests

Surge tests were performed on the coaxial module in conjunction with two GZ60316B low capacity diodes mounted back to back for bipolar action. Surge source was a Keytek Model 424 Surge Generator Monitor with both 8 x 20 and 1.2 x 50 plugin units. Results were recorded on a Tektronix Model 7834 storage Oscilloscope. Tests were performed at the General Semiconductor Industries plant.

Tests 1, 2 and 3 are shown pictorially in figure 22A. All used the 8 x 20 wave shape. The circuit was not terminated. Conical spring in the holder.

a. 500 Volts, 24 amperes, 11 volt clamp

b. 1000 volts, 49 amperes, 12 volt clamp. With slight spike but very little difference.

c. 1000 volts, 98 amperes. Shows bad negative excursion of approximately 10 volts. This latter probably due to heating. The device was operating beyond its limits.

Test 4, Figure 22B is a repeat of the 1000 volt at 98 amperes using a flat non-inductive spring. The clamping voltage was lowered by approximately one volt. Note negative pulse shift.

Test 5, Figure 22C used a 1.2 x 50 wave shape, applying 1000 volts at 66 amperes. The device clamped at 12 volts with no negative excursion.

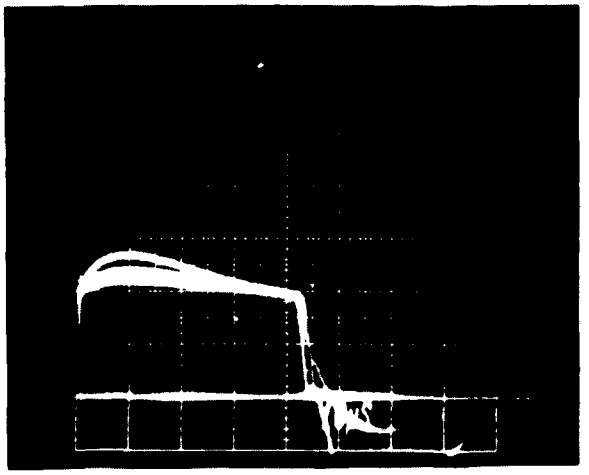

A. Test 1. 500 Volts 24 Amperes
Test 2. 1000 Volts 49 Amperes
Test 3. 1000 Volts 98 Amperes

8 x 20 Waveshape

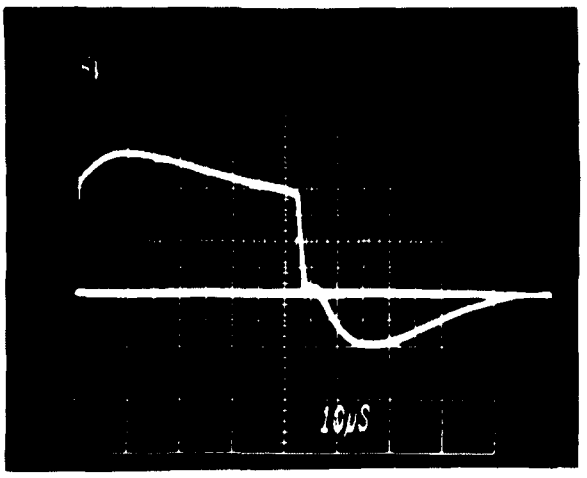

B. Test 4. 1000 Volts 98 Amperes
(Non-inductive spring)
8 x 20 Waveshape

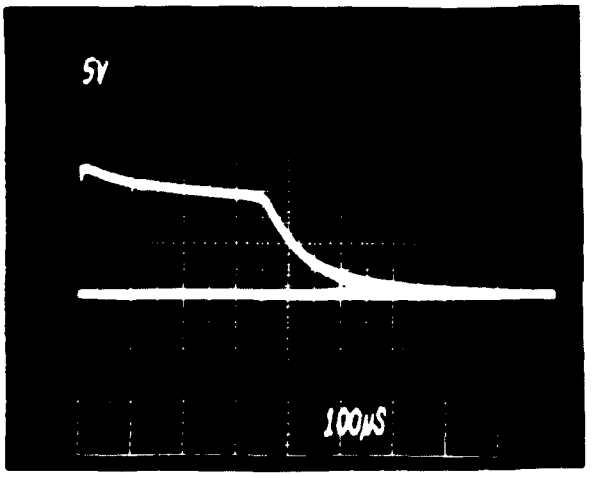

C. Test 5. 1000 Volts 66 Amperes
(Non-inductive spring)
1.2 x 50 Waveshape

Figure 22

Surge Tests

2GZ60316B (Bipolar Connected) in LPMC FA9479

CONCLUSION AND RECOMMENDATIONS

A. Conclusion

Square wave tests on the FA9455A barrier strip type protection module, insertion loss tests on the FA9479 coaxial module and surge testing of both modules indicated that within test parameters, the modules are limited only by the characteristics and capabilities of the surge suppressor devices used. i.e. They are device limited. However, a series of tests* performed by Illinois Institute of Technology Research Institute to determine effectiveness in supressing EMP did indicate a problem in handling short, nanosecond, impulses.

B. Recommendations

The conical spring used in both types of modules should be replaced with a "Belleville washer" type spring such as described in the introduction and pictured in Figure 3. This will require minor modification of the caps for both devices.

*Program conducted under Task 3 of Sub-contract Number S-79-01001 between the Florida Institute of Technology and the IIT Research Institute.

APPENDIX A

Return loss is a term used to describe the degree of mismatch introduced by a TranZorb in a coaxial line. Whereas transmission loss (or insertion loss) is defined as

$$\frac{P_{transmitted}}{P_{incident}}$$

Return loss is defined as

$$\frac{P_{reflected}}{P_{incident}}$$

Thus for a well matched line, the insertion loss in db would be close to zero, since the ratio of the transmitted to the incident power would be close to one. On the other hand, the return loss in db would be a large number, since the reflected power would be a small fraction of the incident power. Given the return loss, the transmission loss can be calculated.

Since $P_{incident} = P_{transmitted} + P_{reflected}$ the VSWR can be derived from the return loss as follows:
The return loss in db is defined as*

$$\text{Return loss, dB} = 10 \log_{10} |\Gamma|^2 \qquad (1)$$

Where $|\Gamma|$= magnitude of the voltage reflection coefficient.

Since

$$|\Gamma| = \frac{\rho-1}{\rho+1} \qquad (2)$$

$$\rho = \text{VSWR} \qquad (3)$$

we can write (1) as

$$\text{Return loss, dB} = 20 \log_{10} \frac{\rho-1}{\rho+1} \qquad (4)$$

Solving for ρ

$$\rho = \frac{1+10^{+\frac{(\text{return loss db})}{20}}}{1-10^{+\frac{(\text{return loss dB})}{20}}}$$

Note that the return loss is always a negative number or zero.

A similar computation can be performed to determine the VSWR from the transmission loss, using

$$\text{Transmission Loss (db)} = 10 \log (1-|\Gamma|^2)$$

and solving for ρ. Care should be taken to account for the power dissipated by the device under test when using transmission loss to determine the VSWR.

*Smith, Phillip H., "Electronic Applications of the Smith Chart," McGraw-Hill Book Company, New York, 1969, pp 37-38.

This paper is based on a report now in preparation for the Federal Aviation Administration. The study was performed by the Department of Electrical Engineering, Florida Institute of Technology as a participant in the Post Doctoral Program at the Rome Air Development Center. The effort was conducted via RADC Job Order No. DOT-FA 72 WAI-356.

It should be noted that trade or manufacturers names appear herein solely because they are considered essential to the object of this paper. TransZorb is a registered trademark of General Semiconductor Industries Inc. Data from the catalog is used with permission of that company.

FURTHER THOUGHTS ON LOCATION OF LIGHTNING STRIKE ZONES ON AIRCRAFT

J. Anderson Plumer
Lightning Technologies, Inc.
560 Hubbard Avenue
Pittsfield, Massachusetts 01201

ABSTRACT

In its advisory circular 20-53 "Protection of Aircraft Fuel Systems Against Lightning", the FAA has defined three lightning strike zones for the purpose of establishing the environment to be protected against at various locations on an aircraft. More recently, SAE Committee AE4L has refined these definitions to remove some ambiguities that have existed and permit a more definite environment to be established for design and qualification test purposes. Neither the original FAA nor SAE Committee definitions, however, prescribe the actual locations of these zones on a particular aircraft; nor is this their intent. The locations of each zone are dependent upon the aircraft's geometry and operational factors, and may vary from one aircraft to another. Actual zones are usually established by the aircraft designer by reference to past inflight experience with aircraft of similar design or with the aid of lightning strike tests on scale models.

This paper addresses some of the questions that have arisen recently concerning establishment of zone locations and boundaries. For example, an aircraft nose has always been considered to be in zone 1A (a direct strike zone with low probability of flash hang-on), but the rearward extent of this zone has not often been established. Whereas a lightning leader will almost always attach to the forwardmost extremity of a nose, continued movement of the aircraft may sweep the leader channel alongside the aircraft for a finite distance prior to completion of the flash and arrival of the first return stroke (which is included in the zone 1A environment). In the past, the rearward extent of zone 1A has been of little interest because most fuselage structures have had aluminum skins that easily withstand zone 1A lightning currents. Replacement of aluminum skins with advanced composites, however, makes this aspect of lightning strike zone location take on much greater importance. Analysis shows that for some aircraft, zone 1A may extend several meters aft of the nose or other leading edges, and some in-flight lightning strike incidents tend to confirm this. The altitude and speed of the aircraft are shown to be important factors in establishing zones, and in determining the probability of severe strikes within these zones.

BACKGROUND

For the purpose of establishing the lightning strike environment to be protected atainst at various locations on an aircraft, the FAA, in it's Advisory Circular No. AC 20-53[1] on protection of aircraft fuel systems against lightning, has defined three lightning zones as follows:

(1) Zone 1.

(a) All surfaces of the wing tips located within 18 inches of the tip measured parallel to the lateral axis of the aircraft, and surfaces within 18 inches of the leading edge on wings having leading edge sweep angles of more than 45 degrees.

(b) Projections such as engine nacelles, external fuel tanks, propeller disc, and fuselage nose.

(c) Tail group: within 18 inches of the tips of horizontal and vertical stabilizer, trailing edge of horizontal stabilizer, tail cone, and any other protuberances.

(d) Any other projecting part that might constitute a point of direct stroke attachment.

(2) Zone 2. Surfaces for which there is a probability of strokes being swept rearward from a Zone 1 point of direct stroke attachment. This zone includes surfaces which extend 18 inches laterally to each side of fore-and-aft lines passing through the Zone 1 forward projection points of stroke attachment. All fuselage and nacelle surfaces, including 18 inches of adjacent surfaces, not defined as Zone 1 are included in Zone 2.

(3) Zone 3. Surfaces other than those covered by Zones 1 & 2. Ignition sources in these areas would exist only in the event of streamering.

c. In connection with the foregoing the following definitions apply:

(1) Corona: A luminous discharge that occurs as a result of an electrical potential difference between the aircraft and the surrounding atmosphere.

(2) Streamering: The branch-like ionized paths that occur in the presence of a direct stroke or under conditions when lightning strokes are imminent.

(3) Swept Stroke: A series of successive direct strikes swept across the surface of the airplane by the motion of the airplane.

(4) Direct Stroke Attachment: Contact of the main channel of a lightning stroke with the aircraft.

Over the years, the terms "swept stroke" and "swept stroke Zone" have become synonymous with zone 2, and the terms "direct strike" and "direct strike zone" have meant zone 1, although this relationship has not been specifically stated in AC 20-53. This usage may be unfortunate, as will become evident.

AC 20-53 and prior editions were originally written for application to aircraft fuel system protection, an area of primary concern. Due to the absence of advisory material on protection of other structures and systems, the zone definitions of AC 20-53 have been widely used to establish protection requirements for the entire aircraft. An example of the application of these definitions to a transport category aircraft is shown in Figure 1.

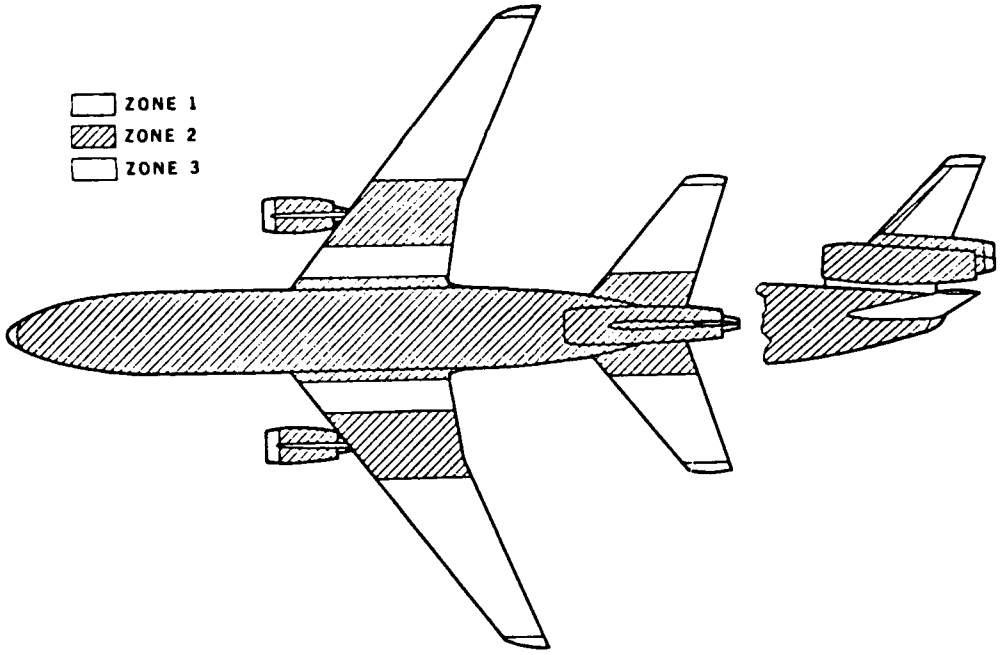

Figure 1 - Typical Aircraft Lightning Strike Zones, Determined from the Definitions of FAA Advisory Circular 20-53.

In accordance with the FAA definitions, the zone 1 regions included all surfaces of the aircraft that are located within 18 inches of the wing tip (measured parallel to the lateral axis of the aircraft), projections such as the nose, nacelle leading

edges and tail. Whereas the FAA definitions describe zone 1 as being ".....within 18 inches of.....(the) trailing edge of the horizontal and vertical stabilizer, tail cone and any other pertuberances" they do not apply the 18 inch criteria to surfaces behind leading edges. By custom, however, the first 18 inches aft of a leading edge or other forward-projecting object have also been considered to be within zone 1. Surfaces further aft of zone 1 areas, including "....areas 18 inches laterally to each side of fore-aft lines passing through the zone 1 forward projection points of stroke attachment" have traditionally been considered within zone 2. Since a lightning flash may exist for up to one second (or more, on occasion) and most aircraft can travel more than their own length in this time, the zone 2 regions have usually been extended all the way aft along the fuselage or across the wing, as was done for the aircraft in Figure 1.

While no rationale for the FAA definitions is included in AC 20-53, the 18 inch lateral extensions of zone 1 and 2 account for the typical scatter of lightning attachment points in direct strike areas and the tortuosity of the flash channel as it sweeps along zone 2 surfaces. In-flight lightning strike experience has tended to confirm this judgment. Thus, in the example of Figure 1, direct strike zones extend inboard 18 inches at the wing tips, and the swept stroke zones across the wings are 36 inches wider than the maximum width of the engine nacelles. The inboard 18 inches of each wing are also in zone 2 due to their proximity to the fuselage.

The significance of either of the lightning strike zones, of course, is that skins, structures and other objects located in these zones must be designed to tolerate the effects of direct or swept lightning strike attachments. In Figure 1, for example, the integral fuel tank skins aft of the nacelles were required to be thick enough to withstand swept lightning strike currents, whereas skins in zone 3 would perhaps not have to be this thick.

After the guidelines of AC 20-53 were in use for a time, several problems became apparent in interpretation of its "requirements". Among these are:

1. No differentiation is made between mid-wing or mid-fuselage surfaces and trailing edges, even though the lightning damage to be expected at trailing edges is known to be much greater than elsewhere, due to the longer dwell times involved.

2. The protection guidelines of AC 20-53 appear to require protection of hardware in zone 2 against the same intensity of current (200,000 amperes) as is suggested for objects in zone 1, even though the actual lightning environment in these two zones is widely acknowledged to be different.

Accordingly, the FAA zone definitions were refined by the Society of Automotive Engineers (SAE) Committee AE4L on lightning (formerly called Special Task F of Committee AE4) to accommodate the different lightning environments appearing at forward and trailing edge regions. This was accomplished by subdividing the original definitions to provide for low and high probabilities of flash hangon. The SAE Committee definitions[3] are:

"*Zone 1A:* An initial attachment point with a low probability of flash hang-on, such as a leading edge.

Zone 1B: An initial attachment point with a high probability of flash hang-on, such as a trailing edge.

Zone 2A: A swept-stroke zone with a low probability of flash hang-on, such as a wing mid-span.

Zone 2B: A swept-stroke zone with high probability of flash hang-on, such as a wing inboard trailing edge.

Zone 3: All of the vehicle areas other than those covered by Zone 1 and 2 regions. In Zone 3 there is low probability of any attachment of the direct lightning flash arc. Zone 3 areas may carry substantial amounts of electrical current but only by direct conduction between some pair of direct or swept stroke attachment points."

For aircraft design and certification test purposes, the SAE Committee has also established lightning currents to be expected in each zone. For this purpose, an idealized representation of the components of a complete lightning flash has been defined[4] and is reproduced in Figure 2.

The current components to be expected in each zone are illustrated in Figure 3. The shaded components apply in each zone indicated.

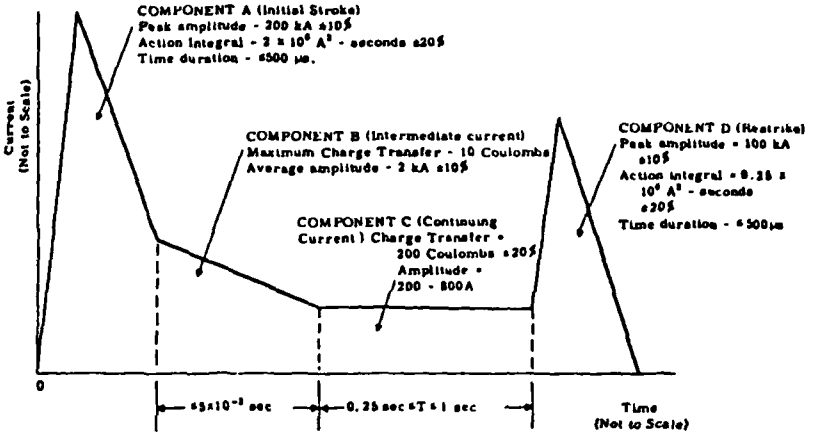

Figure 2 - Idealized Current Waveform Components for Qualification Tests.

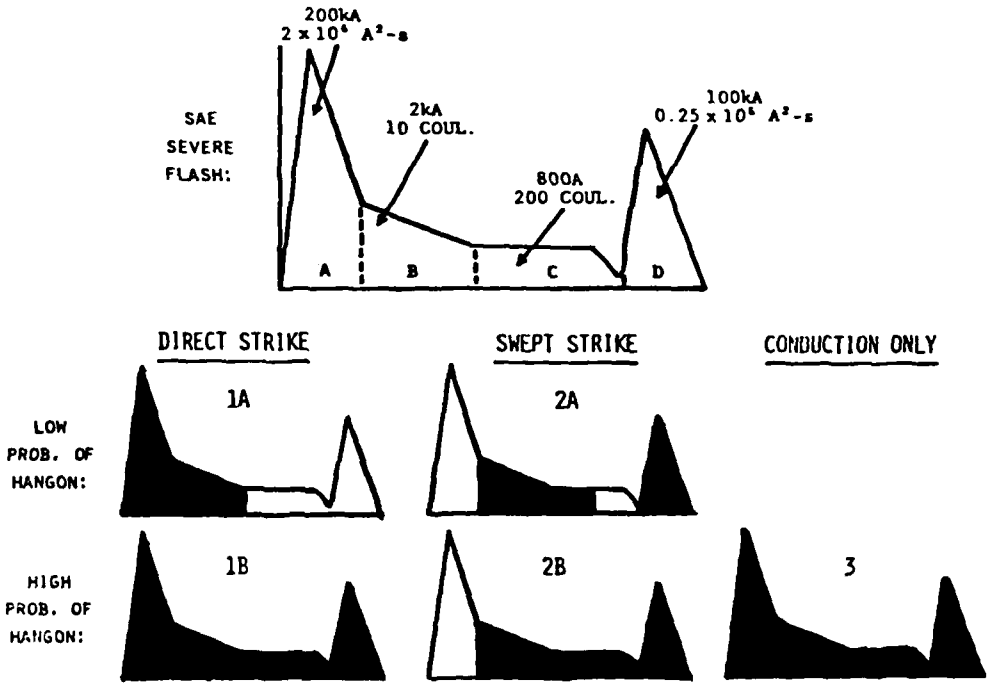

Figure 3 - Lightning Current Components Expected in Each Zone.

THE PROBLEM

In Figures 1 and 4 the zone 1 or 1A areas at the nose and other leading edges were extended aft a distance of 18 inches in accordance with traditional practice. Dielectric structures such as the radome, of course, were considered as being entirely within zone 1 even though their length is often longer than 18 inches, but in other cases the 18-inch criteria has been followed.

For conventional aluminum skins, the line of demarcation between zone 1A and 2A (or between zone 1 and 2 using the AC 20-53 definitions) is of little practical importance, because most aluminum skins can withstand even the first return stroke (SAE current component A) with little damage.

If the skin or structure aft of a leading edge attachment point is made of advanced composites, or other poorly conducting materials, the rearward extent of zone 1A becomes of critical importance. Many graphite-reinforced composites can tolerate the effects produced by the zone 2A currents without requiring additional protection, but the return stroke (component A) designated for zone 1 in the SAE criteria can deliver eight times as much energy than the re-strike current (component D) included in the zone 2A requirement, and the resulting damage can be extensive unless protective coatings or other methods have been applied. Most protective measures add weight and increase cost. Thus, a decision regarding whether to apply protection or not, (or even whether or not a composite should be utilized in the first place), may depend directly on the designation of the lightning strike zones, and especially on a realistic determination of the rearward extent of zone 1A.

The significance of the "A" and "B" designation can be seen in the currents specified for zones 1A and 1B. Due to the short hang-on time for an initial strike to a zone 1A surface, only current components A and B, are applied. But all of the current components will be experienced by trailing edge surfaces in zone 1B.

An example of an application of the SAE zone definitions is shown in Figure 4. The designations of Figure 4 were determined from a scale model test, in which a small percentage of strikes attached to the wing leading edge and to antennas along the top and bottom of the fuselage. Until recently[5], attachments to the leading edges of conventionally-shaped wings (other than those behind propellers) were not known to have occurred in flight. The recent exception was a strike to the wing of an Airforce transport aircraft well inboard of the tip, which is thought to have caused a fuel tank explosion that resulted in loss of the aircraft. Interestingly, this was also a high-wing aircraft.

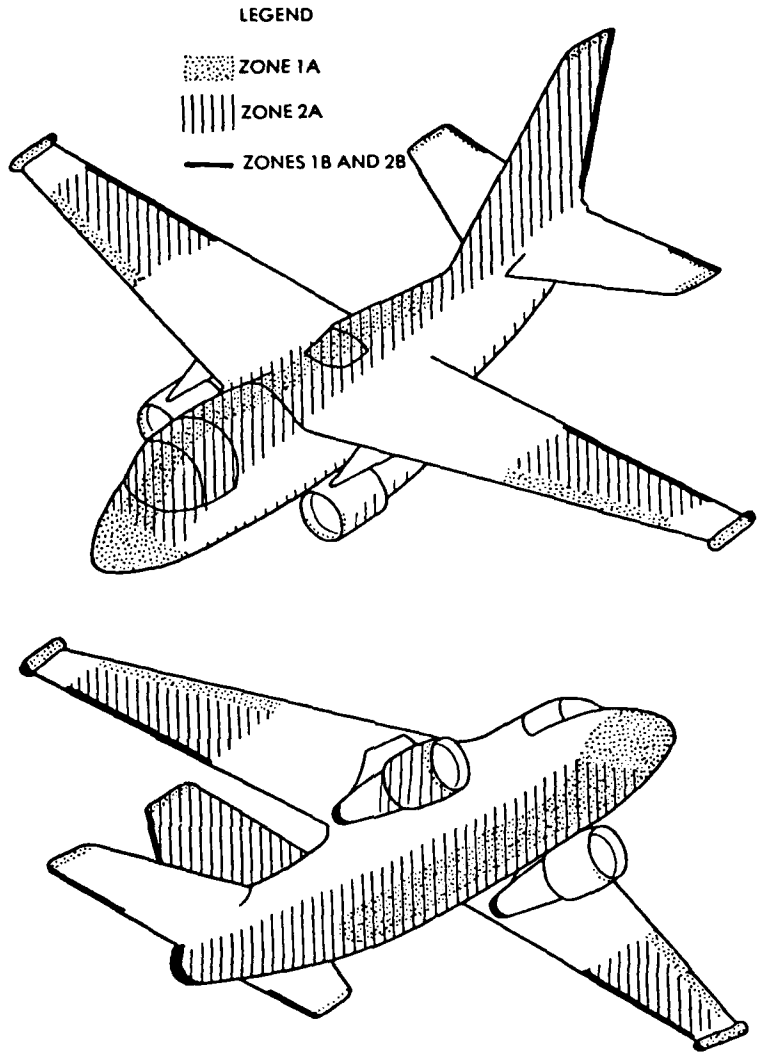

Figure 4 - Lightning Strike Zones Determined from Scale Model Attachment Point Test, Using SAE Zone Definitions.

The question of zone 1A extent became important to this writer when confronted with several aircraft structures made extensively of graphite or kevlar ™ reinforced composites. At first glance, it might be considered that only the nose or leading edges and surfaces within 18 inches of these edges are in zone 1A, but whereas zone 1A is defined as an "initial attachment point" the lightning environment for it includes the first return stroke, current component A.

Study of a number of lightning strike incidents in which moderate-to-severe damage occurred at forward locations

indicates that in some cases the return stroke may not arrive until the lightning channel has swept considerably farther than 18 inches aft of the nose or leading edge. This is because a finite period may elapse between the time the *leader* initially attaches to a leading edge extremity and when the leader has reached its destination and the return stroke is initiated.

During this period the aircraft has moved a finite distance and the leader channel has been drawn aft alongside the structure, reattaching periodically to spots in its path. This situation is illustrated in Figure 5.

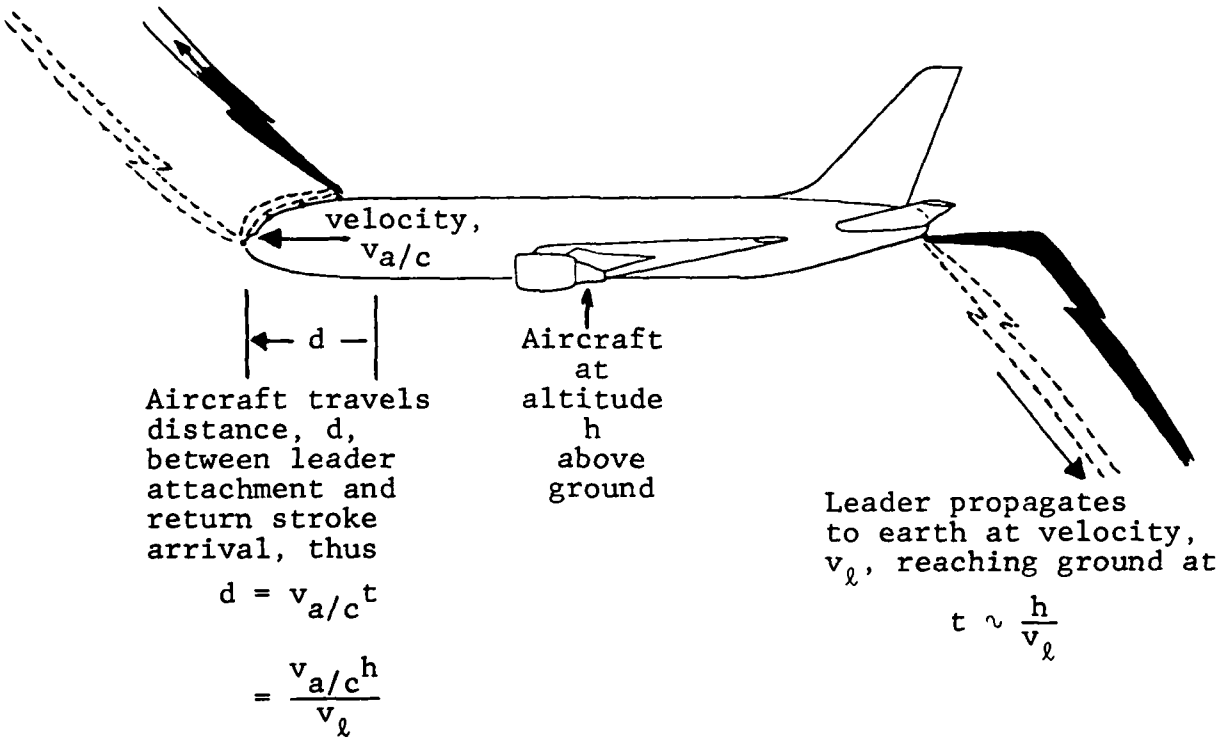

Figure 5 - Leader and Return Stroke Attachment Process.

As shown in Figure 5, while flying at a velocity ($v_{a/c}$) the aircraft travels a distance (d) during the time (t) over which the leader is continuing its propagation to earth. This time depends on the leader velocity (v_ℓ) and the aircraft's altitude (h). Thus, the distance traveled is related to the other parameters by:

$$d \sim \frac{v_{a/c}h}{v_\ell} \qquad (1)$$

The time at which the leader reaches the earth may be assumed to be synonymous with the time the return stroke reaches the

aircraft because once initiated, the return stroke travels back up the channel at a much higher velocity of about one third the speed of light.

A typical lightning leader travels at about 1.5×10^5 meters per second[6]. (If this leader struck the nose of an aircraft traveling 134 m/s (300 miles per hour) at an altitude of 3 kilometers (10,000 ft) the aircraft would have moved about

$$d \sim \frac{(134\,m/s)(3000\,m)}{(1.5 \times 10^5\,m/s)} \sim 2.68\,m \qquad (2)$$

Assuming that the leader channel may sweep aft and reattach to a spot this same distance aft of the initial leading edge attachment point. Surfaces this far aft of the leading edge are within zone 1A.

The foregoing analyses are based on a cloud-to-ground lightning flash situation. A similar mechanism would probably exist for cloud-to-cloud discharges, about which less is known. Since cloud-to-ground flashes are generally believed to present the most serious environment, the analyses in this paper will continue to represent the cloud-to-ground case.

LEADER VELOCITY

The velocity of a typical cloud-to-earth lightning leader has been determined by high speed photography and reported by many researchers as being about 1 or 1.5×10^5 m/s. Schonland, Malan and Collens[6], for example, reported in 1935 that the average velocities of 24 stepped leaders of negative polarity ranged from 1×10^5 to 13×10^5 m/s. Orville and Berger[7] measured a mean velocity of 2.5×10^5 m/s for an upward-progressing positive leader from a tower on Monte San Salvatore in 1965. Uman[8] reports a typical average stepped leader velocity as 1.5×10^5 m/s in 1972, and more recently Fieux et al[9], have estimated leader velocities of the order of 0.2×10^5 to 1×10^5 m/s. Elsewhere in the literature one finds the values of 1×10^5 or 1.5×10^5 m/s quoted most widely. It seems appropriate, therefore, to utilize velocities in this range for analyses of aircraft distance traveled in equation 1.

DISTANCE TRAVELED VS. FLIGHT CONDITIONS

From equation (1) it is evident that the distance (d) which the aircraft travels between the time of leader attachment and return stroke arrival is dependent on the aircraft velocity and altitude, in addition to the leader velocity. Figure 6 shows the

distances that may be traveled under the ranges of altitude and velocities throughout which most aircraft operate, as determined from equation 1.

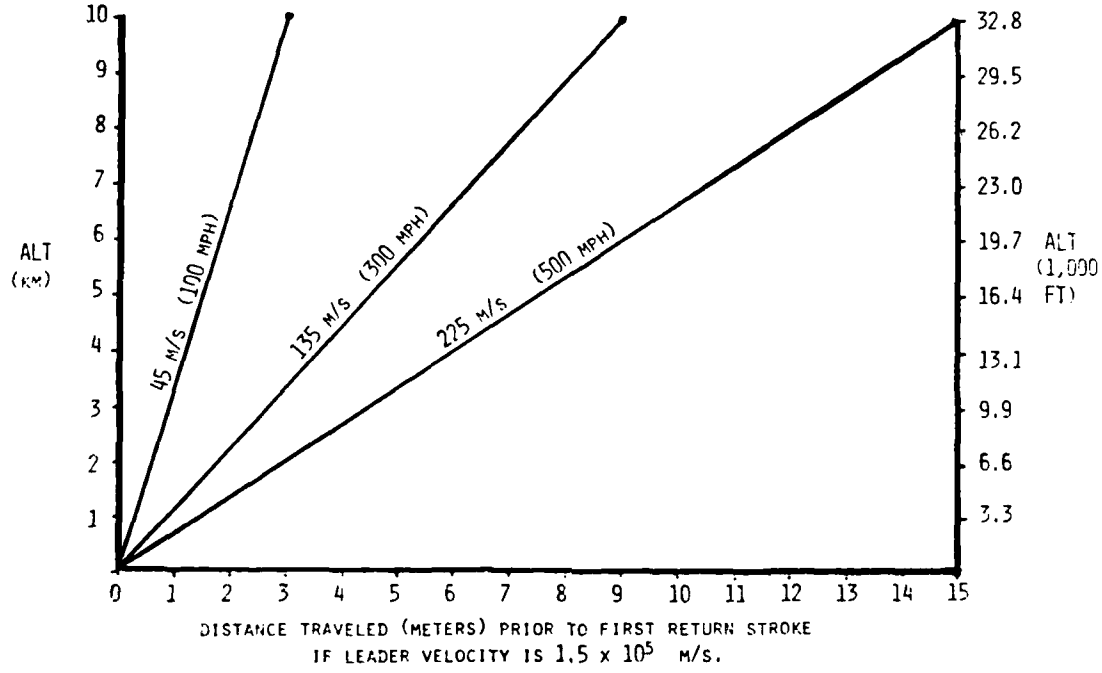

Figure 6 - Aircraft Distance Traveled prior to Return Stroke Arrival at Aircraft as a Function of Aircraft Speed and Altitude for Leader Velocity of 1.5×10^5 m/s.

From Figure 6 it may be seen that a turbojet aircraft cruising at 225 m/s (500 mph) at an altitude of 9 km (29,500 ft) would travel 13.5 m during the time it would take a lightning leader traveling 1.5×10^5 m/s to reach the earth and initiate the return stroke This is more than the entire length of some corporate jet aircraft, and implies that surfaces along the entire length of such an aircraft may, at times, be exposed to the first return stroke of a lightning flash. Since the first return stroke is considered a part of the zone 1A environment, surfaces of the aircraft that are exposed to the swept leader channel are within zone 1A.

On the other hand, a propeller-driven aircraft whose flight envelope extends only to a speed of 135 m/s (300 mph) and an altitude of 3 km (10,000 ft) would travel only 2.7 m before return-stroke arrival at these conditions. Aircraft surfaces aft of this distance would experience only the re-strikes, intermediate and continuing currents characteristic of zone 2A.

The results of Figure 6 were based on a leader velocity of 1.5×10^5 m/s. If the actual leader velocity is slower than this,

the aircraft will travel farther before the return stroke is initiated, and if the leader is faster, the converse will be true. Figure 7 shows the ranges of aircraft distances traveled permitted by leaders traveling between 1×10^5 and 2×10^5 m/s. Figures 6 and 7 may thus be utilized to estimate the possible rearward extension of zone 1A for nearly all flight conditions presently in use.

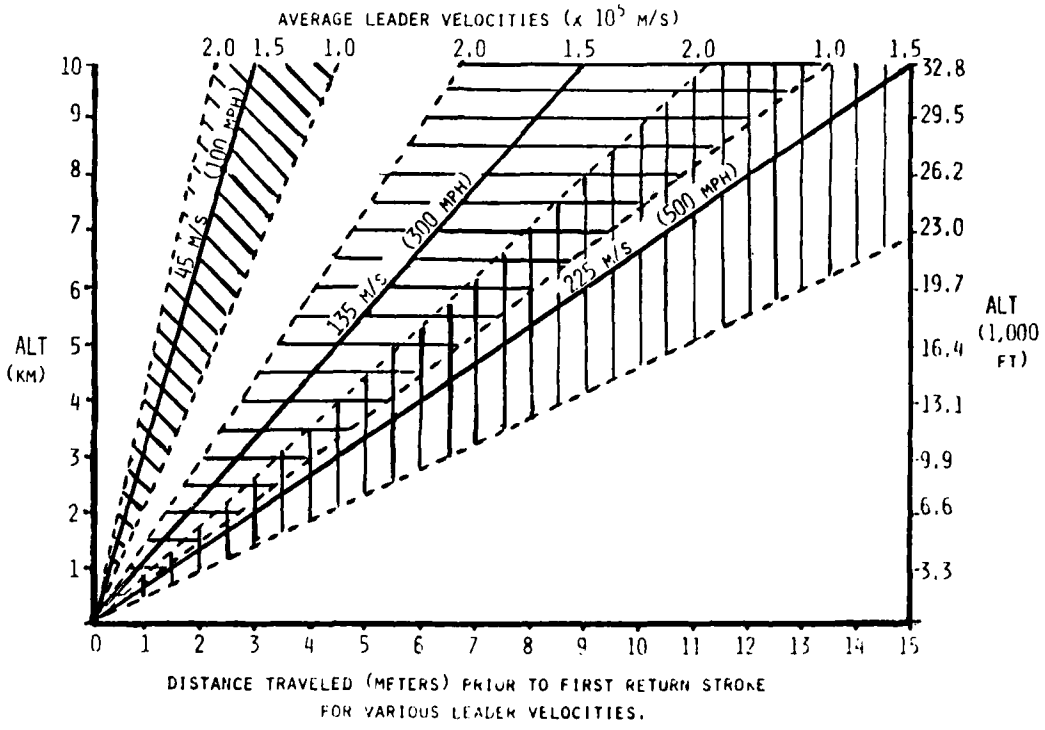

Figure 7 - Aircraft Distance Traveled prior to Return Stroke Arrival at Aircraft as a Function of Aircraft Speed and Altitude for Leader Velocities of between 1×10^5 and 2×10^5 m/s.

APPLICATION CONSIDERATIONS

Since many of today's business as well as commercial transport and military aircraft are being designed to operate at high altitudes and speeds, a large portion of their surfaces aft of initial leader attachment points would, by the results of Figures 6 and 7, be considered as within zone 1A. The significance of this has been academic for conventional aluminum structures because aluminum skins can tolerate the lightning environment defined in Reference 4 for zone 1A about as well as the currents defined for zone 2A. Skins and structures made of advanced composites, however, are likely to suffer much greater damage from the first return stroke (SAE current component A) defined for zone 1A as compared with the re-strike (SAE current component D) defined for zone 2A

due to the higher action integral involved (2.0×10^6 $A^2.s$ as compared with 0.25×10^6 $A^2.s$). External protection is frequently required for composites in zone 1A, whereas it often is not for composites that need only be designed to withstand the zone 2A environment. Since some external protective measures entail considerable weight and cost penalties it is important to consider probability factors in establishing the rearward extent of zone 1A on particular aircraft. In particular, there are several factors that combine to reduce the probability of experiencing a zone 1A-type stroke at the altitude and velocity extremes of the aircraft's flight envelope to an acceptable-risk level, as follows:

Most Strikes Occur at Lower Altitudes

Pilot report surveys[10] indicate that most lightning strikes occur when the aircraft is flying between 1.5 km (5,000 ft) and 6 km (20,000 ft), when the aircraft is climbing or descending. Several such surveys are presented on Figure 8. This means also that the aircraft velocity is sometimes less than cruise, with the result that strikes in the upper and right-hand regions of Figures 6 and 7 are less probable.

Most Severe Strikes Occur at Lower Altitudes

Though not without exception, most strikes that have inflicted severe damage to aircraft have occurred at altitudes of 6 km or less, and many of these are at altitudes below the cloud base of 3 km. In most of the cases of severe damage or loss of the aircraft that are known to this author, the strike occurred at 3 km or below. These, of course, are the return strokes intended for the zone 1A environment. In a few cases, severe damage has occurred at cruise altitudes of between 10 and 12 km.

Strikes at High Altitudes May Not Be Cloud - to - Ground

The foregoing analysis is based on leader propagation between a cloud and the ground. It is probable that many of the strikes occurring at cruise altitudes above 6 km do not involve the ground, but propagate instead between upper level charge centers in or among the clouds. Much less is known about the nature of these cloud-to-cloud (or intracloud) flashes, but it is probable that their leader propagation times are shorter than those of cloud-to-ground flashes originating at high altitudes. Again, this factor tends to reduce the probability of occurrences in the upper region of Figures 7 and 8, but does not eliminate this possibility. Flashes originating in the upper reaches of a cloud have been observed to propagate all the way to ground.

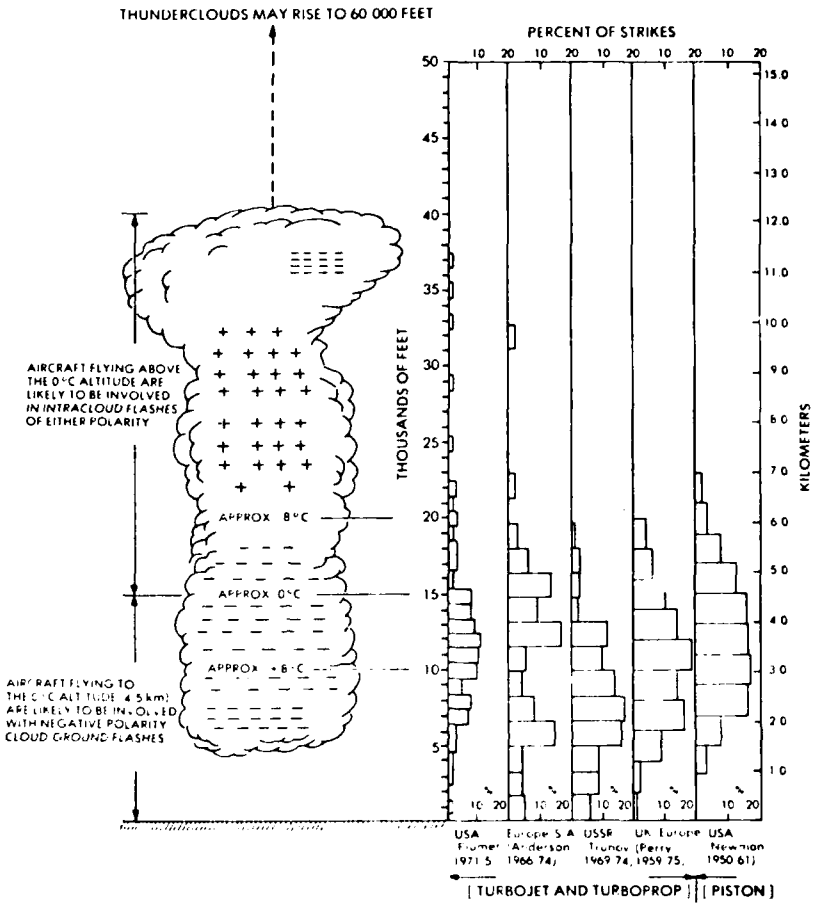

Figure 8 - Aircraft Lightning-Strike Incidents vs Altitude.

Rationale for Zone 1A Establishment

With the above factors in mind, the information of Figure 7 can be used to establish the lightning strike zones of a particular aircraft for design and qualification test purposes. The rationale might proceed as follows:

1. All aircraft *extremities* such as the nose, wing and empennage tips, tail cone, wing-mounted nacelles and other significant projections should be considered within a direct strike zone because they are probable initial leader attachment points. Those that are forward extremities or leading edges should be considered in zone 1A, and extremities that are trailing edges should be in zone 1B, in accordance with the definitions of Reference 3.

2. Since all aircraft fly at some time at altitudes below 6 km, the minimum rearward extension of 1A zones on a particular aircraft should be determined by the intersection of the aircraft velocity line with this altitude on Figure 7. The highest velocity at which the aircraft operates for an appreciable time within this altitude should be used. If the aircraft never reaches 6 km, its normal cruise altitude should be used instead. The aircraft velocity line associated with a leader velocity of 1.5×10^5 m/s is adequate. The 1.0×10^5 and 2.0×10^5 leader velocities will provide more or less conservative results.

   For most of today's aircraft, the above procedure will result in a rearward extension of zone 1A of 4-6 m.

3. For some aircraft that cruise extensively at higher-altitudes and speeds, a further extension of zone 1A may be appropriate, *especially if the probability of a flight safety hazard due to a strike to an unprotected surface is high.* But since the probability of severe strokes at the higher altitudes is lower, such further extension of zone 1A may not otherwise be necessary. In other words, if the flight-safety criticality of the surface (or other component in question) is high, it should be considered as in zone 1A and protected accordingly. If not, it may be designed in accordance with the zone 2A lightning environment, which may require no additional protection.

4. Since nearly all aircraft can travel more than their entire length in the one-second (or so) lifetime of a typical lightning flash, the balance of the surfaces aft of zone 1A should be considered within zone 2A. Trailing edges should be considered in zone 1B or 2B, depending upon whether they were reached by an initial strike (zone 1B) or a swept strike (zone 2B), in accordance with the definitions of Reference 3. Surfaces 0.5 m (18 in.) to either side of those surfaces actually in the line of flight should also be considered within the same lightning strike zone, to account for small lateral movements of the sweeping channel.

Using the above guidelines, the lightning strike zones on the transport aircraft of Figure 1 would be modified as shown on Figure 9. In each case, the zone 1A regions are extended aft at least 6 m from the initial leader attachment points at the nose and wing-mounted engine inlets. Surfaces further aft are in zone 2A, and trailing edges behind zone 2A are in zone 2B.

For aircraft of conventional aluminum structure the consequences of this further extension of zone 1A are minor. Aluminum skins of 10 mm (0.040 in.) or greater can usually withstand the zone 1A environment as well as that prescribed for zone 2A. Skins over integral fuel tanks are most vulnerable to the intermediate current (SAE current component B) which is included in *both* the zone 1A and 2A environments of Reference 4. If the skins or structure are made of advanced composites; however, they are likely to be most vulnerable to the stroke current, which is eight times more severe for zone 1A than for zone 2A. This is likely to affect the design of these structures, and may require that conductive coatings or other protective measures be incorporated in fuselage or engine nacelle skins, for example, that are now recognized as being within zone 1A.

CONCLUSIONS

Based on the analyses and in-flight experience reported above, the following conclusions can be drawn:

1. Zone 1A is Really a Swept Stroke Zone

The term "swept stroke" has heretofore been applied to strikes in zone 2 or 2A, but it clearly applies equally well to zone 1A. Nearly all first return strokes that occur to an aircraft will reach the aircraft in a swept leader channel.

2. The Rearward Extent of Zone 1A is Much More Important for Composite Structures

Whereas the rearward extent of zone 1A has heretofore been only of academic interest, it is very important to establish its possible extent over composite skins and structure.

3. An 18" Aft Extension is Often Inadequate, but the 18" Lateral Criteria, per FAA AC 20-53 is Appropriate

It has been shown that the channel may sweep rearward much farther than 0.5 m (18 in.) prior to return stroke arrival at the aircraft, so use of the "18-inch rule) to locate the rearward extension of zone 1A is not adequate. Use of this guideline to extend zone 1A in lateral directions has been shown by in-flight strike experience to be generally appropriate. The actual rearward extension of zone 1A is dependent upon the aircraft's flight envelope, and this may vary from one aircraft to another.

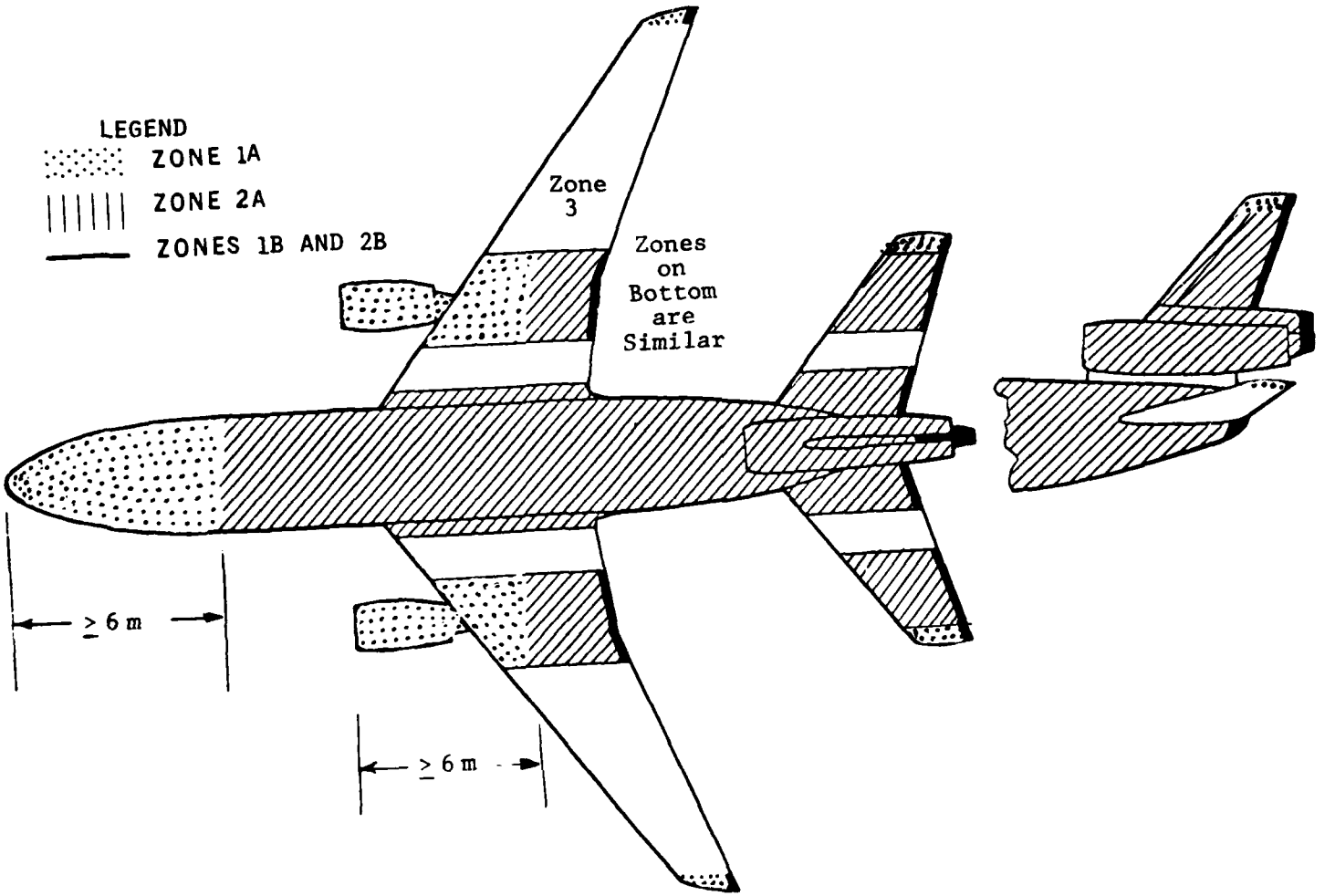

Figure 9 - Typical Aircraft Lightning Strike Zones Showing Rearward Extension of Zone 1A.

REFERENCES

1. U.S. FAA Advisory Circular 20-53 "Protection of Aircraft Fuel Systems Against Lightning" dated 10/6/67, paragraph 4b.

2. Amason, M.P., Cassell, G.J., Kung, J.T., La Manna, J.A. and McCloud, W.W., "Aircraft Lightning Prorection Design Considerations" published in the 1972 Lightning and Static Electricity Conference Papers, 12-15 December 1972, AFAL-TR-72-325, pp. 214-241.

3. "Lightning Test Waveforms and Techniques for Aerospace Vehicles and Hardware" Report of SAE Committee AE4L, June 20, 1978, pp. 4-5.

4. SAE Report, pp. 13.

5. Fisher, F.A. and Plumer, J.A., "Lightning Protection of Aircraft" NASA RP 1008, October 1977, p. 53.

6. Schonland, B.F.J., Malan, D.J. & Collens, H., 1935 Progressive Lightning: II. Proc. R. Soc. Lond. A 152, 595-625.

7. Orville, R.E. and Berger, K., "Spectroscopic and Electric Current Measurements of Lightning at the Monte San Salvator Observatory in Lugano, Switzerland" in Proceedings of the Fifth International Conference on Atmospheric Electricity held at Garmisch-Partenkirchen (Germany) 2-7 Sept 1974 edited by Hans Dolezalek and Reinhold Reiter Darmstadt: Dr. Dietrich Steinkopff Verlag 1977.

8. Uman, M.A., "Spark Simulation of Natural Lightning" in 1972 Lightning and Static Electricity Conference Papers, AFAL-TR-72-235, 12-15 December 1972, pp. 5-13.

9. Fieux, R.P., Gary, C.H., Hutzler, B.P., Eybert-Berard, A.R., Hubert, P.L., Meesters, A.C., Perroud, P.H., Hamelin, J.H. and Person, J.M., "Research on Electrically Triggered Lightning in France", IEEE Transactions on Power Apparatus and Systems, Vol. PAS-97, No. 3, May/June 1978, pp. 725-733.

10. Fisher, F.A. and Plumer, J.A., pp. 57-64.

PRECIPITATION STATIC IN GENERAL AVIATION AIRCRAFT

W.G. Butters
McDonnell Aircraft Company
McDonnell Douglas Corporation

INTRODUCTION

Precipitation static (P-static) has been experienced in aircraft for years. Conversations with pilots and crewmembers who were flying prior to the days of turbine powered equipment will elicit interesting tales of static charges and St. Elmo's Fire. This early experience with P-static usually proved to be of little consequence during routine flights because lower aircraft speeds would generally produce only moderate P-static problems.

Today's general aviation aircraft, however, carry an array of digital avionics that is very sensitive to P-static noise. With many aircraft that are in operation today, it is common to lose communication and navigation avionics while just flying through clouds, without heavy precipitation. In some severe cases an air data computer may act up or an R-nav system may lose all of its waypoints. In many cases P-static is the hidden cause of numerous avionics problems.

The McDonnell Aircraft Co. Lightning Simulation Laboratory has developed a portable P-static test set that has found extensive use in the field of general aviation aircraft. This paper will summarize the types of P-static problems found on operating aircraft.

P-STATIC SYMPTOMS

An increased awareness by pilots and by maintenance people of problems that can be caused by P-static is helping to isolate new avionics problems. A review of pilot reports often shows different symptoms with each problem that is encountered. The following list of problems is a summary of many pilot reports from many different aircraft. Each problem was caused by P-static:

- Complete loss of VHF comms
- Magnetic compass 30^{O} in error
- Aircraft flies with one wing low while autopilot is on
- High pitched squeal on audio
- Motor boat sound on audio
- Loss of all avionics in clouds
- VLF navigation system inoperative most of the time
- Erratic instrument readouts
- "Center" suggested repairing poor radios
- "St. Elmo's Fire" on windshield

In general, each of these symptoms is caused by one general problem on the airframe. This problem is the inablility of the accumulated charge from triboelectric charging (P-static) to flow easily to the wingtips and tail of the airframe, and be properly discharged to the airstream.

THE CAUSE OF P-STATIC

When an aircraft moves through the air it strikes microscopic sized particles of dust, snow, smoke, ice crystals, etc. These particles, in turn, deposit a charge upon the airframe at the point of impact. One ice crystal impact, for example, deposits up to 50$\mu\mu$ coul.[1] on the airframe. The accumulation of these charges on the aircraft and the subsequent corona discharge form the aircraft wingtips and tail is generally assumed to cause most of the P-static noise. Therefore static dischargers of one kind or another are usually installed on the aircraft. However, in practice it has been found that on business aircraft P-static problems are caused more often by sparking or streamering as charge moves on the aircraft. The electrical noise is not a direct result of the charge movement but rather is caused by electrical discontinuities in the airframe. Problem areas on the airframe can be isolated to general areas of concern such as poor bonding or improper treatment of dielectric surfaces. Each airframe, however, must be treated as an individual case. Because of different maintenance histories and operation of the various aircraft, these types of P-static problems vary from one aircraft to another, even among aircraft of the same type.

DISCHARGE WICKS

Very little information about static wicks exists in the general aviation community. There is a lot of misinformation and general lack of knowledge of how wicks work, where they should be placed, and what to avoid with static wicks.

Figure 1 shows one typical wick installation. In this example the wicks are bunched together and are not the resistive type. Although this installation will lower the corona threshold of the aircraft, it does not offer any noise attenuation benefits and thus avionics still suffer from the broadband RF noise.

Figure 2 is an example of three problems showing up on one installation. Two types of wicks are mounted in the same general location. The wick(s) with the lowest corona threshold will operate in a normal fashion but the remaining wick(s) will ride along as added weight. The second problem is that this installation has bunched the wicks in pairs in an attempt to achieve both mechanical strength and to reduce the electrical noise. In this approach, the strength is acheived but the close spacing of the wicks reduces their total effectiveness. This touches on the third problem of spacing. The wicks must maintain a space between each other so that their effectiveness will be maximized. These wicks must be placed far enough apart so that the corona discharge from each doesn't reduce the operational characteristics of the other.

Figure 3 is an example of two wicks that can interfere with each other's operation. Although their location on the airframe is correct, the second wick (on either wing) reduces the operational capability of both.

Figure 4 shows again a mixed wick installation but this aircraft has the "V" type of VOR antenna instead of the blade antenna as shown in Figure 3. This "V" antenna has a lower corona threshold than does the blade antenna. With the use of this antenna relatively modest amounts of P-static charge will cause the navigation receivers to lose signal.

FIGURE 1
STATIC WICK INSTALLATION

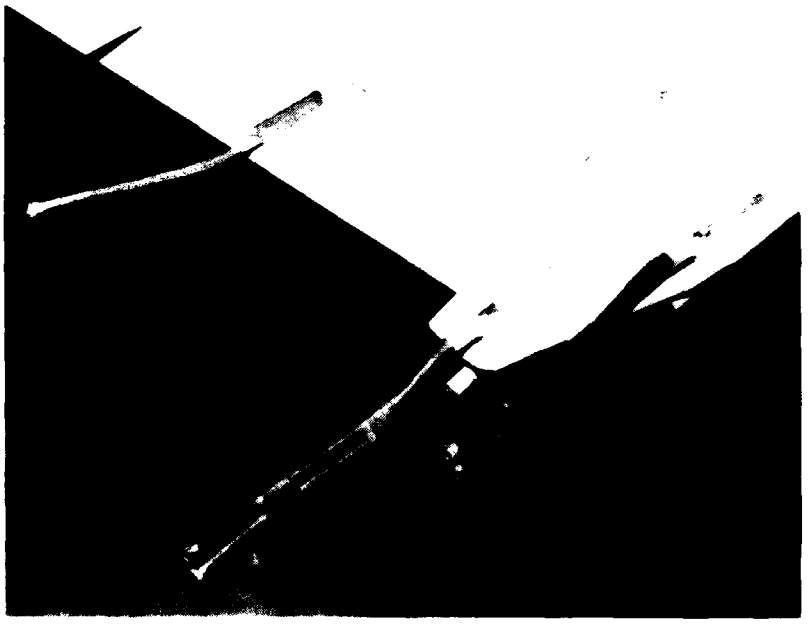

FIGURE 2
MIXED WICK INSTALLATION

FIGURE 3
CLOSE SPACED WICKS

FIGURE 4
MIXED WICK INSTALLATION

Aircraft Wing Problem Areas

The main problem area on the aircraft wing is at the leading edge boot or slat. In both cases when the aircraft strikes particles in flight the accumulated charge that develops upon the leading edge of the wing must migrate to the wingtip. This electron migration causes the charge to move aft and outboard where there are often airframe problem areas that can cause RF noise. At the seam of the leading edge boot or at the slat there can be a noise problem. If the boot has aged and pulled away slightly from the wing or if the slat has corrosion or a paint buildup combined with a grease dielectric film on the track, then the condition exists to have a P-static problem at these gap areas. The problem here is caused by charge jumping the small gap between the leading edge and the rest of the wing. This repetitive arcing generates the broadband noise that is received by the radios and in some cases enters the avionics by way of the interconnect wiring. Other instances have been found where field repairs or modifications have resulted in isolated pieces of metal in the current flow path which lead to arcing under P-static conditions. A leading edge boot installation is shown in Figure 5.

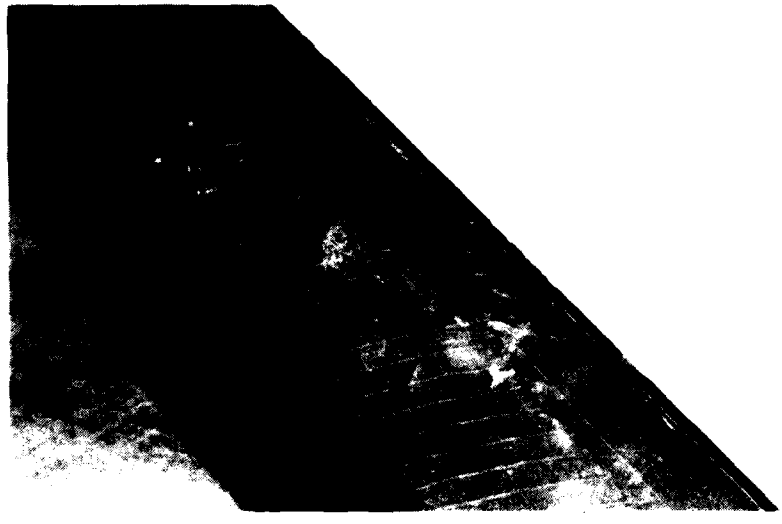

FIGURE 5
LEADING EDGE BOOT

Aircraft Windshield Problems

The aircraft windshield is a source of P-static problems with some aircraft. As the charge accumulates on this dielectric surface, a clean nonconducting windshield will reach the flashover point. This flashover point is where the electrons discharge suddenly onto the airframe and generate R.F. noise. Some aircraft use windshields that are slightly conductive on the outer surface and eliminate this problem.

Figure 6 shows a high voltage test fixture that is mounted on the windshield of an aircraft to test for noise. The flat black plate is a conductive material that holds the sharp spikes that generate corona. The corona action causes electrons to be deposited on the aircraft's windshield. Figure 7 shows a similar test being performed on a lower communication blade antenna.

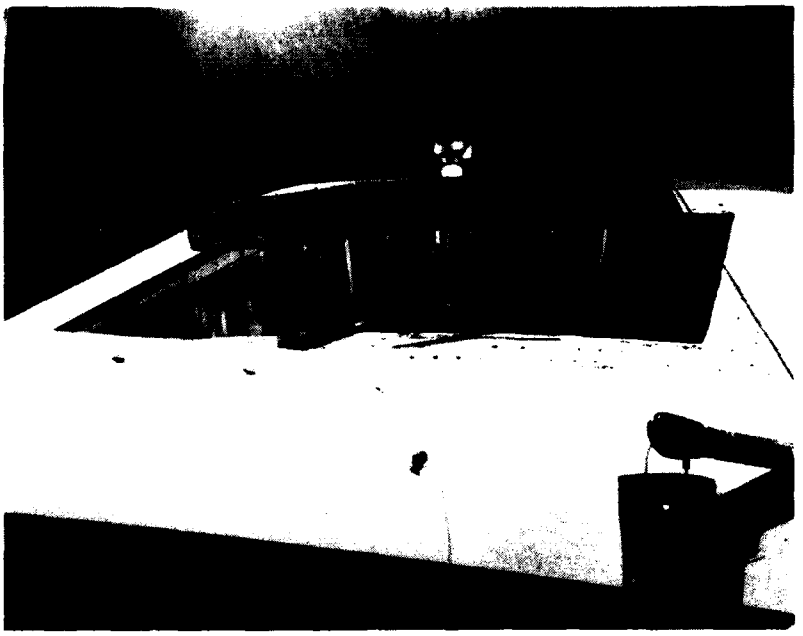

FIGURE 6
TEST FIXTURE ON A WINDSHIELD

FIGURE 7
TEST FIXTURE ON LOWER COMM ANTENNA

Aircraft Radome Problems

The last problem area, and one of the most common sources of P-static RF noise, is the radome. Here there are two sources of noise. The first source is the dielectric material of the radome. This material acts in the same way that the windshield does, in that the charges attempt to move to the airframe by flashing across the surface. If the radome has been coated with an antistatic paint, then the movement of these electrons is continuous and controlled and is noise free.

The second source of noise at the radome is the lightning diverter strip. These strips of metal often loose their good electrical bond to the airframe with small amounts of dirt and corrosion accumulating at the attachment point. When this electrical bond point is no longer a direct short, intense noise is generated by the microscopic spark gap that is located at this poor bonding point. Because this noise source is very close to the avionics bay and most of the associated aircraft wiring, this one source of noise can have a most devastating effect upon the avionics.

Testing for Noise

The location of trouble areas on each aircraft involves the use of various high voltage set ups to simulate the P-static charging. Each area on the aircraft is subjected to simulated P-static current flow while the aircraft avionics are monitored. By using high voltage probes at 30 to 50 thousand volts, each of the static wicks are probed for corona current flow. Here, poor base mounts, broken resistance elements, or poor airframe bonding will show up on the radios as noise.

The windshields, radome and antennas are tested as shown in Figures 6 and 7. With this test the high voltage is applied to a flexible plate that contains numerous sharp spikes (corona generators).[2] The charge from the spikes accumulates on the dielectric surface in a fashion similar to P-static buildup and if the surface is a source of RF noise then the result shows up on the avionics.

Because each aircraft is unique in its history and avionics installation, each must be approached as an individual test problem. In most cases, tests of the areas that have been mentioned as problem spots will reveal the location of P-static noise problems. The exact location of the problem can generally be found with the high voltage test probe technique very quickly. Most P-static tests require less than one day to setup equipment and locate the problem area.

Reference: (1) J. E. Nanevicz, "Static Electricity Phenomena: Theory and Problems," Conference on Certification of Aircraft for Lightning and Atmospheric Electricity Hazards, ONERA-Chatillon, France (September 1978).

Reference: (2) R. C. Twomey, "Laboratory Simulated Precipitation Static Electricity and Its Effects on Aircraft Windshield Subsystems," 1977 IEEE International Symposium on EMC, Seattle, Washington (August 1977).

GLOSSARY OF TERMS

Broadband noise -	radiated electrical energy causes a signal to be present over a large portion of the radio frequency spectrum and acts to "jam" normal tuned incoming radio signals.
Corona -	a blue electrical discharge (current) from a conductor into the air. At nightime this effect is seen as a glow around sharp pointed metallic objects.
Corona threshold -	a voltage level at which the airframe begins to discharge its accumulated electrical charge.
Dielectric surface -	a nonconducting material that is able to retain accumulated charge.
Electron migration -	The equalization of skin potential by the redistribution of electrons around its electrical conducting skin.
Lightning diverter strip -	a metal strip usually found on the radome, used as a protective device for the radome and radar in case of a direct stroke to the radome area.

LIGHTNING PROTECTION TECHNIQUES FOR RADOMES HAVING FORWARD MOUNTED PITOTS

A.W. Hanson
Culham Laboratory, England

This paper contains information derived during the course of contracts with the United Kingdom Ministry of Defence and the Swedish Ministry of Defence.

1. INTRODUCTION

For the most part aircraft with pitot booms mounted in front of the forward radome are supersonic, or very high speed aircraft, where the radar obscuration of a forward mounted pitot is traded off against the need for the pitot to be placed well forward in relatively undisturbed air. The long forward mounted pitot is the dominant stress raiser and this, coupled with the typical constructional features of radomes normally associated with forward mounted pitots, tends to relegate the problem of direct puncture of the radome skin to a position of low importance. The pitot boom is predominantly the major point of initial attachment in the radome region, and it is unlikely that the arc channel will develop sufficient voltage to puncture the radome during subsequent sweeping.

This paper therefore deals only with the problems that arise from a strike to the forward mounted pitot, and some possible solutions of these problems.

2. THE HAZARD OF THE UNPROTECTED PITOT

Consider the case of a forward mounted pitot having no electrical connections to the airframe, or the main electrical systems save for the pitot heater cables. This system has the operational advantage that any additional radar obscuration over and above that of the pitot boom itself can be kept to an absolute minimum. To this end the pitot heater cables cross-section will be no greater than that required to carry heater current. In the event of a strike to an unprotected pitot the lightning stroke easily punctures the pitot heater insulation, and flows to the airframe via the heater cables. The following effects then occur. Firstly a massive voltage transient is injected into the aircraft's electrical system, and secondly the heater cables can fuse explosively. The fusing of the cables and the subsequent lightning arc inside the radome causes dangerous over-pressures, and incidents have been recorded where such over-pressures have detached the radome from the aircraft, or have caused major structural damage to the airframe immediately behind the radome. Incidents have also been recorded where the injected voltage transients have had catastrophic effects on the aircraft's electrical and avionic fit. In one

case within the author's experience voltage transients in the pitot heater cables are believed to have caused the operation of the cockpit canopy ejection circuit.

3. PROTECTION AGAINST CURRENT IN THE HEATER CABLES

3.1 Case 1 - The External Divertor Strip

The first and obvious method of protecting the heater cables from the lightning currents is to provide an alternative, and preferred route, for the lightning currents. This is easily supplied by fitting an external conducting strip from the pitot boss to the main aircraft frame (see Fig. 1). In practice, where a two-wire heating circuit is used no lightning currents will flow in the cable and no voltage transient will be injected into the aircraft wiring so long as the heater insulation does not fail.

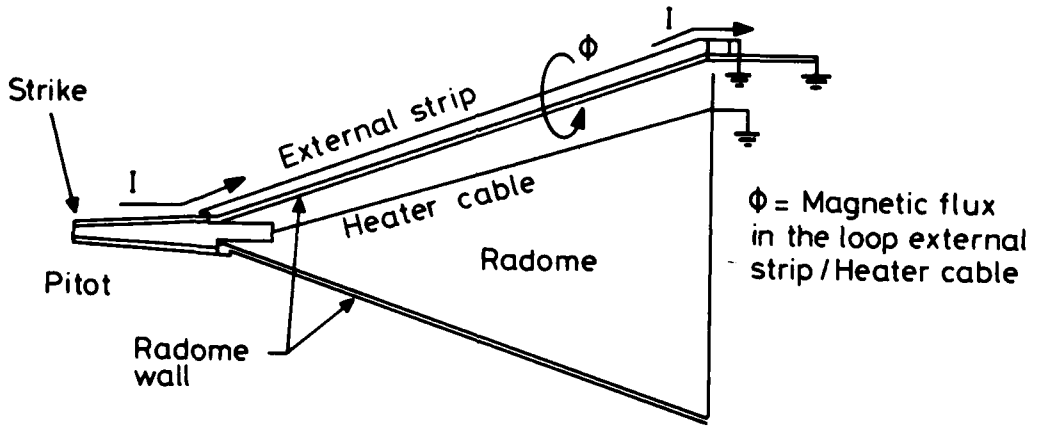

Figure 1 Protection by External Divertor Strip only

It should be noted that if the external strip is used as an 'earth return' for the heater circuit, this will bridge the heater insulation and will have the same effect electrically as a two-wire system having a failed insulation. All future comments in this paper therefore will relate to two-wire systems, and all 'single wire earth return' systems will be considered as two-wire systems with a failed insulation. Single wire earth return systems are clearly not suitable for this application.

Two types of voltage will stress the heater insulation. They are the resistive voltage drop along the divertor strip, and the voltage induced in the heater cable/divertor strip loop due to coupling with the rapidly changing magnetic field around the divertor strip. The permissible thickness of heater insulation is restricted by heat transfer requirements, and the levels of insulation achievable in a practical case could easily be breached by the inductively coupled voltages. The use of wires, or foils to reduce the radar

obscuration of an external divertor strip is also not acceptable. The external divertor must be able to carry the full action integral of the strike without melting or fusing, as the voltages appearing across the resulting arc would be sufficient to rupture the heater insulation, and thereby cause lightning currents to flow in the heater cables.

3.2 Case 2 - The Internal Lightning Divertor

The magnitude of the inductively coupled voltage stressing the insulation will be determined by the total flux which appears between the heater cables and the divertor strip. The closer the cables are to the divertor strip the less flux appears between them and the lower will be the voltage due to fast flux coupling that will stress the insulation. This is the case therefore for taking the divertor strip inside the radome. If the divertor strip is now made in the form of a circular cross-section tube which totally encloses the cable throughout its entire length, there will be no inductive coupling with the heater cables, and the only voltage stressing the heater insulation will be the IR drop along the divertor conduit. Unless the heater insulation fails no lightning currents will flow in the heater cables and no voltage transients will be injected into the electrical system. In the event of a heater insulation failure, the injected voltage transient will be limited to the IR drop in the divertor conduit, and this will probably be below the normal hardening level of the circuit. To work correctly the conduit must be well bonded at both the pitot and the airframe.

NOTE: The use of metallic air data lines as an internal divertor is not recommended, as it does not prevent magnetically coupled voltages, and lightning damage to the pipes could cause loss of air speed data.

3.3 Case 3 - Hybrid Systems

The combination of an internal conduit with a solid divertor strip can be used to reduce the IR voltage stressing the heater insulation. Alternatively it can be used to reduce the dimensions of the conduit in order to lessen the degradation of the radar performance, as the total action integral can be shared between the conduit and the additional divertor strip. The additional divertor strip may be either outside or inside the radome. In the former case the strip may be located in the 'radar shadow' of the conduit. Where an additional internal divertor is used it may be placed anywhere in the radome that best fits the radar performance requirements. This technique was applied successfully to a particular aircraft and the radar obscuration was minimised by using a copper conduit of only 5mm (0.2") outside diameter, together with a copper wire of only 2.5mm (0.1") diameter. Simply designed energy-absorbing rubber mountings formed part of an elegant and effective solution to the problems of the magnetic forces mentioned later in this paper. The system has been proven to give effective protection both by laboratory tests and by natural lightning strikes in service.

Systems using a conducting conduit totally enclosing the heater cables with or without additional divertors, can give complete protection against the previously mentioned hazards arising from a strike to the pitot boom. The

protection system itself however can be subjected to intense mechanical forces due to magnetic interaction between the currents in the different sections of the system, or between the currents in the system as a whole and the arc channel. These forces must be considered and the protective system designed to withstand them.

4 MAGNETIC FORCES

In natural lightning the maximum di/dt occurs close to the time of maximum current. The maximum magnetic forces therefore occur at a time when the current distribution in the protection system is inductively dominated. In calculating the forces the inductive current distribution in the system must be related to the position of the arc channel at peak current. Two extremes of arc channel interaction are considered.

4.1 Minimum Arc Channel Interaction

There will be no magnetic interaction between the protective system and the arc channel when the two lightning attachment points are the pitot head and the rear of the aircraft, with the lightning channel lying horizontally along the flight path (see Fig. 2).

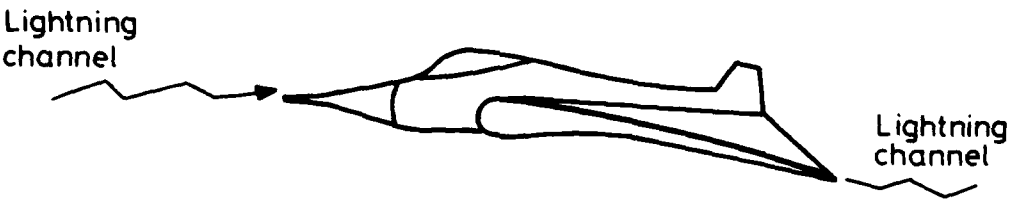

Figure 2 Minimum Arc Channel Interaction Situation

In these circumstances a simple system such as described in Section 3.2 will experience no gross magnetic forces although there may be some localised danger points as described later in Section 4.3.

In the more complex hybrid systems there will be some interaction between the two component parts of the system. The case of the external divertor strip is shown in Fig. 3.

The gross magnetic forces draw the two sections together. With an external strip 10mm wide and 30mm from the conduit the peak force for a 200kA pulse would be 66,000 N/m ($\sim$ 6.5 tons/m) for its entire length. It will be noted that the direction of the force is such that the system components are supported against these forces by the radome wall. Nevertheless with such high forces the conduit can be flattened against the radome wall or pierced by any external strip fixing screws that protrude through the radome wall.

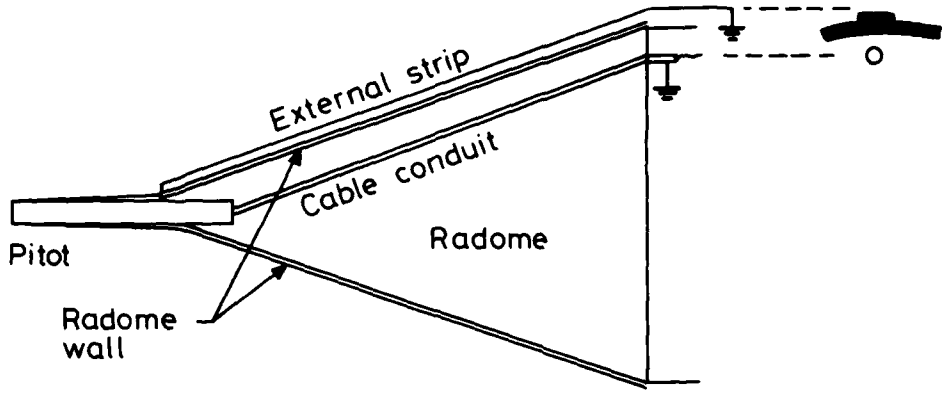

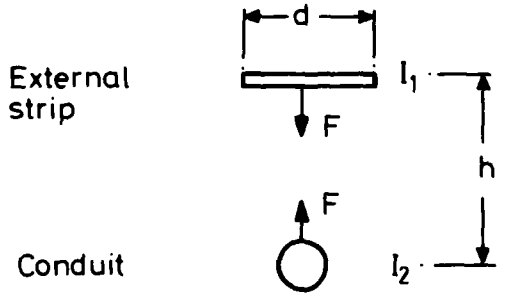

The conduit and the external strip are attracted to each other by force F as shown.

$$F = \frac{\mu_o I_1 I_2}{\pi d} \tan^{-1}\left(\frac{d}{2h}\right) \text{ Newtons/m}$$

Figure 3 Magnetic Forces on Conduit and External Strip for Minimum Arc Channel Interaction Condition.

The case of the internal additional divertor strip is shown in Fig. 4. Again the forces draw the two components together. The much greater distance between the conductors dramatically reduces the forces acting upon them over most of the distance. For example, at a point where the radome diameter is 1.5m a peak current of 200kA would produce a peak force of only 1,333 N/m (293 lbs/m). At the forward end, where the two conductors converge, the effect of their closer proximity is offset to some considerable extent by the wide angle between their two paths.

4.2 Maximum Arc Channel Interaction

If a step leader attaches to the pitot boom and then proceeds from

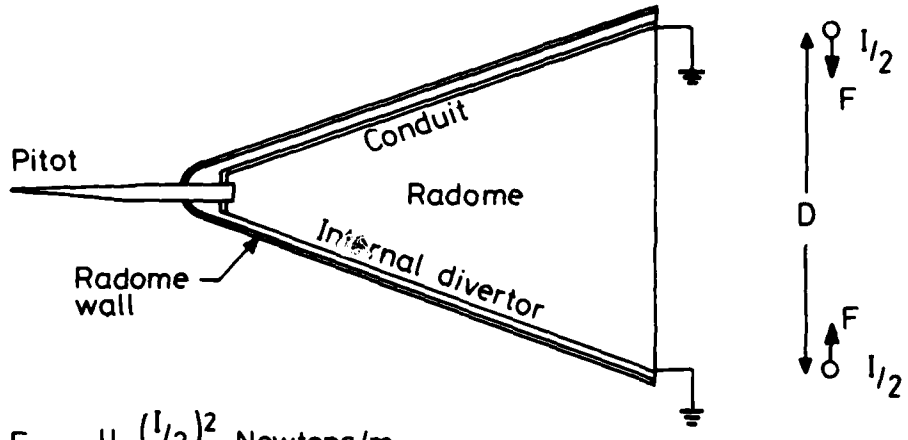

$$F/m = \frac{\mu_o (I/2)^2}{2\pi D} \text{ Newtons/m}$$

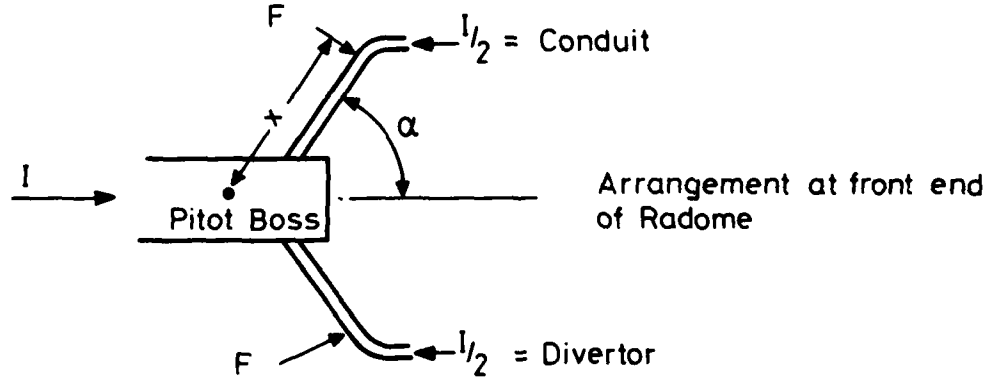

The force per metre (F) at x, normal to the conductor is given by :-

$$F = \frac{\mu_o I^2}{16\pi x} \left\{ \frac{2 - \cos\alpha}{\sin\alpha} \right\} \text{ Newton/m}$$

Figure 4 Magnetic Forces on Conduit and Internal Divertor Strip for Minimum Arc Channel Interaction Conditions

some other attachment point on the aircraft towards the ground, there will clearly be some delay between the time of the initial leader attachment, and the time of the arrival of the first return stroke. During this delay the aircraft will have moved forward and some degree of sweeping of the leader channel will have occurred. The swept leader velocity lies between 5×10^4m/s and 3×10^6m/s, and the return stroke velocity lies between 1×10^7m/s and 1×10^8m/s. With an aircraft altitude of between 1,500 and 3,000m, the time

interval between the initial leader attachment and the arrival of the return stroke will vary from 0.5×10^{-3}s and 60×10^{-3}s. If the aircraft speed is considered to be in the range 66m/s (150 mph) and 200m/s (450 mph) the distance travelled by the aircraft in the time range given can vary between 0.033m and 12m. In addition the original leader path could be virtually anywhere within something like a 270° solid angle. Clearly therefore there is a vast number of combinations of the parameters within the limits given above which can set the conditions where the return stroke arrives at the pitot boom via a channel lying back close to the radome wall, as shown in Fig. 5.

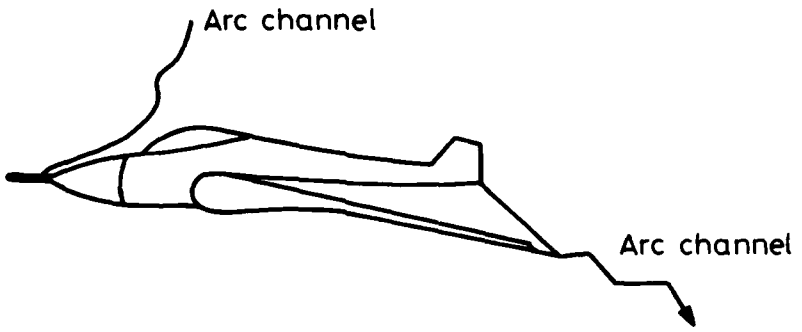

Figure 5 Maximum Arc Channel Interaction Condition

In these circumstances the simple system (Section 3.2) will experience a force due to the interaction of the current in the protection system and the magnetic field of the lightning channel forcing the cable conduit inwards into the radome interior. With the channel very close to the radome wall giving a conduit/channel distance of say 60mm and a peak current of 200kA, the peak inward force would be 133,000 N/m (∿ 13 tons/m) see Fig. 6.

For hybrid systems the forces are in general lower, as the current in the reacting components is reduced by a factor of about 2.

Figure 7 shows the forces acting on a system using an external strip. Assuming equal sharing of the current either side of the new attachment point, viz. the worst case, then the peak inward force on the conduit will be 66,000 N/m (∿ 6.5 tons/m).

Where an internal strip is used the current in the conduit is reacting to the magnetic field of the full lightning current but the distance to the arc channel will be greater than the distance to an external strip. For a distance of 60mm between arc channel and conduit the peak force will be 67,200 N/m (∿ 6.5 tons/m). See Fig. 8.

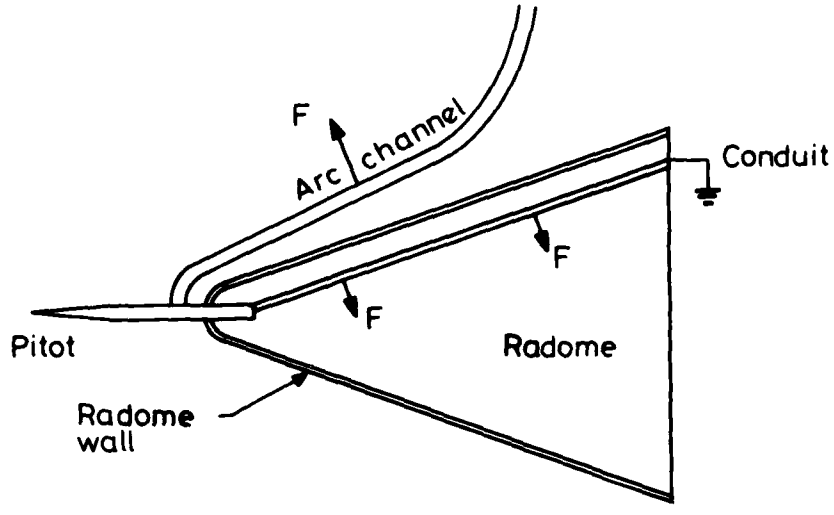

Figure 6 Magnetic Forces Acting on a Simple Conduit Protection System for Maximum Arc Channel Interaction Conditions.

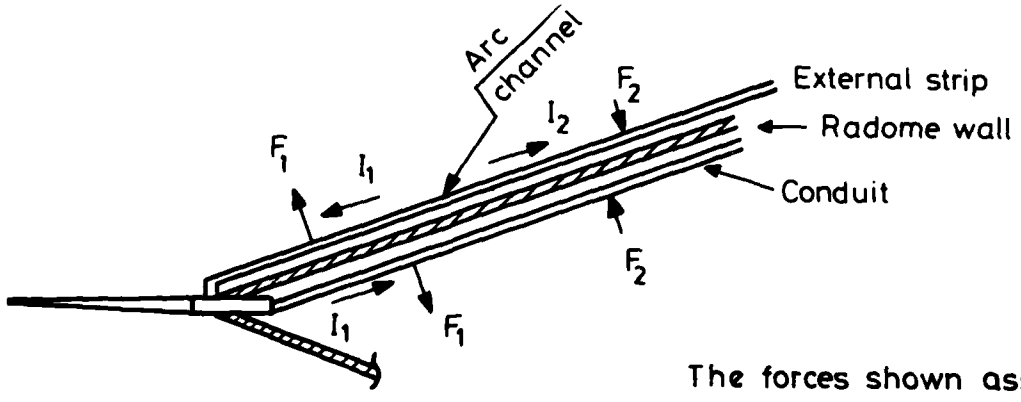

The forces will be similar in magnitude to those shown in Fig. 3, but the direction of the force will differ as shown above.

Figure 7 Magnetic Forces on Conduit and External Strip for Maximum Arc Channel Interaction Condition.

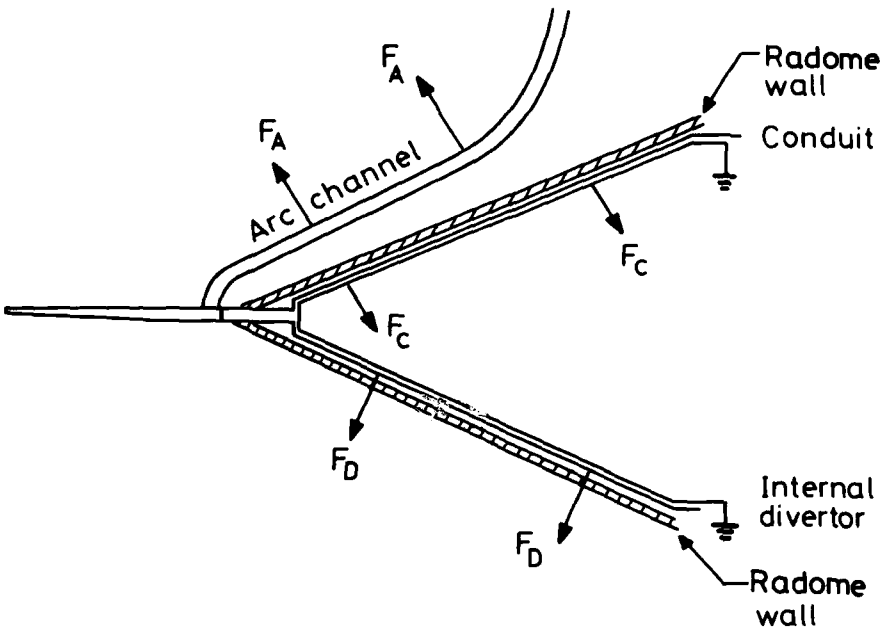

The arrows F_A, F_C, and F_D indicate the direction of the forces on the Arc channel, Conduit and Internal divertor respectively. These forces are in addition to those shown in Fig.4.

Figure 8 Magnetic Forces on Conduit and Internal Divertor for Maximum Arc Channel Interaction Conditions

4.3 Localised Danger Points

Sections 4.1 and 4.2 above deal with gross peak forces acting upon the components of the various protection systems. Additional localised forces of very high magnitude can also be generated at various conductor junctions unless great care is taken in the design stage. The main criterion is to consider the inductively dominated current path either side of the true point of electrical contact, and the forces arising from this current path. In this respect it is important to remember that two rivetted or bolted surfaces that have been anodised or otherwise surface protected can only be considered to be in true electrical contact at the rivet or bolt. The lightning currents are concentrated in small conductors in these systems and these high current densities can cause danger points in places where they are least expected. Many cases could be quoted but the principles are established in the example shown in Fig. 9. This shows a pitot heater cable conduit fastened to a forward bulkhead, and being secured on the rear side by an anodised aluminium bracket.

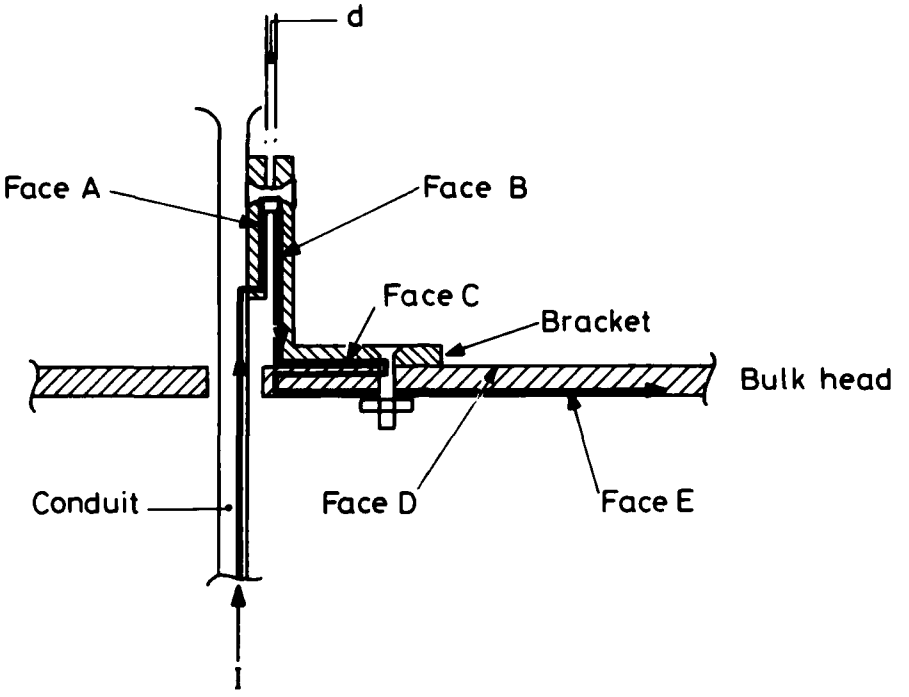

Figure 9 Magnetic Forces at a Typical Local Problem Area.

The current path produces parting forces between faces A and B. The distance (d) between the current paths at faces A and B depends upon the depth of anodising and the currents skin depths. It is however very small compared to the width of the bracket (b). If ℓ is the length of the bracket the parting force will be

$$F = \frac{\mu o \ I^2 \ell}{2b} \quad \text{newtons}$$

If the bracket is assumed to be 25mm wide x 50mm long (1" x 2") and the peak current is 200kA, then the peak parting force will be 50,000 N ($\sim$ 5 ton). An alternative method of mounting a conduit on a bulkhead avoiding these forces is shown in Fig. 10.

5 METHODS OF TESTING

Whilst it is possible to calculate the peak forces that may occur during a lightning strike, the effect of such pulsed forces on a structure will depend upon the duration and waveform of the pulse, and the mechanical response of the structure. During the short duration of these pulsed forces the mass of the structure may prevent it from being appreciably displaced due to its relatively slow mechanical response time. Maximum mechanical stresses occur at maximum deflection when all the kinetic energy is converted into strain energy. For design purposes it is convenient to define an equivalent force F_e which if applied continuously would produce the same stress as the

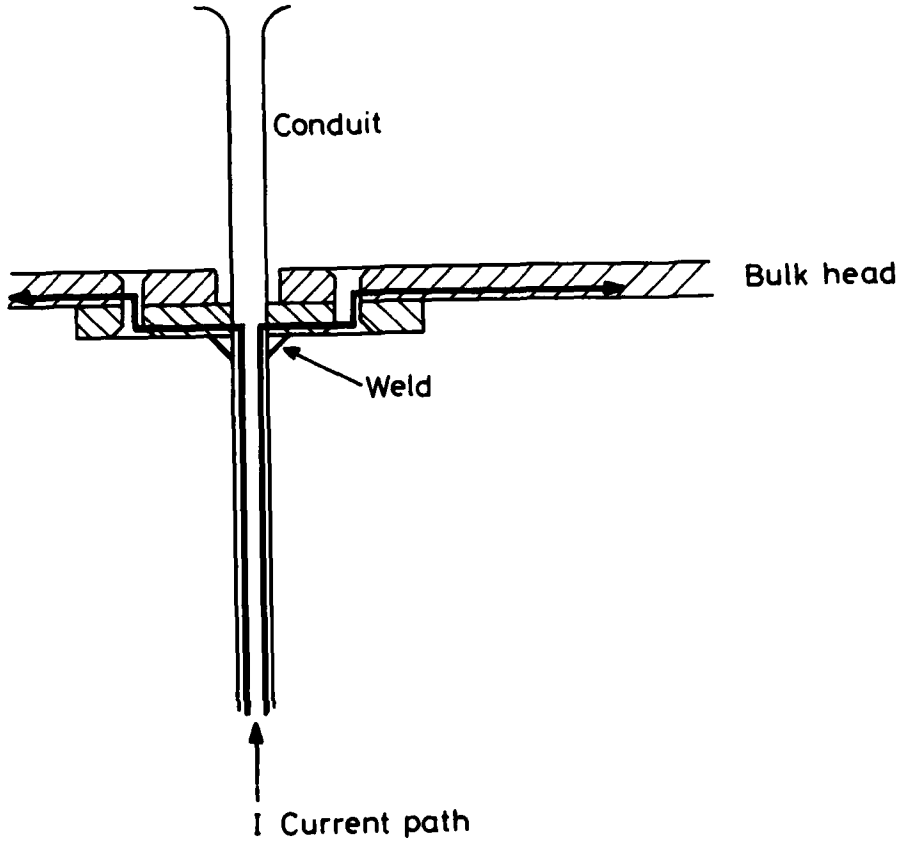

Figure 10 Alternative Arrangement for Detail shown in Fig. 9

pulsed force. In unpublished work in 1959, T.E. James of the Culham Laboratory established a relationship between the effective force (F_e) and the peak force (F_o) in terms of τ the pulse decay time, and ω the mechanical angular frequency of the structure. The effects of τ and ω as applied to forces arising from magnetic interaction during a lightning strike can be summarised as follows:-

1. If τ is very much smaller than $\frac{1}{\omega}$ as for relatively heavy and/or flexible structures, the effective force will be much smaller than the peak force and will be roughly proportional to $\int i^2 dt$.

2. If τ is very much bigger than $\frac{1}{\omega}$ as for light stiff systems the effective force roughly equals twice the peak force. For this doubling of the peak force to occur the current rise time must be very much $<< \frac{1}{\omega}$.

3. If $\tau \simeq \frac{1}{\omega}$ the effective force is approximately 45% of the peak force.

The interactions between pulsed forces and the structure are often difficult to compute, and full scale testing is often the only satifactory way of establishing the total effect of these forces on the protection system. Some comments on general testing technology are therefore appropriate.

5.1 The General Case

The first and apparently simplest approach is to test the system fully mounted on its radome. A radome is however a very expensive piece of equipment, and as it is essentially constructed of dielectric material, its serves no useful purpose in itself in tests intended to investigate induced voltages and magnetic forces. A simple open wooden frame could alternatively be used providing there is suitable replication of the protection system's support devices. Representative sections of the radome wall could be used in places where the radome wall strength is likely to be a significant factor. The rear section of the system under test should terminate in a closed metal box representative of the aircraft fuselage. This box can be used to contain diagnostic probes, and items of electrical significance such as simulated bus-bar impedances. The shape and size of the box is generally unimportant but care must be taken to reproduce the entry points of cable conduits and divertor strips as faithfully as possible, so that localised forces described in Section 4.3 can be effectively studied. The 'open frame' technique has the additional advantage of easy access for inspection and photography, and gives greater freedom in the positioning of the return current conductors. This is an important point if the effects of the magnetic field are to be investigated in a realistic way. Sophisticated systems for measuring pulsed mechanical forces exist, but it will normally suffice to note the total damage, if any, at the end of the test. Photographic records should be kept of any sparking or arcing that occurs during the pulse.

For measurement of the indirect effects that may result from the lightning strike, it is necessary to reproduce the pitot heater failure by 'earthing' the heater cables at the pitot end. Measurements should be made of the voltages appearing at the bus-bar terminals when the cable is terminated with a simulated bus-bar impedance or left open-circuit. The former measurement indicates the voltage transient that will occur at the bus-bars during a lightning strike should the heater insulation fail. The latter measurement will indicate the voltage transient that will stress the heater insulation during a strike.

The voltage transients recorded may have elements of both fast flux coupling and resistive coupling. These elements may be separately assessed by analysis of the waveform recorded, as indicated in Fig. 11.

The voltages induced can be a combination of both fast flux and resistive coupling. The former is the product of the Mutual Transfer Inductance M_{TF} and di/dt, while the latter is a function of IR delayed by the time taken for the current to penetrate the conduit wall. The M_{TF} can be calculated from the actual recorded voltage at time zero and the di/dt at time zero. The rest may be deduced from the actual case shown in Fig. 11.

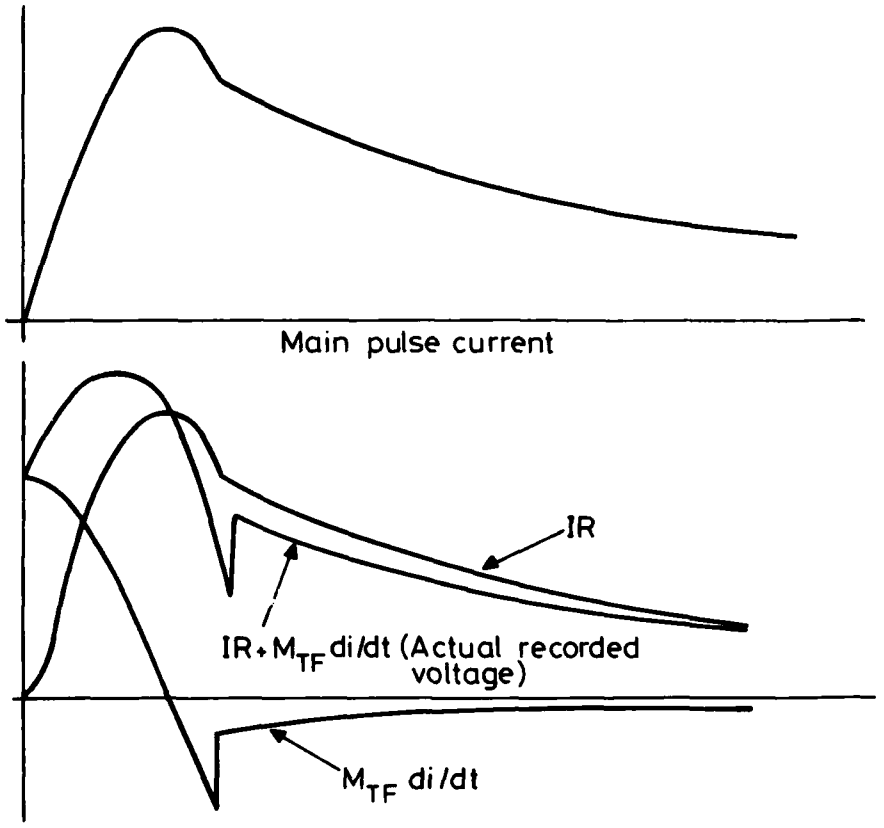

Figure 11 Curves Showing the Derivation of an Induced Voltage Curve

The failure mechanisms under investigation are the inductively and resistively coupled induced voltages, and the mechanical forces arising from magnetic interactions. The first two failure mechanisms scale to di/dt and I peak respectively, whilst the latter failure mechanisms scales to I^2peak and $\int I^2dt$. The pitot will be in zone 1a and the appropriate internationally accepted test current waveforms will be current components A and B. Current component B however contains none of the parameters required for failure, and current component A alone need be used. It should however have an initial di/dt of not less than 20kA/μs. The suggested waveform therefore is a unidirectional pulse having an initial di/dt of ≥ 20kA/μs rising to a maximum of 200kA ± 10% and decaying exponentially to zero with a time constant of ∿ 100μs thus giving an action integral of ∿ 2 x 10^6 A^2s.

5.2 Minimum Arc Channel Interaction Simulation

When simulating the condition of minimum arc channel interaction described in Section 4.1 the return conductors are spaced around the test piece so as to form the outer component of a coaxial system, with a test piece

forming the inner component. Due to the possible complex geometry of the system under test (particularly in the case of some hybrid systems) a simple concentric conductor configuration is not possible. The following procedures may then be adopted. The computed magnetic field around the test piece due solely to current flowing in the test piece itself is plotted in three dimensions. The return conductors are then placed around the test piece at a convenient distance from it, and so positioned that they all lie on the same flux surface throughout their length. The spacing between the conductors should be regulated such that the function $\int H d\ell$ should remain the same between each conductor and its neighbour either side. The number of conductors employed should be as great as practical considerations allow, but in any case it should not be less than six.

5.3 Maximum Arc Channel Interaction Simulation

This simulation is in general simpler than the preceeding case. For this a single conductor can be used to carry the simulated lightning current along the chosen lightning channel path to the pitot and a hard connection made. The forces acting on the arc channel will cause it to move but in the case of a natural lightning strike to an aircraft the aerodynamic forces on the arc channel will tend to stabilise the arc and it is unlikely to move a significant distance during the short risetime. More work is needed however to understand this fully. If the system is to be tested for an attachment to the mid-point of an external divertor strip it may be more convenient to make th connection via a short arc. As only current component A is used the arc root damage will be negligible.

6. CONCLUSIONS

1. Direct puncture of a radome having a forward mounted pitot is extremely unlikely. The main hazards, both direct and indirect, arise from lightning currents flowing in the pitot heater cables.
2. These hazards can be contained by covering the heater cable throughout its length with a conduit that carries all or part of the lightning current.
3. The current carrying capacity of the conduit may be assisted by other parallel lightning path(s), but all paths combined must be capable of carrying the total action integral of the strike safely.
4. The pitot heater circuit should be a two-wire system. Single wire earth return systems are not suitable for this application.
5. The system must be designed to withstand the magnetic forces on it. Care must be taken with detailed design at conductor current junctions.
6. Full scale lightning tests should be conducted on the final design for both direct and indirect effects.

THE ROLE OF FIELD CALCULATIONS IN SIMULATED LIGHTNING TESTING

B.J.C. Burrows
Culham Laboratory, England

This paper contains information derived during the course of contracts with the United Kingdom Ministry of Defence.

INTRODUCTION

Through lightning simulation testing, a wide range of possible effects on an aircraft arising from an in-flight lightning strike may be investigated. These include direct effects (i.e. physical damage from burn through, puncture and vaporisation, and magnetic forces etc.) and indirect effects on antennas, electrical and electronic systems etc. The increasing use of solid state electronics in flight critical systems and the developments in aircraft construction techniques (for example, the use of glass fibre, nomex and graphite composites) makes accurate simulation very important in order to assess reliably the safety and integrity of these systems when exposed to the indirect effects of lightning.

Within the past two or three years considerable improvements in understanding the requirements for satisfactory tests for indirect effects have been made. Some of the problems were discussed in previous papers, (references 1 and 2) and a report, (reference 3) and therefore the aim of this paper is:-

1 to recommend that these improved simulation techniques are adopted in future tests;

2 to demonstrate the value of easy-to-use field programmes to facilitate test rig design and the prediction of induced voltages;

3 to indicate those areas of research where new quantitative information is required to allow further improvements in lightning simulation.

The last can be briefly dismissed. Although the simulation of the low frequency components (below 300kHz) of lightning is the first consideration in the design of test equipment, it has become evident that high frequency effects are important, particularly the presence of standing waves at several megahertz on the aircraft skin. Much more information about the high frequencies present is required from the lightning interaction phenomenologists.

BRIEF REVIEW OF TEST RECOMMENDATIONS FOR

INDUCED VOLTAGES IN SMALL AND LARGE STRUCTURES

Formal recommendations on testing for indirect effects are contained in a small number of documents (references 4,5,6,7 and 8), three of which (5,6 and 7) are derivative from reference 4, the SAEAE4L committee report. Two of the documents (6 and 7) do not include information on engineering tests since engineering tests are outside the scope on these documents. (Note: an engineering test is defined as one which is used to find design information, as distinct from a qualification test which is for proving purposes. Indirect effects tests at the moment are mainly engineering tests.)

The two remaining documents (references 4 and 8) are the so-called "blue book" (SAEAE4L document) and the 'green book' (the Culham Laboratory Report R163). These have only brief descriptions of test rig design and lay-out for indirect effects on either external electrical hardware or whole aircraft tests. There are several other types of indirect effects tests which are required and not yet described in the formal documents. Also the improved understanding of lightning fields and of the design of test facilities has rendered obsolescent much of the existing material on whole aircraft testing. Difficulties in testing were not ignored in these early documents: references 5 and 8 in particular point out many problem areas. For example, the scaling of results obtained with low-level pulses can be a formidable problem, exacerbated by non-linearity in the test object. Other problems appear from overall facility effects on the current distribution, the signal to noise ratio, and the generation of spurious high-frequency current components. Moreover, recommendations are never sufficiently detailed to enable satisfactory rigs to be designed that would yield the same results in different Laboratories.

Two particular types of test are not mentioned but deserve comment. Since large aircraft are usually too big to test economically, small rigs can be used to test sub-structures or components, for example, graphite or glass fibre composite panels behind which wiring is situated. Field calculations enable the current density due to a severe stroke to be calculated for in-flight conditions; this is usually translatable to the test rig by suitable choice of geometry and test current level, but the process has not been discussed. The other type of test not yet described is the swept CW technique currently being developed in several quarters, in particular at the Boeing Aircraft Company. Discussions on the usefulness of this test are necessary to determine its advantages or disadvantages over impulse testing, and the formal documentation should comment on its range of applicability. Detailed considerations for radome tests have been given in a previous paper at this conference (reference 9) and illustrate the care needed for valid electrical and mechanical measurements.

DETAILED COMMENTS AND SUGGESTIONS FOR

IMPROVED TEST RECOMMENDATIONS

The following points not covered in existing documents need consideration and detailed specification.

1 The maximum current and di/dt attainable from a given size capacitor bank are desirable to give best signal-to-noise ratio. This implies the need for low-inductance test circuits. Lumped inductors for trimming the pulse waveform are especially to be avoided since they give self-resonance problems and the added inductance means that higher voltages are required from the capacitor bank to give a high current and high di/dt. The higher voltage required on the capacitor bank results in more radiated interference from that capacitor bank when it is switched.

2 A low-inductance test circuit requires a low-inductance capacitor bank using wide metal strips for connections, a low inductance switches and if a Marx generator is used, as few stages as possible. A total system inductance - airframe + capacitor bank - of approximately 3-4 micro-henries should be aimed at.

3 If hard-wire diagnostics are to be used from the aircraft (or large sub-assembly or test rig etc.) careful attention must be paid to system earthing to avoid serious diagnostic problems. For aircraft tests earthing (or grounding) a part of the airframe directly is desirable, in which case the capacitor bank should have the minimum stray capacitance to ground, be compact, close to the drive point of the airframe and have decoupled charge and trigger leads to the switch. See figure 1.

4 If ground power is required during an aircraft test it is greatly facilitated by point 3 above; that is, by having a grounding point on the airframe. This should be a tube directly to the floor or grounding point through which the power cables and the diagnostic cables can be safely routed. No other part of the system can be earthed.

5 All of the points mentioned in (1) to (4) influence the production of spurious resonances in the 5-15 megahertz range in the aircraft test facility. The ideal is that the aircraft or sub-assembly should only have resonances typical of the in-flight strike situation and these will be associated with the aircraft dimensions, that is, length and wing-span. The resonances must not be dominated by the stray capacity of the capacitor banks, switch and cables to ground. That is, the airframe/return conductor system should control system resonances rather than the stray or lumped electrical elements of the generator. This condition is satisfied by the requirement mentioned in point 3 above, that a simple compact bank is used well spaced from the ground,

but close to the aircraft. It should be noted that the hf resonance problem is in general severe when multi-stage Marx generators are used, owing to the variability of the hf spectrum generated by the erection time jitter. A single stage bank is the ideal but recent work in Culham has shown that a three stage Marx generator bank can give acceptable results.

6 To improve simulations at high frequencies the question of standing waves on the airframe should be considered. Consideration of the in-flight strike suggests that the extremities are voltage antinodes and current nodes and the centre of the fuselage and wing roots will be voltage nodes and current antinodes (see figure 2). Hence the airframe or wing under test is preferably excited at the wing tip, nose, or tail and the return conductors joined at the wing root or fuselage centre, so giving a current antinode at this connection point at the fundamental resonance frequency. The Q of this resonance may be easily controlled by damping as described in reference 1.

7 The existing documentation does not address the problem of scaling satisfactorily. It is most unlikely that results measured at 250 amps on an aircraft can be scaled reliably to 200 kA particularly if any importance is placed on the initial transient. Consider a test on a wire for a data bus in a digital system. To test for possible interference the test should be able to measure approximately 0.5V or less when 200 kA flows in the aircraft. A scaled down test to 250 amps would therefore need to have an adequate signal to noise ratio to measure a voltage of

$$\frac{0.5 \times 250}{200,000} \text{ V} \simeq 600\mu\text{V}$$

Owing to transient interference radiation from the capacitor bank it is well-nigh impossible to measure such signal levels satisfactorily. Although the use of fibre-optic links appears promising, receiver noise limits the available dynamic range to signals greater than approximately 10mV unless considerable amplification is used before the optic cable drive transmitter.

8 A further scaling problem concerns measurements on graphite fibre structures especially those containing aluminium honeycomb. Some recent work at Culham in which low current dc measurements and high current pulse measurements were compared revealed substantial non-linearity in the performance of graphite/aluminium honeycomb, so requiring high current pulse tests for representative results.

9 Further guide lines are needed on testing graphite composites/aluminium structures owing to the current redistribution that takes place between the metal and composite during the high current pulse. For reliable results the pulses must contain a correctly-proportioned pulse in respect of both di/dt and peak current. This arises because the

high resistance of graphite makes it necessary to have a high di/dt to drive the surface current through the graphite. This surface current then produces the IR voltage in the composite panel measured internally. If a pulse of similar peak amplitude were used but much lower di/dt results would indicate that the di/dt effects the scaling of IR voltages whereas an IR voltage would be expected to scale with peak current! Thus a 100kA/μs pulse or an appropriate scaled fraction is desirable for a full-size component test.

10 Protection techniques can be tested on equipment of small physical size which duplicate the in-flight conditions of a complete aircraft carrying the current pulse of a severe stroke. For example the protection of graphite or glass fibre panels can be assessed by mounting the full-size panel in a small test rig in such a way that its surface current density can be calculated. The amplitude of the current test pulse is chosen so as to produce the current density levels that would appear in the same panel when used on the aircraft. The surface current density on the aircraft itself is obtained also by calculation. This technique makes a substantial reduction in the cost of the testing protection techniques but requires the use of computer programmes which can solve the current distribution. Appendix I describes a new programme called INDCAL for this application. This programme, like the POTENT code (reference 10) used previously for induced voltage predictions, is a 2D calculation which assumes a structure of constant cross section. This is a sufficiently good approximation for most parts of the airframe except where complex geometry occurs at wing root, pylons etc. Empirically determined correction factors are available for predicting induced voltages in complex geometry in slots of a wide range of length-to-width ratios.

11 The present documentation does not define an acceptable current distribution achieved in a test compared to the free space in-flight distribution, and thus the degree by which any test over-or under-emphasises certain voltages is unknown. The computer programmes named above can simplify and quantify these unknowns.

CONCLUSIONS

Indirect effects tests, particularly for whole aircraft or large sub-assemblies, need to be specified more adequately in order that the tests are not dominated by facility effects. Many of the facility effects are described above and solutions are offered for most of them. More information on the attachment process and hf excitations caused by natural lightning to the aircraft is needed and it is believed that the configuration improvements suggested here will need little modification to achieve a better simulation when more information is available. Simple-to-use computer programmes considerably simplify the design of test facilities by providing quantitative data on surface current densities in proposed test rig configurations for comparison with conditions in-flight. They also provide data on total system inductance.

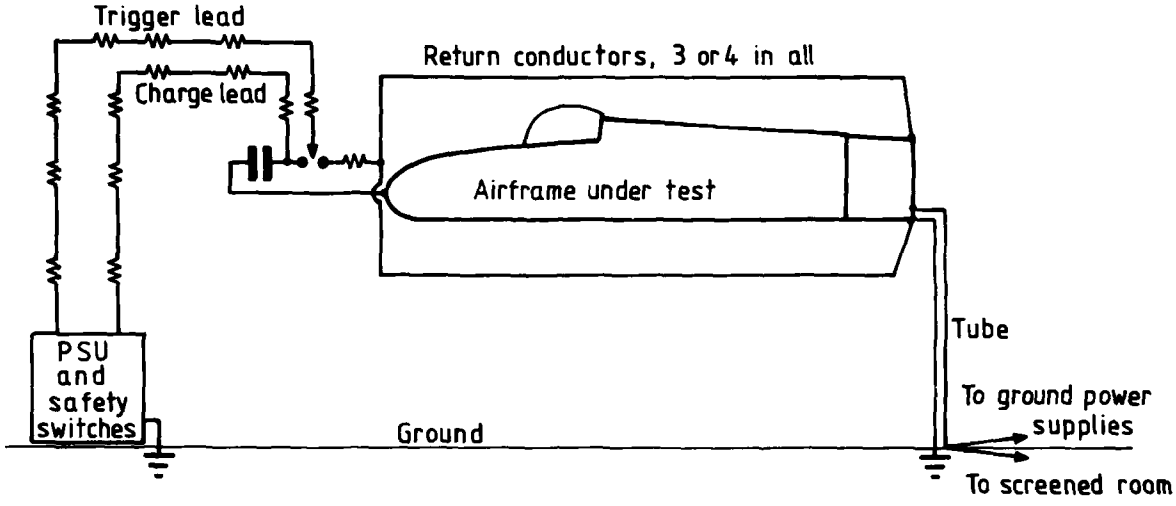

Fig. 1 Typical layout for fuselage or wing test

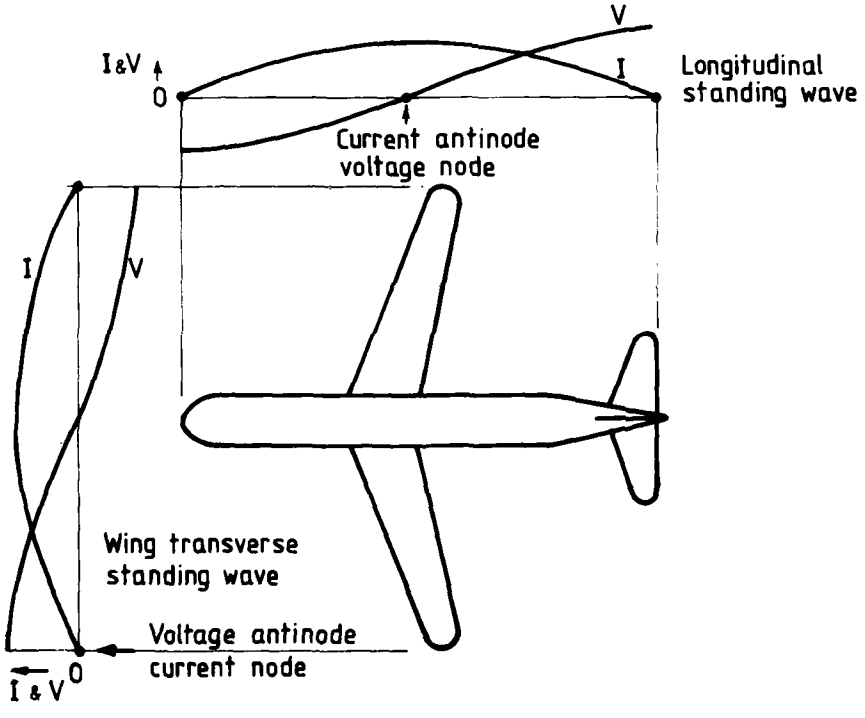

Fig. 2 HF standing wave in air frame

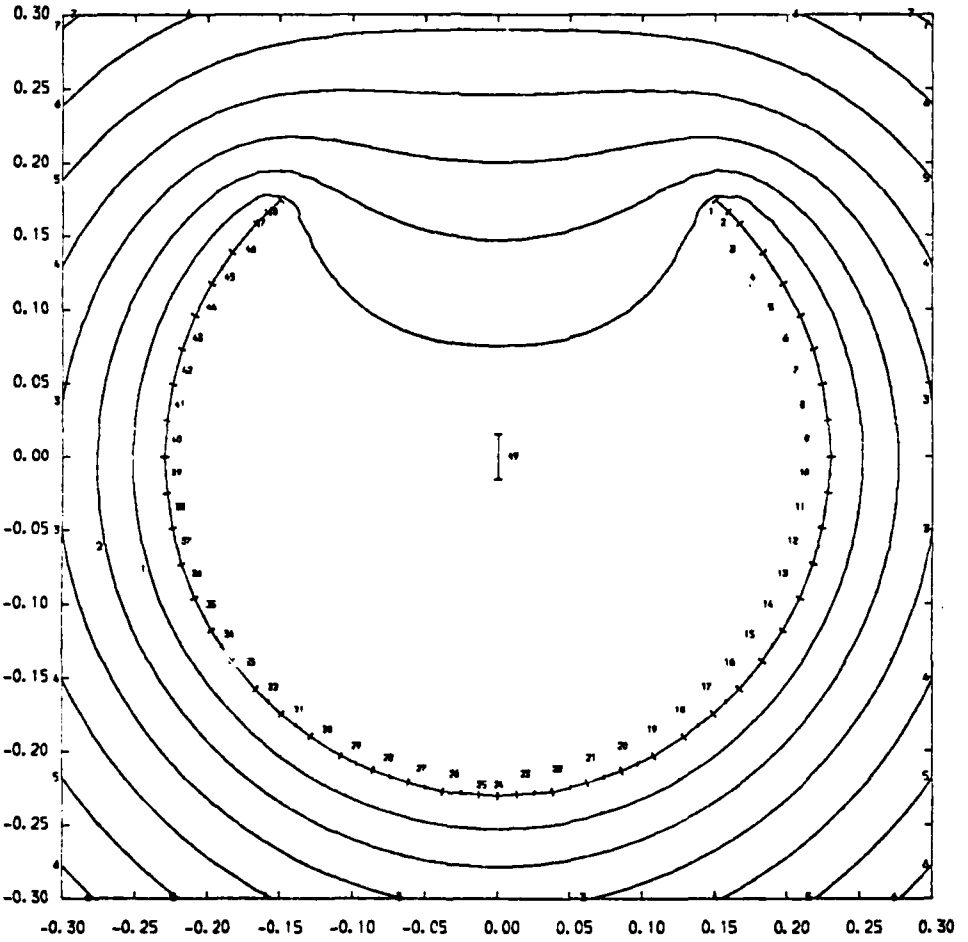

Fig 3. Example of output from INDCAL.
Numbered segments are the structure, the lines are field lines and are also lines of constant M_{TF}.

Appendix 1

Field calculations for aircraft work may be performed in a variety of ways, all of which rely on the same basic physical principle that metal surfaces are the field boundaries and no magnetic flux cuts them. Such calculations can be performed using analogs (TELE-DELTOS resistive paper, electrolytic tank etc.) and by finite element, or finite difference, computer codes. The latter codes are far more reliable than the analog methods and have supplanted them almost entirely. POTENT, a finite difference code has been described previously and was used in work reported in references 1 and 3. INDCAL is a finite element code based on matrix inversion techniques allowing the calculation of current distribution; the field patterns; and common mode coupling factor M_{TF} values for non symmetric shape defined by 50 elements, or a symmetrical shape defined by 2 x 50 elements using symmetry. INDCAL has already been used for several important calculations, and gives results as accurate as POTENT and directly comparable. A brief summary of the principles and features of INDCAL follows.

INDCAL calculates the inductively controlled current distribution around a wing or fuselage using a filamentary approach (ignoring skin resistance) from which the M_{TF} values are calculated.

The M_{TF} at a point p is given by $MTF_p = L - M_p$, where L is the self inductance w.r.t. conductor and, M_p is the Mutual Inductance at the point p.

For the solving of this problem we consider a body to be represented by a series of long straight parallel filaments of circular cross-section. The method relies on the principle that a series of filaments with the correct current distribution has the same overall field at a reasonable distance from any individual filament, as a body of similar cross-section but made from electrically homogeneous sheets.

These filaments are entered into the programme by specifying the end points of a short line, which is called a finiment. The points are then bisected to give the centre of the required filament. The filament radius is then set by dividing the finiment width by a known factor. Thus n finiments are specified by n + 1 points.

INDCAL is an interactive programme; this means that it is controlled by typing commands into the terminal whilst the programme is running. Commands exist which allow the user to perform various operations on the finiments; read and write storage files; read finiment positions form a data file; draw graphs with or without contours; give helpful information, and terminate the programme. These commands may be used as the user requires them.

An example of the graphical output for an INDCAL calculation on a slotted cylinder is shown in Figure 3.

REFERENCES

1 Burrows B.J.C., Luther C., Pownall P.: Induced Voltages in Full Size Aircraft at 10^{11} A/s. IEE Conference on EMC Seattle 1977.

2 Burrows B.J.C.: Tests on Actual Aircraft for Electromagnetic Effects. (Engineering Tests.) ONERA Conference, Paris September 1978.

3 Wallace B.J., Burrows B.J.C., Zietler R.T., Ledwig A.J., Wiles K.G.: Composite Forward Fuselage Systems Integration Volume II. AFFDL-TR-78-110 September 1978.

4 (Plumer J.A., Robb J.D. co-chairman) Lightning Test Waveforms and Techniques for Aerospace Vehicles and Hardware. Report on SAE committee AE4L 1978.

5 Draft MIL Standard Lightning Qualification Test Techniques for Aircraft and Hardware. SAE committee AE4L June 1978.

6 Draft STANAG 3659E. Lightning Qualification Test Techniques for Aircraft and Hardware August 1978.

7 AFSC (USAF) Design Handbook: Electromagnetic Compatability, DH 1-4. Section 7, Lightning and Static Electricity.

8 Phillpott J.: Recommended Practice for Lightning Simulation and Testing Techniques for Aircraft. CLM-R163 Culham Laboratory.

9 Hanson A.W.: Lightning Protection Techniques for Radomes having Forward Mounted Pitots. Symposium on Lightning Technology. Nasa Langley, Hampton 1980.

10 Thomas C.L.I. POTENT: A Package for the Numerical Solution of Potential Problems in General 2 Dimensional Regions. Culham Laboratory Report CLM P339, (or in a more available form: Software for Numerical Mathematics Edited by Evans D.J.: Academic Press 1974. Chapter has same title as CLM P339).

1. Report No.	2. Government Accession No.	3. Recipient's Catalog No.
Supplement to NASA CP-2128 FAA-RD-80-30		
		5. Report Date: January 1981
4. Title and Subtitle: LIGHTNING TECHNOLOGY		6. Performing Organization Code: 505-44-13-02
7. Author(s)		8. Performing Organization Report No.: L-13666
		10. Work Unit No.
9. Performing Organization Name and Address: NASA Langley Research Center, Hampton, VA 23665		11. Contract or Grant No.
		13. Type of Report and Period Covered: Conference Publication Supplement
12. Sponsoring Agency Name and Address: National Aeronautics and Space Administration, Washington, DC 20546 and Florida Institute of Technology, Melbourne, FL 32901 and Department of Transportation, Washington, DC 20590		14. Sponsoring Agency Code

15. Supplementary Notes

16. Abstract

This report is a compilation of papers presented at the 1980 Symposium on Lightning Technology which were not available for printing at the time of publication of NASA CP-2128. The Symposium was held at the NASA Langley Research Center April 22-24, 1980, and included papers concerning lightning phenomenology, measurement, detection, protection, interaction, and testing.

17. Key Words (Suggested by Author(s))	18. Distribution Statement
Lightning and aircraft interactions Lightning instrumentation Lightning phenomenology Lightning protection Lightning detection Lightning simulation	Unclassified - Unlimited Subject Category 47

19. Security Classif. (of this report)	20. Security Classif. (of this page)	21. No. of Pages	22. Price
Unclassified	Unclassified	133	A07

For sale by the National Technical Information Service, Springfield, Virginia 22161

NASA-Langley, 1981